Università degli Studi di Torino

Doctoral School of the University of Torino

PhD program in Chemical and Materials Science XXXVIII Cycle

Ru-based Catalysts from deposition-precipitation: Structural and Surface Properties from Pristine to Fully Reduced States

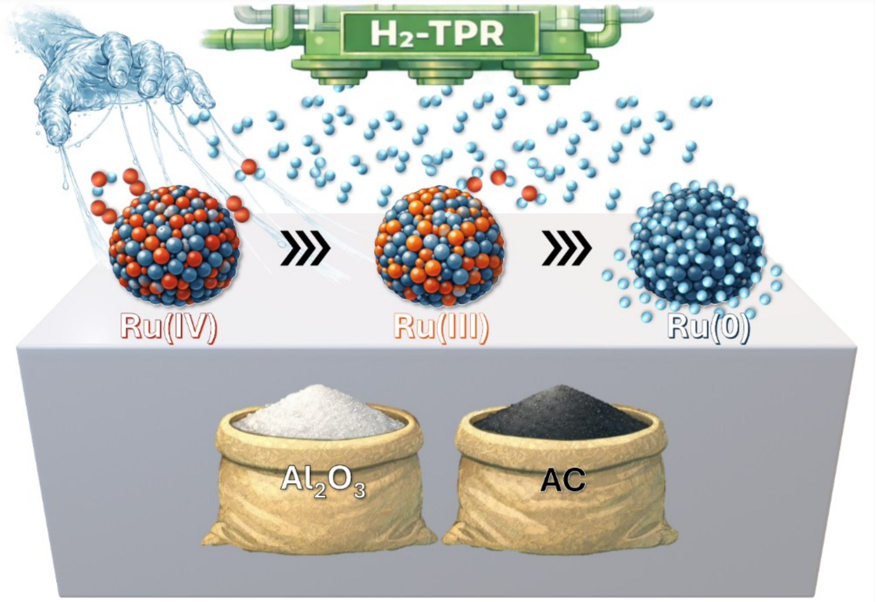

Paolo Lazzarini

Supervisor:

Prof. Elena Groppo

Dr. Andrea Piovano

Università degli studi di Torino

Doctoral School of the University of Torino

PhD program in Chemical and Materials Science XXXVIII Cycle

Candidate: **Paolo Lazzarini**

Supervisor: **Prof. Elena Groppo**
Dr. Andrea Piovano

Jury members: **Dr. Giovanni Di Liberto**
Dip. di Scienza dei Materiali
Università degli Studi di Milano Bicocca

Prof. Francesco Mauriello
Dip. di Ingegneria Civile, dell'Energia, dell'Ambiente e dei Materiali
Università degli Studi Mediterranea di Reggio Calabria

Dr. Sara Morandi
Dip. di Chimica
Università degli Studi di Torino

Head of Doctoral School: Prof. Enzo Medico

PhD Program Coordinator: Prof. Bartolomeo Civalleri

Table of Contents

Abstract

Ruthenium-based heterogeneous catalysts play a central role in industrial hydrogenation processes, yet a unified mechanistic understanding of how oxidized Ru precursors transform into catalytically active species remains incomplete. In particular, the reducibility of hydrated Ru oxide phases prepared by deposition–precipitation (DP), the identity of intermediate states formed during activation, and the influence of water, support chemistry, and synthesis history on these processes are still debated. This PhD thesis addresses these knowledge gaps through a systematic, multi-technique investigation of the oxide-to-metal transformation in unsupported and supported Ru catalysts under industrially relevant conditions.

The work was conducted within the framework of the European Next Generation EU program and represents a joint academic–industrial collaboration between the Department of Chemistry of the University of Torino and Chimet S.p.A. Combining laboratory-scale methods routinely employed in industry with advanced synchrotron- and neutron-based techniques, this thesis follows the structural and chemical evolution of Ru catalysts from their oxidized, hydrated state to the reduced phase under hydrogen.

Comprehensive characterization of the oxidized precursors reveals that DP-derived Ru does not form a single, well-defined RuO_2 phase. Instead, it consists of highly dispersed and strongly hydrated Ru(IV) oxy-hydroxide domains spanning a continuum from disordered RuO_2-like motifs to partially crystalline regions, depending on support chemistry and hydration state. Activated carbons stabilize highly defective, strongly hydrated species, whereas alumina promotes partial structural ordering. Surface-sensitive O K-edge NEXAFS identifies peroxo-like Ru–O–O species across all systems, whose abundance correlates directly with the systematic hydrogen overconsumption observed during H_2 temperature-programmed reduction (H_2-TPR), establishing a direct link between surface oxygen chemistry and macroscopic reducibility fingerprints.

In situ bulk-sensitive techniques (Ru K-edge XAS, high-energy X-ray total scattering with PDF analysis, and XRD) coupled with multivariate statistical analysis demonstrate that reduction proceeds through a transient Ru(III) intermediate with structural fingerprints consistent with a corundum-like Ru_2O_3 phase. This finding resolves the long-standing ambiguity associated with the multi-feature H_2-TPR profiles characteristic of DP-derived Ru

catalysts. Concurrent surface-sensitive investigations by *in situ* FTIR, O K-edge NEXAFS, and inelastic neutron scattering (INS) reveal that reduction is accompanied by tightly coupled surface restructuring processes, including hydroxyl condensation, peroxo rearrangement, formation of defective RuO_2–x phases, and transient stabilization of Ru–H species. While IR selectively detects terminal hydrides, INS provides direct spectroscopic evidence of multi-coordinated and subsurface hydrides and captures hydrogen spillover at the Ru–Al_2O_3 interface, offering rare experimental confirmation of this frequently invoked phenomenon.

Catalytic validation in the selective hydrogenation of benzaldehyde demonstrates that catalytic performance cannot be interpreted solely in terms of metallic Ru formation. Unsupported catalysts containing amorphous and partially hydrated $RuO_x(OH)_Y$ phases exhibit significant activity under mild conditions, indicating that oxidic or partially reduced Ru states can directly participate in hydrogen activation. In contrast, alumina-supported systems require higher temperatures to reach comparable activity, consistent with progressive metallic Ru formation stabilized by the support. These results challenge the widespread assumption that fully reduced Ru represents the exclusive active phase in Ru-catalyzed hydrogenation.

A unifying outcome of this thesis is the recognition of water as a structural and kinetic variable governing reducibility, dispersion, and site accessibility. Controlled drying and ageing experiments demonstrate that gradual dehydration drives structural reorganization and condensation processes that critically affect catalyst stability and performance. The drying step thus emerges as a deliberate thermal treatment rather than a simple solvent-removal operation, particularly in industrial liquid-phase processes.

By integrating complementary bulk- and surface-sensitive techniques with catalytic validation, this work establishes a coherent mechanistic framework for the activation of DP-derived Ru catalysts and provides practical guidelines for controlling hydration, reducibility, and performance in industrially relevant systems.

Chapter 1

1 Introduction

1.1 Ru-based catalysts

1.1.1 Established applications and emerging opportunities for Ru-based catalysts

Catalysts based on ruthenium (Ru) already play a pivotal role in the chemical industry both in the form of supported and unsupported nanoparticles. Supported metallic Ru nanoparticles are largely employed for hydrogenation and hydrogenolysis reactions. They are integral to the Haber-Bosch process, to synthesize ammonia from nitrogen and hydrogen, playing a crucial role in the production of fertilizers and other chemicals.[1–3] In hydrogenation and hydrogenolysis catalysis, Ru catalysts have attracted renewed attention due to their ability to promote reactions under milder conditions or with alternative selectivity patterns compared to conventional Pd- or Pt-based systems. In particular, Ru-based catalysts have demonstrated promising performance in the selective hydrogenation of functionalized molecules and in the cleavage of oxygenated groups derived from biomass feedstocks, which is part of the broader effort to develop renewable energy sources and reduce dependence on fossil fuels.[4–6] Researchers have also recently begun to explore Ru catalysts for upcycling of polyolefin waste into valuable hydrocarbons, aiming to address plastic pollution and promote sustainable recycling practices,[7–9] or for the energy sector, for example in the decomposition of ammonia into nitrogen and hydrogen, providing a clean hydrogen source for fuel cells and other applications.[2,10,11]

From a broader perspective, Ru occupies a peculiar position among platinum-group metals, combining a relatively low cost with rich and complex surface chemistry. Compared to more extensively exploited noble metals such as Pt and Pd, Ru exhibits stronger metal–adsorbate interactions and a marked tendency to access multiple oxidation states under reaction conditions. These features make Ru-based catalysts particularly attractive for reactions involving the activation of strong chemical bonds, such as C-C, C-O, C-N and N-N bonds, which are central to many emerging catalytic processes. At the same time, this intrinsic reactivity introduces additional complexity in catalyst design, as subtle variations in structure, particle size or chemical environment can lead to significant changes in catalytic performance.

The versatility of ruthenium is further exemplified by its oxide form, RuO_2, whose ability to reversibly switch between different oxidation states under operating conditions is a key factor underlying its outstanding electrochemical performance,[12] as well as its applications in the fields of supercapacitors and chemical sensors.[13–15] Its dynamic behavior is particularly relevant in reactions such as the oxygen evolution reaction (OER),[16,17] where surface restructuring and redox processes are intimately linked to catalytic activity.[12] In this field Ru is often proposed as an alternative to Ir, offering competing performances at significantly lower costs for the catalyst manufacturing and use. At the same time, the same redox flexibility that enables high activity also raises challenges related to catalyst stability, dissolution and long-term durability, which remain central topics in current research.[13–17]

In the past decades, alongside the consolidation of Pt- and Pd-based catalysts as industrial standards, interest in Ru-based systems has only marginally increased, partly due to the inherent challenges associated with the study of Ru. As discussed in the next paragraphs, Ru exhibits remarkable versatility, with physico-chemical properties that make it a promising candidate for a wide range of catalytic applications. At the same time, its high intrinsic reactivity and sensitivity to external conditions require careful control of structural and environmental parameters, as small variations can strongly influence catalytic behavior. While these aspects have historically limited the widespread adoption of Ru catalysts, they also offer unique opportunities: when properly understood and controlled, Ru reactivity can be effectively harnessed to achieve enhanced performance, tunable selectivity and access to reaction pathways that are less accessible with other noble metals.

In this context, recent technological advances in synthesis, *in situ* and *operando* characterization techniques, and theoretical modeling are playing a crucial role in enabling a deeper understanding of Ru-based systems. Together with the growing industrial demand for cost-effective, high-performance catalysts capable of addressing emerging challenges in energy, sustainability and resource efficiency, these developments are driving a renewed interest in Ru. Rather than being viewed solely as an alternative to more established noble metals, Ru is increasingly recognized as a uniquely versatile element whose sensitivity and reactivity can be transformed from limiting factors into key assets for the design of advanced catalytic and technological systems.

1.1.2 Great potential for tunability comes with great characterization challenges

The broad applicability and tunability of Ru-based catalysts outlined in the previous section are intrinsically connected to a high degree of complexity in their structural, chemical and electronic properties.[12,18,19] Therefore, the same features that make Ru highly attractive from a catalytic perspective also render its characterization particularly challenging. Despite not being more abundant than other rare transition metals, the price of Ru is surprisingly low, and this can be explained simply in terms of lower demand for Ru based systems with respect to other platinum-group-metals (PGM). This combination of relatively low cost and high catalytic potential has contributed to renewed academic and industrial interest in ruthenium, while simultaneously highlighting the need for reliable and detailed characterization strategies to fully exploit its tunability.

From the catalytic point of view, Ru exhibits unmatched activity for hydrogenation reactions, but it lacks selectivity and often requires high activation temperatures to be operational. Because of its high reactivity, completely reduced Ru is instantly oxidized when exposed to air, while the high hydrophilicity of RuO_2 renders almost impossible to have optimal storage and demands dedicated activation procedures. As discussed before, another inherent quality of Ru is its sensitivity to external conditions that, if not properly understood and controlled, can cause serious issues to reproducibility of results. These features place Ru-based catalysts at the boundary between high catalytic performance and experimental complexity, where small variations in pretreatment, atmosphere, temperature or support composition can lead to markedly different structural and chemical states.

Moreover, Ru is often reported to have unexpected or counterintuitive behavior with respect to common heuristic expectations, which often can be misleading and hard to interpret. For instance, Ru activity does not scale with adsorption strength or with size.[20–22] Ru redox properties are easily influenced by its surroundings and can rarely be predicted in analogy with what observed for other PGM.[12] Completely reduced supported Ru nanoparticles are partially oxidized when exposed to CO, a well-known reducing agent, through a process named oxidative disruption, i.e. they are partially re-oxidized and fragmented, with a mechanism not yet fully understood involving the participation of the support and driven by the strong interactions between CO molecules and undercoordinated Ru atoms in the nanoparticles.[23–28] This phenomenon, as it will be further discussed in Section1.2.3, causes issues when using CO as a molecular probe, both for quantitative measurements like CO chemisorption to determine dispersion, and for qualitative measurements like IR spectroscopy of CO interacting with Ru NP. The example of oxidative disruption illustrates how characterization methods routinely applied to other noble metal catalysts may provide misleading or incomplete information when transferred to Ru-based systems, emphasizing the need for combined and, whenever possible, *in situ* or *operando* approaches.

On one hand, when fully understood, the inherent complexity of Ru-based systems grants a high level of tunability of Ru properties, making it a versatile material suitable for many applications. On the other hand, the same complexity poses a serious challenge for any effort towards thorough characterization of Ru based systems. In this sense, characterization challenges should not be regarded merely as limitations, but rather as an integral aspect of the opportunity offered by Ru. The strong sensitivity of Ru to its local environment provides a rich parameter space for tailoring catalytic behavior, while simultaneously motivating the development and application of advanced characterization strategies, which form a central theme of the present work.

1.2 From Ru-oxide to Ru-metal

1.2.1 RuO_2: crystalline reference and hydrated phases

Ruthenium dioxide (RuO_2) is a conducting transition metal oxide that crystallizes in the rutile structure, which represents its thermodynamically stable bulk phase. Owing to its metallic-like electrical conductivity and rich redox chemistry, crystalline RuO_2 has long been employed as a heterogeneous catalyst and electrocatalyst in a variety of oxidation reactions, including CO, NH_3 and methanol oxidation, as well as in the Deacon process for chlorine production from HCl. In the electrochemical field, RuO_2 is a benchmark anode material for the chlor-alkali process and exhibits excellent activity for both the hydrogen and oxygen evolution reactions.

In the rutile bulk structure of RuO_2, each Ru atom is octahedrally coordinated by six oxygen atoms, forming slightly distorted [RuO_6] units (Figure1.1a). Two Ru-O bonds are shorter, with distances of approximately 1.94 Å, while the remaining four Ru-O bonds are slightly elongated, around 1.98 Å, reflecting the anisotropic coordination environment characteristic of the rutile lattice. From a metal-metal perspective, the structure is defined by two distinct Ru-Ru distances. The shorter Ru-Ru distance, approximately 3.1 Å, corresponds to neighboring [RuO_6] octahedra linked in chains running along the crystallographic *c* axis. A second Ru-Ru contribution at about 3.5 Å reflects the three-dimensional connectivity of the rutile lattice, in which each octahedral chain is linked to four adjacent chains. This hierarchical connectivity, combining one-dimensional chains and three-dimensional coupling, underpins both the structural robustness and the high electronic conductivity of crystalline RuO_2.

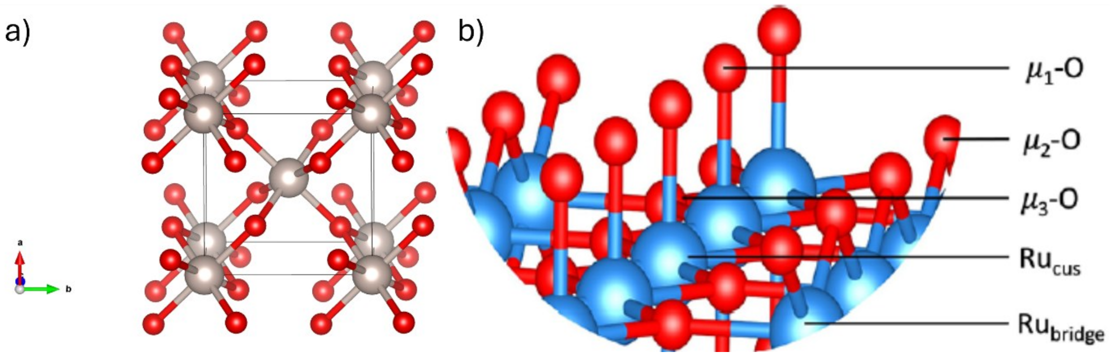

Figure1.1 (a) Structure of bulk RuO_2 rutile. (b) Structure of the most stable RuO_2 (110) surface. Adapted from reference 54.

From a structural perspective, most experimental and computational studies on crystalline RuO_2 focus on the most stable (110) surface of the rutile phase (Figure1.1 b). This surface is characterized by the presence of coordinatively unsaturated five-fold coordinated Ru atoms (Ru_{5c}), bridged oxygen atoms (O_{br}) and terminal oxygen atoms (O_{term}), which together define the surface reactivity. Density functional theory investigations and experiments have shown that the Ru_{5c} sites act as strong Lewis's acid centers and play a central role in adsorption and activation of small molecules. [12,19,29–35]

Atomistic studies of water adsorption on RuO_2(110) have revealed a complex and coverage-dependent behavior.[36–41] At very low water coverages, isolated H_2O molecules adsorb molecularly on Ru_{5c} sites, being in equilibrium with partially dissociated configurations in which water deprotonates to form Ru_{5c}–OH species hydrogen-bonded to neighboring O_{br} atoms. With increasing water coverage, water dimers form on adjacent Ru_{5c} sites, giving rise to mixed molecular–dissociated motifs such as $H_3O_2^-$ species. At even higher coverages, extended hydrogen-bonded networks and quasi-one-dimensional water chains develop along the surface, profoundly modifying both the local structure and the electronic properties of the surface. These findings provide a fundamental framework for understanding how water interacts with RuO_2 surfaces under realistic conditions.

Nanosized RuO_2 can incorporate strongly bound H_2O in its lattice, deeply altering its crystalline structure and stabilizing an amorphous hydrated phase.[12,15,42–44] The hydrous RuO_2 is often reported as $RuO_x(OH)_y$ or as $RuO_2 \bullet nH_2O$ if the stoichiometry is quantified. The water content n is expected to be between 1 and 3 in commercially available RuO_2 and has been measured to be up to n = 2.32[13] in samples not subjected to thermal treatments. RuO_2 in its anhydrous form is obtained by high temperature annealing, causing massive sintering along crystallization associated with water removal.[12] However, nanostructured RuO_2 exhibits high hydrophilicity and substantially favors the formation of hydrous amorphous oxide, even after thermal treatments[12,13] rendering the presence of $RuO_x(OH)_y$ an inherent property of all oxidized Ru systems. From a structural standpoint, the incorporation of water within the RuO_2 lattice disrupts long-range order and promotes the formation of defective, amorphous or poorly ordered phases. This structural disorder is often accompanied by a high density of coordinatively unsaturated Ru sites and surface hydroxyl groups, which strongly influence surface reactivity. Consequently, hydrous RuO_2 cannot be regarded simply as a hydrated analogue of crystalline RuO_2, but rather as a distinct material with its own structural and chemical identity, which is however poorly predictable.

At the same time, the presence of H_2O allows for the stabilization of surface properties that can be desirable, such as defective sites or relevant functional groups, and can increase the dispersion of Ru nanoparticles. This dual role of structural water, simultaneously complicating the interpretation of material properties while enabling enhanced surface reactivity, has made hydrous RuO_2 a subject of sustained interest across different research communities. In particular, the dynamic nature of water incorporation and removal, which depends on synthesis routes, thermal history and operating environment, introduces an additional degree of freedom for tailoring the physicochemical properties of Ru-based oxides.

Many works in the electrochemical field have been dedicated to the measurement of H_2O content in relation to synthesis and thermal history of Ru based systems, often finding correlations between the hydration level of Ru oxide and the properties expressed by the catalysts.[12,43,45–47] The water content is known to determine the specific capacitance of RuO_2 influencing its supercapacitor behavior.[12,15,45,46] This has proven relevant for tuning its sensitivity towards CO detection for sensors applications. In electrocatalysis, the presence of water in RuO_2 systems is considered desirable as it favors proton conduction and modulates electron transfer kinetics, both useful characteristics for hydrogen evolution reaction (HER) applications.[18,48,49] More recently, it has been proposed that the structural H_2O may be responsible for the stabilization of peroxo groups at the surface of RuO_2, which are considered crucial for the catalytic mechanism of OER.[36,50–52]

In this context, a growing body of recent literature[34,36,40,53,54] has highlighted the importance of local structural motifs and connectivity within RuO_2-based materials for the oxygen evolution reaction. Attention has shifted from ideal crystalline RuO_2 toward disordered, hydrated or dynamically reconstructed structures in which RuO_6 octahedra can adopt different connection modes, such as corner-sharing, edge-sharing and face-sharing configurations. These motifs are associated with distinct Ru–Ru distances, steric environments and reaction pathways, and have been proposed to play a key role in modulating OER activity. Recent studies [40,53] suggest that structural rearrangements occurring under OER conditions promote a transition from vertex-sharing octahedral networks, typical of rutile RuO_2, toward edge-sharing or even face-sharing RuO_6 units (Figure1.2). This evolution is often accompanied by lattice expansion, increased structural flexibility and reduced steric hindrance for oxygenated intermediates, effectively shortening the reaction pathway for O–O bond formation. In this framework, hydrous and amorphous RuO_2 phases are particularly relevant, as the presence of structural water facilitates lattice distortion and enables the stabilization of these highly active motifs under operating conditions. Importantly, these findings reinforce the view of RuO_2 as a dynamically evolving catalyst during OER rather than a static crystalline material. The ability of RuO_2-to undergo reversible structural transformations, driven by hydration, redox processes and applied potential, provides a mechanistic basis for its exceptional activity, while simultaneously contributing to challenges related to stability and dissolution. Understanding the interplay between local octahedral connectivity, hydration and electrochemical environment has therefore become a central theme in contemporary studies of RuO_2-based OER catalysts.

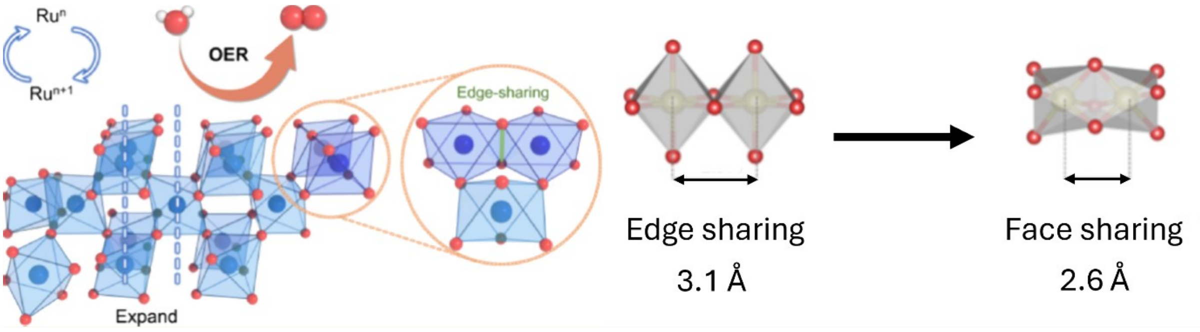

Figure1.2 Schematic representation of the dynamic structural evolution of hydrous RuO_2 under OER conditions. Structural rearrangements involving lattice expansion and the formation of edge-sharing and face-sharing RuO_6 octahedra are highlighted, illustrating how hydration and redox processes promote locally flexible and highly active motifs. Such dynamic behavior emphasizes the non-static nature of RuO_2 under operating conditions and the key role of structural water in enabling highly active configurations. Adapted from references 40 and 53.

While the relevance of structural water and dynamic lattice rearrangements has been most intensively discussed in the context of electrochemical reactions such as OER, similar considerations extend to thermo-catalytic processes. In particular, the presence of hydrous Ru oxide phases and residual lattice water has important implications for the activation, reduction and catalytic behavior of Ru-based systems under hydrogenation conditions. For catalysis of hydrogenation reactions, the presence of structural H_2O is mostly considered a hindrance for activation, namely the reduction of RuO_2 into metallic Ru. As a product of reduction, the presence of bound water is responsible for the delayed reduction of RuO_2. On the other hand, bound H_2O favors increased dispersion and high concentration of defective active sites at Ru nanoparticles surfaces, both desirable qualities for a good catalyst. Moreover, it was shown how enhanced proton conduction through the oxidized lattice could facilitate hydrogenation reactions occurring in H-transfer conditions.[55–57] Therefore, the role of hydrous Ru oxide in catalytic systems is inherently ambivalent and strongly context-dependent. While structural water can slow down reduction processes and complicate catalyst activation, it can also promote high dispersion, defect-rich surfaces and enhanced proton mobility, which are beneficial for specific reaction mechanisms. A detailed understanding of the balance between these effects is essential for rational catalyst design and represents a recurring theme in the study of Ru-based catalytic materials.

1.2.2 Reducibility of Ru oxide

As discussed in the previous section, RuO_2 is very often present in a hydrous, partially amorphous and structurally dynamic form, in which strongly bound water plays a key role in determining structural, redox and transport properties. When moving from oxide-based systems to hydrogenation catalysis, this intrinsic hydration and structural complexity acquire a central importance, as the formation of the catalytically active metallic phase necessarily proceeds through a reduction step. The transformation from RuO_2-like phases to metallic Ru therefore represents a critical transition in the activation of Ru-based catalysts.

Many synthesis parameters can influence reducibility of Ru-based catalysts. It can be increased by addition of reductive agents during the synthesis,[58–61] or by favoring dispersion of the Ru precursor with use of capping agents.[62–65] Residuals from synthesis can modify the reducibility, as well as high temperature calcination. The presence of structural or strongly bound water, characteristic of hydrous RuO_2, is also known to affect both the thermodynamics and the kinetics of reduction, often delaying the formation of fully metallic Ru and modifying the reduction pathway itself.

Beyond a purely phenomenological description, it is important to note that the reduction of RuO_2-like phases to metallic Ru can proceed through different mechanistic pathways, often involving multiple elementary steps. Depending on the initial oxidation state, degree of hydration, morphology and metal–support interaction, the reduction may involve the formation of intermediate oxygen-deficient RuO_{2-x} phases or partially reduced RuO_x species, particularly in the case of hydrous or amorphous oxides. In addition, the nucleation of metallic Ru domains can introduce autocatalytic effects, whereby hydrogen activated on newly formed Ru^0 accelerates the reduction of the remaining oxide. Support-mediated phenomena, such as hydrogen spillover or the stabilization of interfacial Ru-O-support species, can further modify the reduction pathway. As a result, the overall transformation from RuO_2 to Ru^0 often reflects a convolution of chemical reduction, dehydroxylation, structural rearrangement and metal nucleation processes rather than a single elementary event.

Considering the characteristics of Ru based systems and their intrinsic challenges, the study of the reducibility of Ru-based catalysts for hydrogenation reactions remains a key step in their characterization, providing fundamental information to the optimization of the activation step and on the final properties of the active metal phase. The most employed technique to study the reducibility of materials is the temperature programmed reduction in H_2 (H_2-TPR), both at the industrial and academic level.[65–72] The sample is exposed to a H_2 flow while increasing the temperature, triggering the reduction and measuring the H_2 consumption rate as a function of the increasing temperature. The so obtained thermogram bears main aspects about the thermodynamics of the reduction, as well as the peak temperature, associated with the maximum kinetic rate of reduction. The integration of the thermogram allows to measure the total H_2 consumption and perform quantitative analysis against an expected stoichiometry. To measure the true properties of the pristine catalyst, it is not desirable to perform excessive treatment to the samples prior to H_2-TPR experiments. Annealing in oxygen or inert atmosphere, for example, is a treatment often performed prior to H_2-TPR measurement, clearly simplifying the thermogram shape, at the cost of valuable information about the true nature of the catalyst studied. This aspect is particularly critical for Ru-based systems, where hydration state, defect density and partial oxidation can be strongly altered by thermal pretreatments.

The thermograms obtained by H_2-TPR can be regarded as the experimental fingerprint of the reduction mechanisms described above and can, therefore, provide qualitative insights into the reduction process. Sharp peaks indicate fast and collective reduction events, while broader features are signs of higher morphological or chemical heterogeneity within the same phase. When multiple peaks are observed, they can be attributed to the presence of different phases with distinct reduction thermodynamics, but may also arise from the sequential nature of the reduction process itself, such as multi-step reduction pathway or the presence of different families of particles with significant difference in size.[66,68,73–75] Importantly, these different contributions are often experimentally indistinguishable in a standalone H_2-TPR experiment, as similar thermogram features may originate from fundamentally different underlying mechanisms.

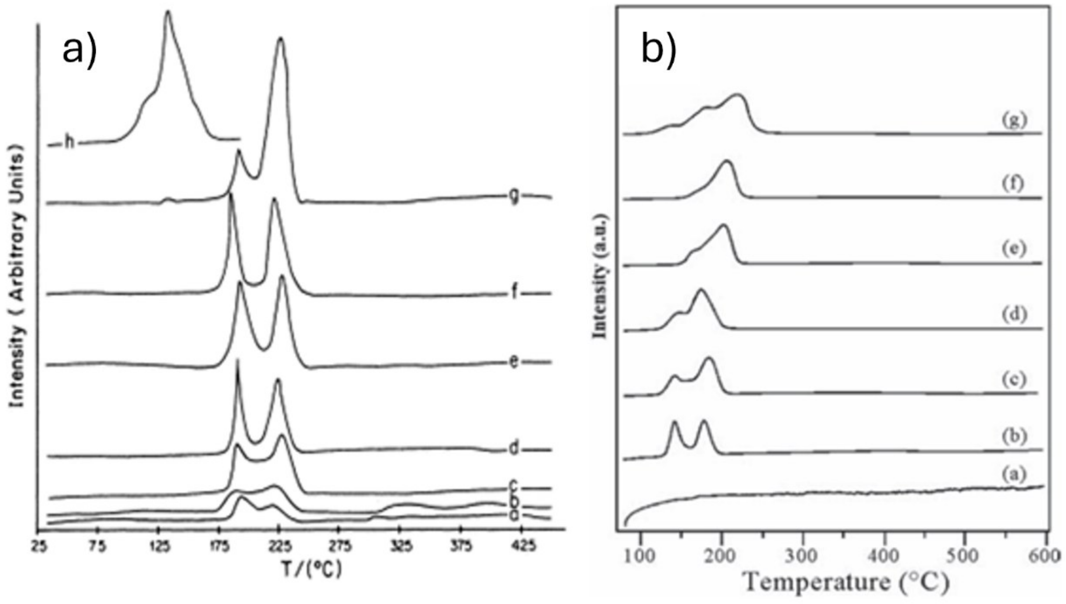

Figure1.3 H_2-TPR profiles of Ru/Al_2O_3 catalysts with varying Ru loading and pretreatment conditions. (a) Comparison between calcined (500 °C) and non-calcined samples highlights the presence of multiple and partially overlapping reduction features associated with different Ru species. (b) Effect of increasing Ru loading on the reduction behavior, showing a progressive shift toward higher-temperature contributions attributed to bulk-like RuO_2. Adapted from references 68 and 75.

The reduction of Ru oxide is typically observed within a relatively broad temperature window, with reported values for complete reduction commonly ranging from about 140 °C to 350 °C depending on precursor chemistry, metal loading, support and thermal history, whereas the need for temperatures above 400 °C is rarely reported.[65,66,68,75–77] Moreover, most thermograms are not characterized by a single sharp feature, but rather by broad or multiple partially overlapping peaks, consistent with the coexistence of more than one reducible Ru species and/or with multi-step reduction processes. In calcined samples, a higher-temperature contribution is often associated with the reduction of bulk-like RuO_2 domains, whereas lower-temperature features are commonly attributed to more easily reducible surface RuO_x species in highly dispersed nanoparticles. In catalysts prepared from $RuCl_3$ precursors and characterized prior to calcination, an additional low-temperature reduction peak is frequently observed and ascribed to precursor-derived Ru^{3+} species that persist after synthesis and washing. Systematic studies further show that increasing Ru loading tends to favor the formation of bulk RuO_2 at the expense of more easily reducible dispersed species, while differences between preparation routes (e.g., incipient wetness impregnation vs deposition–precipitation) can lead to distinct oxide/hydroxide or hydrated RuO_2-like phases with different reducibility. Representative examples of such behavior, illustrating the coexistence of multiple reduction features and their dependence on metal loading and synthesis route, are shown in Figure1.3, where H_2-TPR thermograms of supported Ru catalysts display partially overlapping peaks associated with bulk-like RuO_2, surface RuO_x species and, in some cases, precursor-derived Ru^{3+} contributions.

As a direct consequence of the coexistence of multiple and partially overlapping reduction pathways, the interpretation of H_2-TPR data cannot be reduced to a one-to-one correspondence between a thermogram feature and a single elementary process. Instead, peak position, shape and intensity often reflect the simultaneous contribution of chemical reduction, dehydroxylation, nucleation of metallic Ru domains and transport phenomena. This intrinsic convolution has important implications not only for qualitative interpretation, but also for any attempt to extract quantitative kinetic information from H_2-TPR experiments. Kinetic parameters, such as the activation energy of reduction, can be extracted from H_2-TPR data by performing regression fits on thermograms using established models.[70,78–82] However, this type of analysis requires detailed calculations and careful comparison procedures to obtain reliable results. Thus, the qualitative information that can be extracted from H_2-TPR alone relies strongly on prior knowledge of the system and on the interpretation of the operator. This limitation becomes especially relevant for complex and highly sensitive systems, whose reduction behavior reflects a convolution of structural, chemical and transport-related phenomena. Under these conditions, similar thermogram features may originate from fundamentally different underlying mechanisms, limiting the unambiguous attribution of both qualitative descriptors and kinetic parameters.

To overcome this limitation, the qualitative information inherently hard to extract from H_2-TPR data can be unraveled by suitable coupling to other experimental techniques. The combination of H_2-TPR with complementary structural and spectroscopic methods allows reduction events to be correlated with changes in oxidation state, local structure and dispersion, providing a more robust interpretation of the oxide-to-metal transformation in Ru-based catalysts.

1.2.3 Dispersion of the Ru phase

Once the oxide phase has been reduced to metallic Ru, the dispersion of the metal phase becomes a key parameter for assessing the density and nature of accessible active sites. In Ru-based hydrogenation catalysts, dispersion directly influences not only the number of surface Ru atoms but also the relative abundance of low-coordinated sites, which are often associated with enhanced reactivity. However, the evaluation of dispersion in Ru systems is intrinsically non-trivial due to the strong sensitivity of Ru to its chemical environment and to the dynamic nature of the oxide-to-metal transformation.

A common approach to estimate metal dispersion relies on chemisorption techniques, which probe the uptake of probe molecules irreversibly adsorbed on surface metal atoms under controlled conditions. For Ru-based catalysts, both H_2 and CO have been employed as probe molecules, each presenting specific advantages and limitations. H_2 chemisorption is frequently used to estimate Ru dispersion, owing to the strong interaction between H_2 and metallic Ru and to the direct relevance of hydrogen adsorption for hydrogenation catalysis. Several studies have shown that, when properly conducted, H_2 chemisorption can provide dispersion values that are consistent with independent structural characterization methods such as XRD or electron microscopy.[83–88] At the same time, the interpretation of H_2 uptake on Ru is complicated by the possible formation of surface or subsurface hydride species, as well as by hydrogen spillover onto the support. These phenomena can lead to an overestimation of the number of exposed Ru sites and require careful experimental protocols and data interpretation. Therefore, H_2 chemisorption is often regarded as a semi-quantitative method for Ru dispersion, whose reliability depends strongly on catalyst formulation and measurement conditions.

CO is another widely used probe molecule for dispersion measurements on noble metal catalysts and has also been extensively applied to Ru-based systems.[75,89–92] CO chemisorption benefits from stronger and more localized interaction with Ru surface atoms and from a lower tendency to spill over onto the support. However, for Ru catalysts the use of CO as a quantitative probe is particularly challenging. Numerous studies have demonstrated that the stoichiometry of CO adsorption on Ru is not constant, but varies with particle size, surface structure and oxidation state.[23–26,75,93,94] CO can adsorb on Ru in different geometries, including linear, bridged and multicarbonyl configurations, and the CO/Ru ratio is therefore not uniquely defined. As a result, CO chemisorption on Ru is often less reliable than H_2 chemisorption for the determination of absolute dispersion values.

Within this framework, infrared spectroscopy of adsorbed CO represents a powerful complementary technique, providing qualitative insight into the surface structure and heterogeneity of metallic Ru nanoparticles. The number, position and relative intensity of ν(CO) bands are highly sensitive to the coordination environment of Ru atoms and can be used to distinguish between terrace, edge and defect sites. Highly dispersed Ru nanoparticles typically exhibit multiple CO adsorption bands, reflecting a broad distribution of surface environments, whereas larger particles or extended Ru surfaces often display fewer and sharper spectral features. Importantly, CO adsorption on Ru is not merely a passive probe of surface structure. The strong interaction between CO molecules and low-coordinated Ru atoms can promote the formation of multicarbonyl species and, under certain conditions, induce restructuring, fragmentation or partial oxidation of Ru nanoparticles.[23–26,75,93,94] This phenomenon, often referred to as oxidative or corrosive disruption, introduces additional complexity in the interpretation of both CO chemisorption and CO-IR data. For this reason, CO-based techniques are most effectively employed in a comparative manner, for example to monitor changes in dispersion as a function of reduction conditions, metal loading or support properties, rather than as standalone quantitative tools.

Overall, the reliable assessment of Ru dispersion requires a cautious and integrated approach. Chemisorption measurements provide useful estimates of metal surface exposure but are affected by probe-specific limitations, while spectroscopic techniques such as CO-IR offer detailed qualitative information on surface site distribution and heterogeneity. Combining these methods with structural characterization techniques, such as electron microscopy or X-ray diffraction, is therefore essential to obtain a consistent and physically meaningful description of dispersion in Ru-based catalytic systems.

1.3 Purpose and structure of the PhD thesis

Despite the long-standing industrial relevance of Ru-based catalysts, a unified understanding of how oxidized Ru phases transform into active metallic species, and how this transformation is affected by water, support and synthesis history, is still lacking. In particular, the reducibility of hydrated Ru oxide phases, the nature of intermediate states formed during activation, and the evolution of surface chemistry under working conditions remain open questions. This PhD work addresses these issues by following the transformation of Ru catalysts from their oxidized, hydrated state to the reduced metallic phase through a combination of advanced bulk- and surface-sensitive characterization techniques.

This PhD project is part of the European project Next Generation EU and was co-funded by the Department of Chemistry of the University of Torino and the Catalyst Division of Chimet S.p.A. (https://www.chimet.com), an Italian company leader in the recovery and refining of precious metals. The work here presented was devoted to the study of industrially relevant Ru-based heterogeneous catalysts for hydrogenation reactions, either unsupported or supported on Al_2O_3 or active carbons. In particular, great effort was dedicated to the characterization of the reduction process of Ru oxidized phase and parameters influencing its reducibility.

The discussion is organized to reflect the logical progression of the oxide-to-metal transformation, moving from the nature of the oxidized precursor to bulk reduction pathways, surface chemistry and, finally, the role of water as a key structural and kinetic variable.

In chapter 2 will be presented the synthesis procedure used to obtain all studied catalysts as well as all the characterizations methods employed in this thesis. The experimental protocols chosen to achieve the best coupling among different techniques, together with additional information regarding data treatment, analysis and fitting procedures will also be presented.

In chapter 3 the theme of the Ru oxide-hydroxide phase obtained via deposition-precipitation will be discussed. The goal here was to perform a global characterization of the oxy-hydroxy Ru phase obtained in the pristine catalysts. The characterization of surface oxygenated species and reducibility was carried out on all four industrial Ru based catalysts. The analysis was performed by means of electron microscopy, H_2-TPR measurements and O K-edge near edge X-ray absorption fine structure (NEXAFS). The structural properties of the oxy-hydroxy Ru phase were studied selecting two catalysts as representative systems. In particular, the unsupported and alumina-supported catalysts were chosen as limiting scenarios for metal-support interactions. The analysis was performed by means of high energy X-ray total scattering experiments, extracting both diffraction data (XRD) and pair distribution function data (PDF), and Ru K-edge X-ray absorption spectroscopy (XAS). This preliminary characterization laid the foundation for the interpretation of support-dependent trends observed in all catalysts within this PhD work.

In chapter 4 the focus will be on the reduction process of unsupported and Al_2O_3-supported Ru catalysts. To investigate the origin of the multi-feature profile of thermograms obtained with H_2-TPR, indicating a complex reduction mechanism, the reduction process was monitored with cutting-edge bulk-sensitive synchrotron techniques, such as X-ray total scattering (XRD and PDF) and Ru K-edge X-ray absorption spectroscopy (XAS). All measurements were performed *in situ* using the same protocol of H_2-TPR. The datasets obtained were analyzed with principal components analysis (PCA), followed by multivariate curves resolution (MCR). The evolution of surface species during reduction was instead investigated by coupling surface-sensitive techniques such as transmission Fourier-transform infrared spectroscopy (FTIR) and O K-edge near edge absorption fine structure (NEXAFS), performing *in situ* experiments emulating the H_2-TPR experimental protocol. Information regarding stability, coordination geometry and spillover of Ru hydrides species was collected by means of inelastic neutron scattering (INS) across sequential thermal and chemical treatments. These characterization techniques were coupled with catalytic tests for selective hydrogenation of benzaldehyde to benzyl alcohol.

In chapter 5 the findings made on the Ru/Al_2O_3 catalyst will be extended with a systematic investigation of Ru catalysts supported on commercial alumina and activated carbons prepared by deposition-precipitation under industrially relevant conditions. By combining H_2 temperature-programmed reduction (H_2-TPR), CO pulsed chemisorption and O K-edge near-edge X-ray absorption fine structure (NEXAFS) spectroscopy. Here the goal was to link the support-dependent structure of the hydrated Ru phase to H_2 consumption during reduction and to the evolution of dispersion upon drying and ageing.

Finally, Chapter 6 will sum up all the salient results of the performed analysis, and will drive general conclusions and highlight remaining issues to be addressed in future works.

References

(1) Goodwin, C. M.; Lömker, P.; Degerman, D.; Davies, B.; Shipilin, M.; Garcia-Martinez, F.; Koroidov, S.; Katja Mathiesen, J.; Rameshan, R.; Rodrigues, G. L. S.; Schlueter, C.; Amann, P.; Nilsson, A. Operando Probing of the Surface Chemistry during the Haber–Bosch Process. *Nature* **2024**, *625* (7994), 282–286. https://doi.org/10.1038/s41586-023-06844-5.

(2) Fang, H.; Liu, D.; Luo, Y.; Zhou, Y.; Liang, S.; Wang, X.; Lin, B.; Jiang, L. Challenges and Opportunities of Ru-Based Catalysts toward the Synthesis and Utilization of Ammonia. *ACS Catal.* **2022**, *12* (7), 3938–3954. https://doi.org/10.1021/acscatal.2c00090.

(3) Schmal, M. *Heterogeneous Catalysis and Its Industrial Applications*; **2016**. https://doi.org/10.1007/978-3-319-09250-8.

(4) Müller, T. E. Hydrogenation and Hydrogenolysis with Ruthenium Catalysts and Application to Biomass Conversion. In *Ruthenium*; Ishida, H., Ed.; IntechOpen: Rijeka, **2021**; p Ch. 6. https://doi.org/10.5772/intechopen.97034.

(5) Ciriminna, R.; Pagliaro, M.; Luque, R. Heterogeneous Catalysis under Flow for the 21st Century Fine Chemical Industry. *Green Energy & Environment* **2021**, *6* (2), 161–166. https://doi.org/https://doi.org/10.1016/j.gee.2020.09.013.

(6) Hengne, A. M.; Biradar, N. S.; Rode, C. V. Surface Species of Supported Ruthenium Catalysts in Selective Hydrogenation of Levulinic Esters for Bio-Refinery Application. *Catal. Letters* **2012**, *142* (6), 779–787. https://doi.org/10.1007/s10562-012-0822-4.

(7) Rorrer, J. E.; Beckham, G. T.; Román-Leshkov, Y. Conversion of Polyolefin Waste to Liquid Alkanes with Ru-Based Catalysts under Mild Conditions. *JACS Au* **2021**, *1* (1), 8–12. https://doi.org/10.1021/jacsau.0c00041.

(8) Rorrer, J. E.; Troyano-Valls, C.; Beckham, G. T.; Román-Leshkov, Y. Hydrogenolysis of Polypropylene and Mixed Polyolefin Plastic Waste over Ru/C to Produce Liquid Alkanes. *ACS Sustain. Chem. Eng.* **2021**, *9* (35), 11661–11666. https://doi.org/10.1021/acssuschemeng.1c03786.

(9) Tu, W.; Chu, M.; Wang, X.; Wang, X.; Li, Y.; Yang, W.; Cao, M.; Wang, L.; Li, Y.; Sham, T.-K.; Cui, Y.; Zhang, Q.; Chen, J. SMSI-Induced Charge Transfer for Selective Hydrogenolysis of Polyolefins. *Appl. Catal. B* **2023**, *339*, 123122. https://doi.org/https://doi.org/10.1016/j.apcatb.2023.123122.

(10) Chen, C.; Wu, K.; Ren, H.; Zhou, C.; Luo, Y.; Lin, L.; Au, C.; Jiang, L. Ru-Based Catalysts for Ammonia Decomposition: A Mini-Review. *Energy & Fuels* **2021**, *35* (15), 11693–11706. https://doi.org/10.1021/acs.energyfuels.1c01261.

(11) Petrii, O. A. Pt–Ru Electrocatalysts for Fuel Cells: A Representative Review. *Journal of Solid State Electrochemistry* **2008**, *12* (5), 609–642. https://doi.org/10.1007/s10008-007-0500-4.

(12) Over, H. Surface Chemistry of Ruthenium Dioxide in Heterogeneous Catalysis and Electrocatalysis: From Fundamental to Applied Research. *Chem. Rev.* **2012**, *112* (6), 3356–3426. https://doi.org/10.1021/CR200247N.

(13) McKeown, D. A.; Hagans, P. L.; Carette, L. P. L.; Russell, A. E.; Swider, K. E.; Rolison, D. R. Structure of Hydrous Ruthenium Oxides: Implications for Charge Storage. *J. Phys. Chem. B* **1999**, *103* (23), 4825–4832. https://doi.org/10.1021/jp990096n.

(14) Majumdar, D.; Maiyalagan, T.; Jiang, Z. Recent Progress in Ruthenium Oxide-Based Composites for Supercapacitor Applications. *ChemElectroChem* **2019**, *6* (17), 4343–4372. https://doi.org/https://doi.org/10.1002/celc.201900668.

(15) Adeyemo, A.; Hunter, G.; Dutta, P. K. Interaction of CO with Hydrous Ruthenium Oxide and Development of a Chemoresistive Ambient CO Sensor. *Sens. Actuators B Chem.* **2011**, *152* (2), 307–315. https://doi.org/https://doi.org/10.1016/j.snb.2010.12.027.

(16) Galani, S. M.; Mondal, A.; Srivastava, D. N.; Panda, A. B. Development of RuO2/CeO2 Heterostructure as an Efficient OER Electrocatalyst for Alkaline Water Splitting. *Int. J. Hydrogen Energy* **2020**, *45* (37), 18635–18644. https://doi.org/https://doi.org/10.1016/j.ijhydene.2019.08.026.

(17) Ping, X.; Liu, Y.; Zheng, L.; Song, Y.; Guo, L.; Chen, S.; Wei, Z. Locking the Lattice Oxygen in RuO2 to Stabilize Highly Active Ru Sites in Acidic Water Oxidation. *Nat. Commun.* **2024**, *15* (1), 2501. https://doi.org/10.1038/s41467-024-46815-6.

(18) Cherevko, S.; Geiger, S.; Kasian, O.; Kulyk, N.; Grote, J. P.; Savan, A.; Shrestha, B. R.; Merzlikin, S.; Breitbach, B.; Ludwig, A.; Mayrhofer, K. J. J. Oxygen and Hydrogen Evolution Reactions on Ru, RuO2, Ir, and IrO2 Thin Film Electrodes in Acidic and Alkaline Electrolytes: A Comparative Study on Activity and Stability. *Catal. Today* **2016**, *262*, 170–180. https://doi.org/10.1016/j.cattod.2015.08.014.

(19) Over, H. Ruthenium Dioxide, a Fascinating Material for Atomic Scale Surface Chemistry. *Applied Physics A* **2002**, *75* (1), 37–44. https://doi.org/10.1007/s003390101053.

(20) Jacobsen, C. J. H.; Dahl, S.; Hansen, P. L.; Törnqvist, E.; Jensen, L.; Topsøe, H.; Prip, D. V; Møenshaug, P. B.; Chorkendorff, I. Structure Sensitivity of Supported Ruthenium Catalysts for Ammonia Synthesis. *J. Mol. Catal. A Chem.* **2000**, *163* (1), 19–26. https://doi.org/https://doi.org/10.1016/S1381-1169(00)00396-4.

(21) Fernández, C.; Pezzotta, C.; Gaigneaux, E. M.; Bion, N.; Duprez, D.; Ruiz, P. Disclosing the Synergistic Mechanism in the Catalytic Activity of Different-Sized Ru

Nanoparticles for Ammonia Synthesis at Mild Reaction Conditions. *Catal. Today* **2015**, *251*, 88–95. https://doi.org/https://doi.org/10.1016/j.cattod.2014.11.010.

(22) Fernández, C.; Sassoye, C.; Flores, N.; Escalona, N.; Gaigneaux, E. M.; Sanchez, C.; Ruiz, P. Insights in the Mechanism of Deposition and Growth of RuO2 Colloidal Nanoparticles over Alumina. Implications on the Activity for Ammonia Synthesis. *Appl. Catal. A Gen.* **2015**, *502*, 48–56. https://doi.org/https://doi.org/10.1016/j.apcata.2015.05.023.

(23) Hadjiivanov, K.; Lavalley, J.-C.; Lamotte, J.; Maugé, F.; Saint-Just, J.; Che, M. FTIR Study of CO Interaction with Ru/TiO2Catalysts. *J. Catal.* **1998**, *176* (2), 415–425. https://doi.org/https://doi.org/10.1006/jcat.1998.2038.

(24) Kantcheva, M.; Sayan, S. On the Mechanism of CO Adsorption on a Silica-supported Ruthenium Catalyst. *Catal. Letters* **1999**, *60* (1), 27–38. https://doi.org/10.1023/A:1019082218590.

(25) Solymosi, F.; Raskó, J. An Infrared Study of the Influence of CO Adsorption on the Topology of Supported Ruthenium. *J. Catal.* **1989**, *115* (1), 107–119. https://doi.org/https://doi.org/10.1016/0021-9517(89)90011-0.

(26) Solymosi, F.; Raskó, J. An Infrared Spectroscopic Study of the Formation of Isocyanate Species on RuAl2O3. *J. Catal.* **1977**, *49* (2), 240–243. https://doi.org/https://doi.org/10.1016/0021-9517(77)90260-3.

(27) Todorova, S. Zh.; Kadinov, G. B. Infrared Spectroscopy Study of Adsorption and Coadsorption of Carbon Monoxide and Hydrogen on Ru/Al203. *Research on Chemical Intermediates* **2002**, *28* (4), 291–301. https://doi.org/10.1163/15685670260188601.

(28) Mizushima, T.; Tohji, K.; Udagawa, Y.; Ueno, A. An EXAFS and IR Study of the CO Adsorption-Induced Morphology Change in Ruthenium Catalysts. *J. Am. Chem. Soc.* **1990**, *112* (22), 7887–7893. https://doi.org/10.1021/ja00178a006.

(29) Wang, C.-C. DFT Study of NHx (x = 1−3) Adsorption on RuO2(110) Surfaces. *The Journal of Physical Chemistry C* **2009**, *113* (7), 2816–2821. https://doi.org/10.1021/jp8062355.

(30) Wang, C.-C. DFT Study of NHx (x = 1−3) Adsorption on RuO2(110) Surfaces. *The Journal of Physical Chemistry C* **2009**, *113* (7), 2816–2821. https://doi.org/10.1021/jp8062355.

(31) Seitsonen, A.; Kim, Y. D.; Knapp, M.; Wendt, S.; Over, H. CO Adsorption on the Reduced RuO2(110) Surface: Energetics and Structure. *Physical Review B, v.65, 035413-1-035413-9 (2002)* **2001**, *65*. https://doi.org/10.1103/PhysRevB.65.035413.

(32) Li, T.; Kim, M.; Rai, R.; Liang, Z.; Asthagiri, A.; Weaver, J. F. Adsorption of Alkanes on Stoichiometric and Oxygen-Rich RuO2(110). *Physical Chemistry Chemical Physics* **2016**, *18* (32), 22647–22660. https://doi.org/10.1039/C6CP04195G.

(33) Wang, Y.; Jacobi, K.; Ertl, G. Interaction of NO with the Stoichiometric RuO2(110) Surface. *J. Phys. Chem. B* **2003**, *107* (50), 13918–13924. https://doi.org/10.1021/jp0308108.

(34) Rao, R. R.; Kolb, M. J.; Giordano, L.; Pedersen, A. F.; Katayama, Y.; Hwang, J.; Mehta, A.; You, H.; Lunger, J. R.; Zhou, H.; Halck, N. B.; Vegge, T.; Chorkendorff, I.; Stephens, I. E. L.; Shao-Horn, Y. Operando Identification of Site-Dependent Water Oxidation Activity on Ruthenium Dioxide Single-Crystal Surfaces. *Nat. Catal.* **2020**, *3* (6), 516–525. https://doi.org/10.1038/s41929-020-0457-6.

(35) Jadon, A.; Rossi, C.; Djafari-Rouhani, M.; Estève, A.; Pech, D. Interaction of Hydrogen with the Bulk, Surface and Subsurface of Crystalline RuO2 from First Principles. *Physics Open* **2021**, *7*, 100059. https://doi.org/https://doi.org/10.1016/j.physo.2021.100059.

(36) Di Liberto, G.; Pacchioni, G.; Shao-Horn, Y.; Giordano, L. Role of Water Solvation on the Key Intermediates Catalyzing Oxygen Evolution on RuO2. *The Journal of Physical Chemistry C* **2023**, *127* (21), 10127–10133. https://doi.org/10.1021/acs.jpcc.3c02733.

(37) Rao, R. R.; Kolb, M. J.; Hwang, J.; Pedersen, A. F.; Mehta, A.; You, H.; Stoerzinger, K. A.; Feng, Z.; Zhou, H.; Bluhm, H.; Giordano, L.; Stephens, I. E. L.; Shao-Horn, Y. Surface Orientation Dependent Water Dissociation on Rutile Ruthenium Dioxide. *The Journal of Physical Chemistry C* **2018**, *122* (31), 17802–17811. https://doi.org/10.1021/acs.jpcc.8b04284.

(38) Creazzo, F.; Luber, S. Water-Assisted Chemical Route Towards the Oxygen Evolution Reaction at the Hydrated (110) Ruthenium Oxide Surface: Heterogeneous Catalysis via DFT-MD and Metadynamics Simulations. *Chemistry – A European Journal* **2021**, *27* (68), 17024–17037. https://doi.org/https://doi.org/10.1002/chem.202102356.

(39) Siahrostami, S.; Vojvodic, A. Influence of Adsorbed Water on the Oxygen Evolution Reaction on Oxides. *The Journal of Physical Chemistry C* **2015**, *119* (2), 1032–1037. https://doi.org/10.1021/jp508932x.

(40) She, S.; Chen, H.-C.; Chen, C.; Zhu, Y.; Chen, G.; Song, Y.; Xiao, Y.; Lin, Z.; Zu, D.; Peng, L.; Li, H.; Zhu, Y.; Tsang, Y. H.; Huang, H. Regulating Ru–Ru Distance in RuO2 Catalyst by Lattice Hydroxyl for Efficient Water Oxidation. *ACS Nano* **2025**, *19* (19), 18513–18521. https://doi.org/10.1021/acsnano.5c01937.

(41) Karamad, M.; Hansen, H. A.; Rossmeisl, J.; Nørskov, J. K. Mechanistic Pathway in the Electrochemical Reduction of CO2 on RuO2. *ACS Catal.* **2015**, *5* (7), 4075–4081. https://doi.org/10.1021/cs501542n.

(42) Zheng, J. P.; Xin, Y. Characterization of RuO2·xH2O with Various Water Contents. *J. Power Sources* **2002**, *110* (1), 86–90. https://doi.org/10.1016/S0378-7753(02)00234-3.

(43) Chang, K.-H.; Hu, C.-C.; Chou, C.-Y. Textural and Capacitive Characteristics of Hydrothermally Derived RuO2·xH2O Nanocrystallites: Independent Control of Crystal Size and Water Content. *Cheminform* **2007**, *38*. https://doi.org/10.1021/cm0629661.

(44) Balek, V.; Labhsetwar, N.; Mitsuhashi, T.; Haneda, H.; Subrt, J.; Zelenak, V. Study of the Preparation of Ruthenia Based Catalytic Materials by Heating Their Precursors. *J. Mater. Sci.* **2004**, *39*, 3095–3103. https://doi.org/10.1023/B:JMSC.0000025838.19459.ec.

(45) Sugimoto, W.; Yokoshima, K.; Murakami, Y.; Takasu, Y. Charge Storage Mechanism of Nanostructured Anhydrous and Hydrous Ruthenium-Based Oxides. *Electrochim. Acta* **2006**, *52* (4), 1742–1748. https://doi.org/10.1016/j.electacta.2006.02.054.

(46) Sugimoto, W.; Iwata, H.; Yokoshima, K.; Murakami, Y.; Takasu, Y. Proton and Electron Conductivity in Hydrous Ruthenium Oxides Evaluated by Electrochemical Impedance Spectroscopy: The Origin of Large Capacitance. *J. Phys. Chem. B* **2005**, *109*, 7330–7338. https://doi.org/10.1021/jp044252o.

(47) Hu, C.-C.; Chen, W.-C.; Chang, K.-H. How to Achieve Maximum Utilization of Hydrous Ruthenium Oxide for Supercapacitors. *J. Electrochem. Soc.* **2004**, *151* (2), A281. https://doi.org/10.1149/1.1639020.

(48) Yu, J.; He, Q.; Yang, G.; Zhou, W.; Shao, Z.; Ni, M. Recent Advances and Prospective in Ruthenium-Based Materials for Electrochemical Water Splitting. *ACS Catal.* **2019**, *9* (11), 9973–10011. https://doi.org/10.1021/ACSCATAL.9B02457.

(49) Lee, J.; Sher Shah, S. A.; Yoo, P. J.; Lim, B. Hydrous RuO2 Nanoparticles as Highly Active Electrocatalysts for Hydrogen Evolution Reaction. *Chem. Phys. Lett.* **2017**, *673*, 89–92. https://doi.org/10.1016/J.CPLETT.2017.02.029.

(50) Zhang, J.; Fu, X.; Kwon, S.; Chen, K.; Liu, X.; Yang, J.; Sun, H.; Wang, Y.; Uchiyama, T.; Uchimoto, Y.; Li, S.; Li, Y.; Fan, X.; Chen, G.; Xia, F.; Wu, J.; Li, Y.; Yue, Q.; Qiao, L.; Su, D.; Zhou, H.; Goddard, W. A.; Kang, Y. Tantalum-Stabilized Ruthenium Oxide Electrocatalysts for Industrial Water Electrolysis. *Science (1979).* **2025**, *387* (6729), 48–55. https://doi.org/10.1126/science.ado9938.

(51) Shi, Z.; Li, J.; Wang, Y.; Liu, S.; Zhu, J.; Yang, J.; Wang, X.; Ni, J.; Jiang, Z.; Zhang, L.; Wang, Y.; Liu, C.; Xing, W.; Ge, J. Customized Reaction Route for Ruthenium Oxide towards Stabilized Water Oxidation in High-Performance PEM Electrolyzers. *Nat. Commun.* **2023**, *14* (1), 843. https://doi.org/10.1038/s41467-023-36380-9.

(52) Tang, J.; Guan, D.; Xu, H.; Zhao, L.; Arshad, U.; Fang, Z.; Zhu, T.; Kim, M.; Pao, C.-W.; Hu, Z.; Ge, J.; Shao, Z. Undoped Ruthenium Oxide as a Stable Catalyst for the Acidic

Oxygen Evolution Reaction. *Nat. Commun.* **2025**, *16* (1), 801. https://doi.org/10.1038/s41467-025-56188-z.

(53) Donakowski, M. D.; Mansour, A. N.; Pala, I. R.; Chervin, C. N.; DeSario, P. A.; Long, J. W.; Rolison, D. R. Trapping a Ru2O3 Corundum-like Structure at Ultrathin, Disordered RuO2 Nanoskins Expressed in 3D. *The Journal of Physical Chemistry C* **2018**, *122* (50), 28895–28900.

(54) Deka, N.; Jones, T. E.; Falling, L. J.; Sandoval-Diaz, L.-E.; Lunkenbein, T.; Velasco-Velez, J.-J.; Chan, T.-S.; Chuang, C.-H.; Knop-Gericke, A.; Mom, R. V. On the Operando Structure of Ruthenium Oxides during the Oxygen Evolution Reaction in Acidic Media. *ACS Catal.* **2023**, *13* (11), 7488–7498. https://doi.org/10.1021/acscatal.3c01607.

(55) Yang, H. J.; Redington, M.; Miller, D. P.; Zurek, E.; Kim, M.; Yoo, C.-S.; Lim, S. Y.; Cheong, H.; Chae, S.-A.; Ahn, D.; Hur, N. H. New Monoclinic Ruthenium Dioxide with Highly Selective Hydrogenation Activity. *Catal. Sci. Technol.* **2022**, *12* (21), 6556–6565. https://doi.org/10.1039/D2CY00815G.

(56) Shangguan, J.; Hensley, A. J. R.; Gradiski, M. V; Pfriem, N.; McEwen, J.-S.; Morris, R. H.; Chin, Y.-H. C. The Role of Protons and Hydrides in the Catalytic Hydrogenolysis of Guaiacol at the Ruthenium Nanoparticle–Water Interface. *ACS Catal.* **2020**, *10* (20), 12310–12332. https://doi.org/10.1021/acscatal.0c01963.

(57) Knapp, M.; Crihan, D.; Seitsonen, A.; Over, H. Hydrogen Transfer Reaction on the Surface of an Oxide Catalyst. *J. Am. Chem. Soc.* **2005**, *127*, 3236–3237. https://doi.org/10.1021/ja043355h.

(58) Furusawa, T.; Shirasu, M.; Sugiyama, K.; Sato, T.; Itoh, N.; Suzuki, N. Preparation of Ru/ZrO2 Catalysts by NaBH4 Reduction and Their Catalytic Activity for NH3 Decomposition To Produce H2. *Ind. Eng. Chem. Res.* **2016**, *55* (50), 12742–12749. https://doi.org/10.1021/acs.iecr.6b03265.

(59) Cao, N.; Luo, W.; Cheng, G. One-Step Synthesis of Graphene Supported Ru Nanoparticles as Efficient Catalysts for Hydrolytic Dehydrogenation of Ammonia Borane. *Int. J. Hydrogen Energy* **2013**, *38* (27), 11964–11972. https://doi.org/10.1016/J.IJHYDENE.2013.06.125.

(60) Krajczewski, J.; Ambroziak, R.; Kudelski, A. Formation and Selected Catalytic Properties of Ruthenium, Rhodium, Osmium and Iridium Nanoparticles. *RSC Adv.* **2022**, *12* (4), 2123–2144. https://doi.org/10.1039/D1RA07470A.

(61) Patharkar, R.; Nandanwar, S.; Chakraborty, M. Synthesis of Colloidal Ruthenium Nanocatalyst by Chemical Reduction Method. *J. Chem.* **2013**, *2013*. https://doi.org/10.1155/2013/831694.

(62) Simakova, I. L.; Demidova, Yu. S.; Gläsel, J.; Murzina, E. V; Schubert, T.; Prosvirin, I. P.; Etzold, B. J. M.; Murzin, D. Yu. Controlled Synthesis of PVP-Based Carbon-

Supported Ru Nanoparticles: Synthesis Approaches, Characterization, Capping Agent Removal and Catalytic Behavior. *Catal. Sci. Technol.* **2016**, *6* (24), 8490–8504. https://doi.org/10.1039/C6CY02086K.

(63) Chen, G.; Zhang, J.; Gupta, A.; Rosei, F.; Ma, D. Shape-Controlled Synthesis of Ruthenium Nanocrystals and Their Catalytic Applications. *New Journal of Chemistry* **2014**, *38* (5), 1827–1833. https://doi.org/10.1039/C3NJ01155K.

(64) Villaverde-Cantizano, G.; Laurenti, M.; Rubio-Retama, J.; Contreras-Cáceres, R. Reducing Agents in Colloidal Nanoparticle Synthesis – an Introduction. In *Reducing Agents in Colloidal Nanoparticle Synthesis*; Mourdikoudis, S., Ed.; The Royal Society of Chemistry, **2021**; p 0. https://doi.org/10.1039/9781839163623-00001.

(65) Navarro-Jaén, S.; Navarro, J. C.; Bobadilla, L. F.; Centeno, M. A.; Laguna, O. H.; Odriozola, J. A. Size-Tailored Ru Nanoparticles Deposited over γ-Al2O3 for the CO2 Methanation Reaction. *Appl. Surf. Sci.* **2019**, *483*, 750–761. https://doi.org/https://doi.org/10.1016/j.apsusc.2019.03.248.

(66) Balint, I.; Miyazaki, A.; Aika, K. Methane Reaction with NO over Alumina-Supported Ru Nanoparticles. *J. Catal.* **2002**, *207* (1), 66–75. https://doi.org/https://doi.org/10.1006/jcat.2001.3489.

(67) Reddy, P. S. S.; Pasha, N.; Chalapathi Rao, M. G. V; Lingaiah, N.; Suryanarayana, I.; Sai Prasad, P. S. Direct Decomposition of Nitrous Oxide over Ru/Al2O3 Catalysts Prepared by Deposition–Precipitation Method. *Catal. Commun.* **2007**, *8* (9), 1406–1410. https://doi.org/https://doi.org/10.1016/j.catcom.2006.11.039.

(68) Pavan Kumar, V.; Priya, S. S.; Harikrishna, Y.; Kumar, A.; Chary, K. V. R. Catalytic Functionalities of Nano Ruthenium/γ-Al2O3 Catalysts for the Vapour Phase Hydrogenolysis of Glycerol. *J. Nanosci. Nanotechnol.* **2016**, *16* (2), 1952–1960.

(69) Ju, X.; Liu, L.; Yu, P.; Guo, J.; Zhang, X.; He, T.; Wu, G.; Chen, P. Mesoporous Ru/MgO Prepared by a Deposition-Precipitation Method as Highly Active Catalyst for Producing COx-Free Hydrogen from Ammonia Decomposition. *Appl. Catal. B* **2017**, *211*, 167–175. https://doi.org/https://doi.org/10.1016/j.apcatb.2017.04.043.

(70) Monti, D. A. M.; Baiker, A. Temperature-Programmed Reduction. Parametric Sensitivity and Estimation of Kinetic Parameters. *J. Catal.* **1983**, *83* (2), 323–335. https://doi.org/https://doi.org/10.1016/0021-9517(83)90058-1.

(71) Chapter 11 Temperature Programmed Reduction and Sulphiding. In *Studies in Surface Science and Catalysis*; Moulijn, J. A., van Leeuwen, P. W. N. M., van Santen, R. A., Eds.; Elsevier, **1993**; Vol. 79, pp 401–417. https://doi.org/https://doi.org/10.1016/S0167-2991(08)63815-X.

(72) Da Ros, S.; Valter Flores, K. A.; Schwaab, M.; Barbosa-Coutinho, E.; Fernandes, N. R. C.; Pinto, J. C. Phenomenological Approaches for Quantitative Temperature-Programmed Reduction (TPR) and Desorption (TPD) Analysis. *Journal of Industrial*

and Engineering Chemistry **2021**, *94*, 425–434. https://doi.org/https://doi.org/10.1016/j.jiec.2020.11.018.

(73) Balaraju, M.; Rekha, V.; Devi, B. L. A. P.; Prasad, R. B. N.; Prasad, P. S. S.; Lingaiah, N. Surface and Structural Properties of Titania-Supported Ru Catalysts for Hydrogenolysis of Glycerol. *Appl. Catal. A Gen.* **2010**, *384* (1), 107–114. https://doi.org/https://doi.org/10.1016/j.apcata.2010.06.013.

(74) Garcia Garcia, F.; Fernández-García, M.; Newton, M.; Rodriguez-Ramos, I.; Ruiz, A. Following the Evolution of Ru/Activated Carbon Catalysts during the Decomposition–Reduction of the Ru(NO)(NO. *ChemCatChem* **2013**, *5*. https://doi.org/10.1002/cctc.201300065.

(75) Betancourt, P.; Rives, A.; Hubaut, R.; Scott, C.; Goldwasser, J. A Study of the Ruthenium–Alumina System. *Applied Catalysis A-general - APPL CATAL A-GEN* **1998**, *170*, 307–314. https://doi.org/10.1016/S0926-860X(98)00061-1.

(76) García-García, F. R.; Fernández-García, M.; Newton, M. A.; Rodríguez-Ramos, I.; Guerrero-Ruiz, A. Following the Evolution of Ru/Activated Carbon Catalysts during the Decomposition–Reduction of the Ru(NO)(NO3)3 Precursor. *ChemCatChem* **2013**, *5* (8), 2446–2452. https://doi.org/https://doi.org/10.1002/cctc.201300065.

(77) García-García, F. R.; Gallegos-Suarez, E.; Fernández-García, M.; Guerrero-Ruiz, A.; Rodríguez-Ramos, I. Understanding the Role of Oxygen Surface Groups: The Key for a Smart Ruthenium-Based Carbon-Supported Heterogeneous Catalyst Design and Synthesis. *Appl. Catal. A Gen.* **2017**, *544*, 66–76. https://doi.org/https://doi.org/10.1016/j.apcata.2017.06.030.

(78) Kanervo, J. M.; Krause, A. O. I. Characterisation of Supported Chromium Oxide Catalysts by Kinetic Analysis of H2-TPR Data. *J. Catal.* **2002**, *207* (1), 57–65. https://doi.org/10.1006/JCAT.2002.3531.

(79) Hurst, N. W.; Gentry, S. J.; Jones, A. Temperature Programmed Reduction. *Catalysis Reviews* **1982**, *24* (2), 233–309. https://doi.org/10.1080/03602458208079654.

(80) Kissinger, H. E. Reaction Kinetics in Differential Thermal Analysis. *Anal. Chem.* **1957**, *29* (11), 1702–1706. https://doi.org/10.1021/AC60131A045.

(81) Avrami, M. Kinetics of Phase Change. I: General Theory. *J. Chem. Phys.* **1939**, *7* (12), 1103–1112. https://doi.org/10.1063/1.1750380.

(82) Ehrhardt, K.; Richter, M.; Roost, U.; Öhlmann, G. Temperature Programmed Reduction of Chromium Impregnation Catalysts: Mathematical Treatment of Complex Reduction Profiles. *Appl. Catal.* **1985**, *17* (1), 23–45. https://doi.org/10.1016/S0166-9834(00)82700-1.

(83) Busca, G.; Spennati, E.; Riani, P.; Garbarino, G. Properties, Industrial Applications and Future Perspectives of Catalytic Materials Based on Nickel and Alumina: A Critical Review. *Catalysts* **2024**, *14* (8). https://doi.org/10.3390/catal14080552.

(84) Aika, K.; Miyazaki, A.; Balint, I. CHEMICAL AND MORPHOLOGICAL EVOLUTION OF SUPPORTED Ru NANOPARTICLES DURING OXIDATIVE CONVERSION OF METHANE. *Reaction Kinetics & Catalysis Letters* **2003**, *80* (1), 81–87.

(85) Balint, I.; Miyazaki, A.; Aika, K. I. The Relevance of Ru Nanoparticles Morphology and Oxidation State to the Partial Oxidation of Methane. *J. Catal.* **2003**, *220* (1), 74–83. https://doi.org/10.1016/S0021-9517(03)00279-3.

(86) Zawadzki, M.; Okal, J. Synthesis and Structure Characterization of Ru Nanoparticles Stabilized by PVP or γ-Al2O3. *Mater. Res. Bull.* **2008**, *43* (11), 3111–3121. https://doi.org/10.1016/J.MATERRESBULL.2007.11.006.

(87) Okal, J.; Zawadzki, M.; Kepiński, L.; Krajczyk, L.; Tylus, W. The Use of Hydrogen Chemisorption for the Determination of Ru Dispersion in Ru/γ-Alumina Catalysts. *Appl. Catal. A Gen.* **2007**, *319*, 202–209. https://doi.org/10.1016/J.APCATA.2006.12.005.

(88) Berthoud, R.; Délichère, P.; Gajan, D.; Lukens, W.; Pelzer, K.; Basset, J. M.; Candy, J. P.; Copéret, C. Hydrogen and Oxygen Adsorption Stoichiometries on Silica Supported Ruthenium Nanoparticles. *J. Catal.* **2008**, *260* (2), 387–391. https://doi.org/10.1016/J.JCAT.2008.10.010.

(89) Tolek, W.; Nanthasanti, N.; Pongthawornsakun, B.; Praserthdam, P.; Panpranot, J. Effects of TiO2 Structure and Co Addition as a Second Metal on Ru-Based Catalysts Supported on TiO2 for Selective Hydrogenation of Furfural to FA. *Sci. Rep.* **2021**, *11* (1), 9786. https://doi.org/10.1038/s41598-021-89082-x.

(90) Guglielminotti, E.; Boccuzzi, F.; Manzoli, M.; Pinna, F.; Scarpa, M. Ru/ZrO2 Catalysts: I. O2, CO, and NO Adsorption and Reactivity. *J. Catal.* **2000**, *192* (1), 149–157. https://doi.org/10.1006/JCAT.2000.2835.

(91) Masthan, S. K.; Chary, K. V. R.; Rao, P. K. Measurement of Surface Dispersion of Ruthenium on γ-Al2O3 Support by Low-Temperature Oxygen Chemisorption (LTOC) Technique. *J. Catal.* **1990**, *124* (1), 289–292. https://doi.org/10.1016/0021-9517(90)90125-4.

(92) Truszkiewicz, E.; Zegadło, K.; Wojda, D.; Mierzwa, B.; Kępiński, L. The Effect of the Ruthenium Crystallite Size on the Activity of Ru/Carbon Systems in CO Methanation. *Top. Catal.* **2017**, *60* (17), 1299–1305. https://doi.org/10.1007/s11244-017-0815-z.

(93) Chin, S. Y.; Williams, C. T.; Amiridis, M. D. FTIR Studies of CO Adsorption on Al2O3- and SiO2-Supported Ru Catalysts. *J. Phys. Chem. B* **2006**, *110* (2), 871–882. https://doi.org/10.1021/jp053908q.

(94) Todorova, S. Zh.; Kadinov, G. B. Infrared Spectroscopy Study of Adsorption and Coadsorption of Carbon Monoxide and Hydrogen on Ru/Al203. *Research on Chemical Intermediates* **2002**, *28* (4), 291–301. https://doi.org/10.1163/15685670260188601.

Chapter 2

2 Experimental

2.1 Catalysts preparation and storage

The Ru-based catalysts investigated in this work were prepared in the Catalyst Division of Chimet S.p.A. following the pH-controlled precipitation and deposition-precipitation method,[1,2] using $RuCl_3$ as metal precursor and Na_2CO_3 as precipitating agent. All supported catalysts were prepared with a nominal Ru loading of 5 wt%.

The unsupported Ru catalyst, hereby named Ru_{uns}, was obtained by precipitating the $RuCl_3$ precursor in H_2O solution in the absence of any support. The alumina-supported catalyst (RuAl) was prepared in the presence of an industrial alumina (surface area = 121 m^2g^{-1}, pore volume 0.43 cm^3g^{-1}, mixture of δ and θ phases). The catalysts supported on activated carbons (RuCw and RuCch) were prepared using industrial carbons of wood origin differing in activation procedure. Cw was obtained by physical activation with water vapor at high temperatures, whereas Cch was chemically activated by treatment with H_3PO_4. Therefore, the two carbon supports differ not only in specific surface area (948 ± 2 m^2g^{-1} for Cw and 1541 ± 7 m^2g^{-1} for Cch), but also in pore size distribution and in the type and abundance of oxygen-containing surface functional groups. Differences in porosity and surface functionality between Cw and Cch have been discussed in detail elsewhere.[3–6] After deposition–precipitation, RuCw and RuCch were treated in the liquid phase with a mild reducing agent (formic acid or formate salts), following industrial practice.

After filtration, all catalysts were thoroughly washed with deionized water to remove residual chlorides and then dried overnight at 90 °C.

To investigate the effect of post-synthesis drying, a new synthesis of the supported catalysts was performed following the same protocol described above. After washing, the catalysts were divided into two aliquots. One aliquot of each catalyst was kept in the wet state and dried overnight at different temperatures (70–120 °C) immediately prior to characterization. These samples will be denoted further as RuAl(w), RuCw(w) and RuCch(w), where (w) stands for wet. For ageing studies, the second aliquot was dried overnight at 90 °C and stored under ambient conditions for controlled periods of time before characterization.

A summary of the catalysts that will be discussed is provided in Table 2. *1*.

Table 2. 1 Summary of the catalysts studied with relevant synthesis parameters

Sample	**Support**	**Reducing agent**	**T_{dry} overnight (°C)**
Ru_{uns}	-	No	90
RuAl	Al_2O_3	No	90
RuAl(w)	Al_2O_3	No	-
RuCw	Physically AC	Na-formate	90
RuCw(w)	Physically AC	Na-formate	-
RuCch	Chemically AC	Na-formate	90
RuCch(w)	Chemically AC	Na-formate	-

2.2 FE-SEM and HR-TEM measurements

Field emission scanning electron microscopy (FE-SEM) micrographs were collected with a FIB-SEM TESCAN S9000G equipped with a FEG type Schottky electron source with operating energies ranging between 2 and 15 keV. The samples were fixed to a metallic stub covered with carbon tape and sputtered with a Cr layer (2 nm) to enhance their conductivity.

High resolution transmission electron microscopy (HR-TEM) measurements were carried out with a JEOL 3010-UHR instrument equipped with a LaB_6 electron source operating at 300 kV, and a 2k × 2k pixel Gatan US1000 CCD camera. The samples were deposited onto copper grids covered in lacey carbon film without using any solvent, which could react with Ru oxy-hydroxide.

2.3 *In situ* O K-edge NEXAFS spectroscopy and data treatment

In situ Near Edge X-ray Absorption Fine Structure (NEXAFS) spectra at the O K-edge (520 - 560 eV) were collected with a 0.1 eV energy step using a specially designed reactor cell[7] mounted at the APE-HE beamline of the Elettra Synchrotron radiation source (Trieste, Italy). NEXAFS spectra were acquired in Total Electron Yield (TEY) mode by measuring the drain current from the sample with a picoammeter. In a typical experiment, the sample (~10 mg of powder) was hand-pressed into the sample-holder. The reactor cell was closed with a plug containing a SiN membrane transparent to soft X-rays (thickness: 150nm; window area: 0.5x0.5 mm^2). In this configuration, the X-ray beam passes through the SiN membrane and a thin gas layer before reaching the sample. Particular care was taken to minimize the thickness of the gas layer while avoiding any electrical contact between the sample and the membrane, which is critical for stable TEY measurement. Once assembled and electrically connected, the cell was inserted in the ultra-high vacuum (UHV) chamber of the APE-HE beamline. The position of the SiN membrane, and hence the sample, was aligned with respect to the incident the beam by scanning the xy plane with a spatial precision of approximately 5 µm.

The samples were first measured under flowing He at 25°C (50 ml/min) and successively heated up to 200°C under He flow with a temperature ramp of 5 °C/min in order to monitor the dihydroxylation and restructuring of surface oxygen species. After reaching 200 °C, the temperature was lowered back to ambient conditions under He flow, followed by isothermal exposure to a 5% H_2/He mixture at room temperature for 30 min. Subsequently, the hydrogen reduction was carried out by heating the sample up to 200 °C with a temperature ramp of 5 °C/min under continuous flow of the 5% H_2/He mixture, replicating the same thermal and chemical protocol adopted for the *in situ* IR experiments (see below).

During a single experiment, the spectral baseline was observed to vary as a function of both temperature and gas environment. For this reason, the standard pre-edge/post-edge normalization procedure commonly applied in hard X-ray XAS was not suitable. Instead, baseline subtraction was performed using a spline function constrained by selected points in the pre-edge and post-edge regions. The spectra were then normalized to the intensity of the broad feature centered around 540 eV, attributed to transitions involving antibonding O(2p) states hybridized with metal orbitals, and dominated by the features associated with the supports.[8] This procedure compensates for variations in baseline slope and intensity, minimizes normalization artifacts, and ensures reproducibility of the spectral treatment, as shown in Figure 2.1 and Figure 2.2.

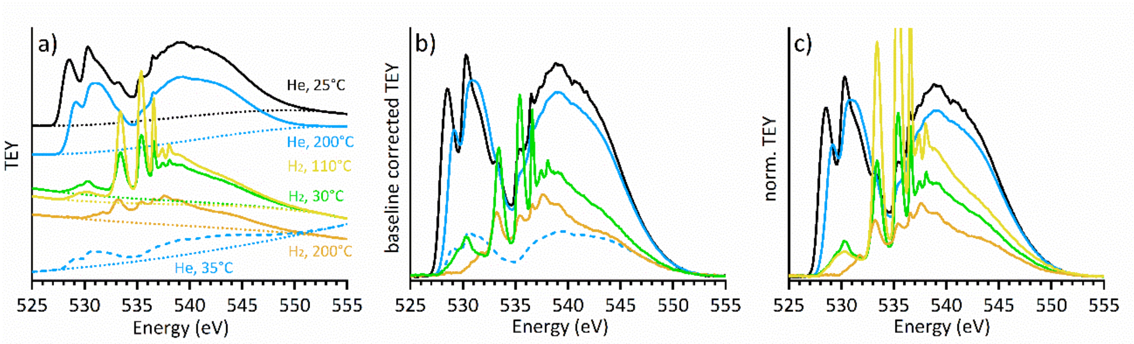

Figure 2.1 Examples of baseline correction and normalization NEXAFS spectra for Ru_{uns} in different atmospheric and temperature conditions. (a) Example spectra and their respective spline baseline references. (b) Baseline subtracted example spectra. (c) Example spectra normalized with respect to the intensity of the absorption peak centered at 540 eV.

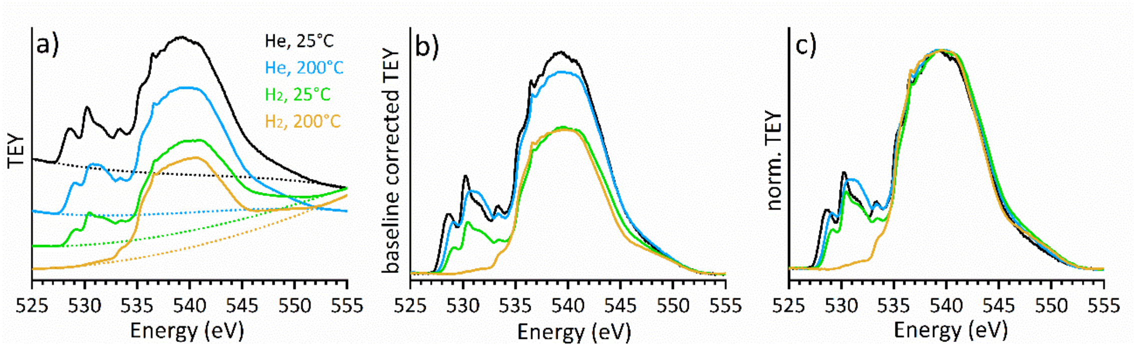

Figure 2.2 Examples of baseline correction and normalization NEXAFS spectra for RuAl in different atmospheric and temperature conditions. (a) Example spectra and their respective spline baseline references. (b) Baseline subtracted example spectra. (c) Example spectra normalized with respect to the intensity of the absorption peak centered at 540 eV.

In order to enable a semi-quantitative comparison of the spectral features associated with the Ru oxy-hydroxide phase in the pristine catalysts, the normalized O K-edge NEXAFS spectra were further analyzed by spectral fitting. The fitting procedure was applied exclusively to spectra collected under identical experimental conditions and after the baseline correction and normalization described above. Each spectrum was fitted using a total of five components. Two broad components were introduced to reproduce the high-energy region dominated by the transitions to antibonding O(2p) states hybridized with metal p orbitals and extending above ~535 eV. In the case of supported catalysts, this bands are associated with support-related transitions, while in the case of Ru_{uns} they are associated to transitions within RuO_2. The spectral region of primary interest (528–535 eV), which contains the well-resolved pre-edge features characteristic of transitions to O(2p)-Ru(4d) orbitals, was instead fitted using three distinct components (A, B and X). All spectral components were modeled using Voigt functions, in order to account simultaneously for instrumental broadening (Gaussian contribution) and intrinsic lifetime broadening of the core-excited states (Lorentzian contribution). During the fitting procedure, the positions and widths of the support-related components were allowed to vary within narrow bounds to accommodate small differences in baseline curvature and support contribution among samples, while the number of components and their functional form were kept constant across all pristine catalysts. This approach ensures internal consistency of the fitting procedure and allows meaningful comparison of the relative intensities of the Ru-related pre-edge features (A, B and X) across different samples, while minimizing cross-correlation between the Ru-related contributions and the broad background associated with the support.

2.4 H_2-TPR measurements and data treatment

H_2-TPR experiments have been carried out with a Micromeritics Autochem 2910 instrument, equipped with thermal conductivity detectors (TCD) and a liquid-nitrogen cryocooler for temperature control below room temperature. A molecular sieve trap was placed between the reactor and the detector to remove water formed during reduction. The detectors were calibrated using a CuO standard to quantify the H_2 consumption. Approximately 100 mg and 10 mg of supported and unsupported catalysts, respectively, were loaded into a quartz reactor and flushed with Ar (50 ml/min) at room temperature for 5 min to remove weakly adsorbed impurities. The temperature was then lowered to -70°C and the sample was exposed to a 5%H_2/Ar flow (50 ml/min) and held at -70°C for 35 min to equilibrate temperature and detector signal. The temperature was subsequently increased to 400°C at a heating rate of 5°C/min.

For RuCw and RuCch, baseline subtraction was required to separate the reduction of the Ru oxy-hydroxy phase from contributions associated with the carbon support. It is well established in the literature that Ru-based catalysts supported on carbon can promote methanation of the carbon support under H_2 at elevated temperatures, leading to additional hydrogen consumption.[9–12] In addition, surface oxygen-containing functional groups on activated carbons undergo reduction at low temperatures, further complicating the interpretation of H_2-TPR profiles. Despite the relevance of this issue, no standardized experimental protocol has been reported to unambiguously separate the reduction of supported Ru species from hydrogen-consuming processes associated with the carbon support. In this work, baseline profiles were obtained by heating the catalysts to 80 °C in He, followed by exposure to pure H_2 for 5 min, as shown in Figure 2.3. This procedure represents a compromise between achieving complete reduction of the Ru phase while preserving the structural features of the carbon supports.

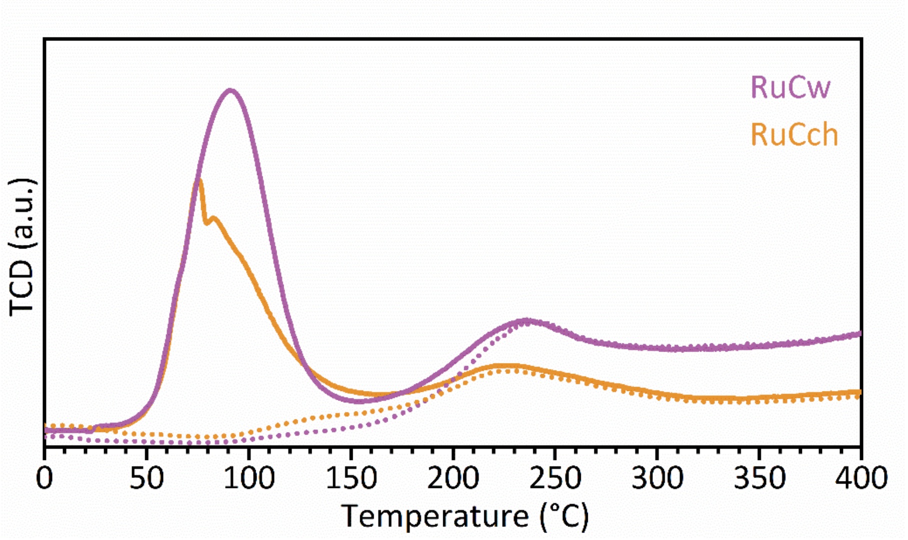

Figure 2.3 H_2-TPR TCD signal (baseline uncorrected) for RuCw (green) and RuCch (violet). The dotted lines indicate the baseline correction curves and follow the same color scheme.

For all samples, the initial analysis of the H_2-TPR data consisted of determining the temperature of the main reduction maxima and the total integrated H_2 consumption, denoted as $H_2(exp)$. To facilitate comparison between catalysts and drying/ageing conditions, the experimental H_2 consumption was normalized to the theoretical value ($H_2(theo)$) expected for complete reduction of RuO_2 according to the stoichiometry $RuO_2 + 2H_2 \rightarrow Ru + 2H_2O$. The resulting ratio, defined as $H_2(ratio) = H_2(exp)/H_2(theo)$ was used throughout the manuscript to quantify deviations from ideal RuO_2 stoichiometry.

For RuAl, where the reduction profiles exhibit sufficiently resolved features, fitting of the H_2-TPR thermograms was performed using Origin software by standard least-squares minimization. Voigt functions were initially employed and subsequently simplified to Gaussian or Lorentzian functions when justified by the fitting results, to avoid overparameterization. The fitting procedure yields the number of contributing components, the position of the maximum temperature for each component, and the integrated area associated with each contribution, which corresponds to a defined amount of consumed H_2. Due to the very broad and poorly defined nature of the reduction features observed for RuCw and RuCch, further peak fitting was not performed for these samples, as any fitting procedure would be highly under constrained and physically ambiguous.

2.5 *In situ* X-ray total scattering and Ru K-edge XAS experiments

In situ high-energy X-ray total scattering and transmission Ru K-edge XAS experiments were performed adopting the same experimental set-up and protocol. Approximately 30 mg of sample were loaded in a flow-through cell specifically designed for *in situ* X-ray experiments, equipped with glassy carbon windows (diameter 13 mm) which ensures negligible residence time and leak-free gas flow through the catalyst bed.[13] A typical measurement protocol was as follows. The sample was equilibrated in a 5% H_2/Ar mixture (25 ml/min total flow) at 25°C for 30 minutes. The temperature was then increased to 400°C with a 5°C/min ramp, using a Eurotherm Nanodac 2.1 temperature controller. The equilibration time was extended compared to H_2-TPR experiments to take into account the different geometry and bigger dead volume of the gas delivery system.

In situ X-ray total scattering experiments were carried out at beamline ID15A (ESRF, Grenoble).[14] The incident beam energy was 98 keV (λ= 0.126515 Å) and the scattered signal was collected with a Pilatus3 2M CdTe (Dectris AG, Switzerland) area detector, positioned at a sample-to-detector distance of 310 mm. The data were collected at a time resolution of 1 pattern/s. A CeO_2 standard powder (NIST 674b) was used for the calibration of detector geometry and for determining the experimental resolution function. To isolate the signals associated with the Ru-phase Δ-XRD patterns were calculated as XRD(Ru_{uns})-XRD(empty cell) and XRD(RuAl)-XRD(Al_2O_3), Figure 2.4 and Figure 2.5 respectively, where XRD(empty cell) and XRD(Al_2O_3) are the patterns of the empty cell and of the alumina support collected under the same thermochemical conditions. To aid visual comparison, the Δ-XRD pattern of RuAl was then normalized for the Ru content to that present in Ru_{uns} (5 wt% vs ca 76 wt%). The two-dimensional diffraction patterns were azimuthally integrated using Python scripts[15,16] and PDFs were obtained using PDFgetx3.[17] Data were corrected for the flat-field response and spatial distortion of the detector, beam polarization, and incident photon flux. The pattern of the empty cell collected under the same thermochemical conditions was subtracted as a background. The *Q*-range used to calculate the PDF was 0.9-20 $Å^{-1}$. For RuAl, Δ-PDF patterns were calculated as PDF(RuAl)-PDF(Al_2O_3) (Figure 2.6).

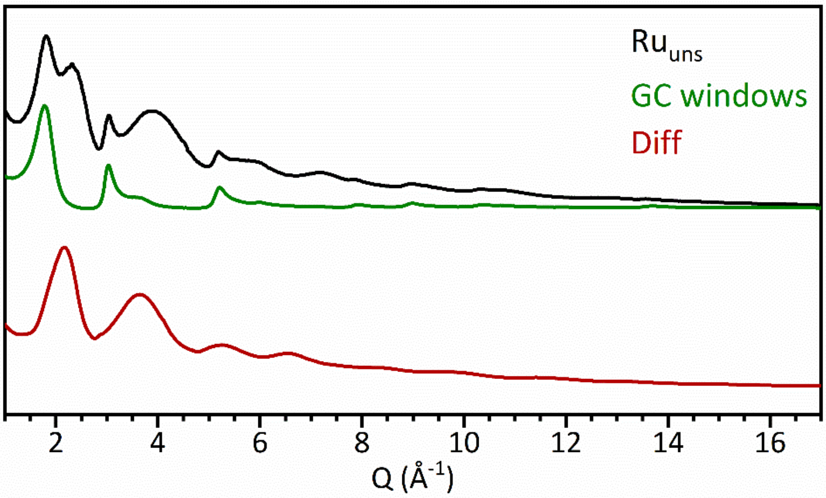

Figure 2.4 XRD pattern of Ru_{uns} compared to that collected with empty cell in the same experimental conditions (Ar flow at 25°C) and their difference.

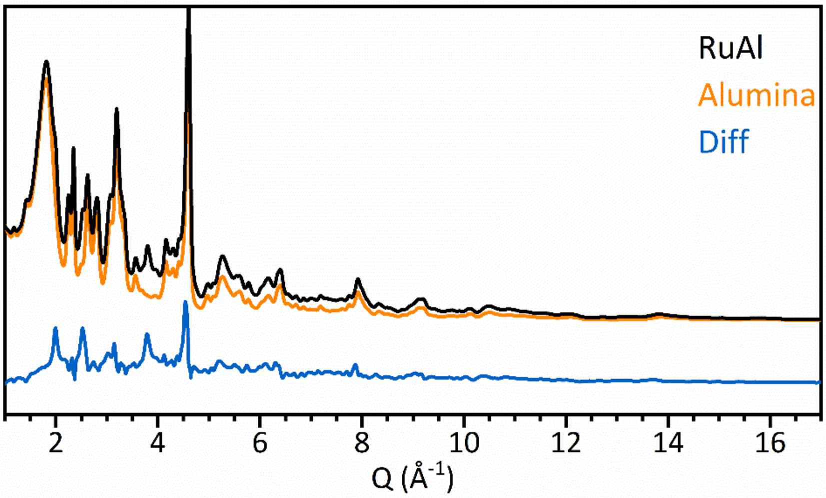

Figure 2.5 XRD patterns of RuAl compared to that of bare alumina collected in the same experimental conditions (5%H_2/Ar flow at 25°C) and their difference. Intensity discrepancies from very intense signals related to alumina were impossible to compensate for and lead to the artefacts around 3 Å^{-1} and 4.5 Å^{-1} in the difference pattern.

The subtraction procedure for RuAl datasets was far from trivial and required interpolation and intensities adjustments to obtain a sensible outcome and compensate for artefacts arising from very intense alumina signals. Very intense signals in the bare alumina are in fact challenging to subtract from the catalyst pattern for two main reasons: i) the presence of Ru oxy-hydroxy nanoparticles in RuAl can cause differences in preferred orientation of alumina crystals leading to slight different intensity in the most intense alumina diffraction peaks; ii) intense alumina signals like the one centered around 4.5 Å^{-1} (corresponding to the 440 plane in γ-Al_2O_3) can overstimulate the area detector leading to a parasitic enhancement of the specific signal. Nevertheless, it was possible to minimize the occurrence of said artefacts maintaining information on the crystalline fraction of Ru oxy-hydroxide NP.

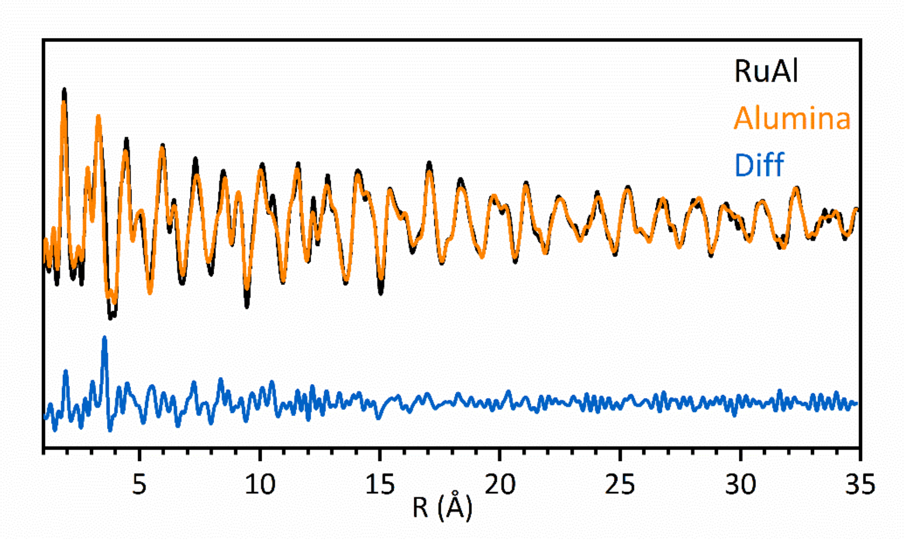

Figure 2.6 PDF radial distributions of RuAl compared to that of bare alumina collected in the same experimental conditions (5%H_2/Ar flow at 25°C) and their difference.

Ru K-edge XAS measurements were carried out in transmission mode at the ID24 DCM beamline (ESRF, Grenoble).[18] The white beam was monochromatized using a fixed exit double crystal monochromator equipped with Si(111) and Si(311) crystals, and two harmonic rejection mirrors positioned between the monochromator and the undulator.[19] Three ionization chambers were employed as detection systems: one before the sample to normalize with respect to the incident beam intensity, one after the sample to measure the X-ray absorption by the sample, and one after a metallic Ru reference to provide correct alignment of the edge position. The spectra were acquired in the 21799 – 23192 eV energy range, with an energy step of 0.5 eV and a total integration time of ~ 7 seconds. The XAS data were aligned and normalized using the Athena software.[20,21] EXAFS data analysis was performed using the Arthemis software.[20,21] The $k^3\chi(k)$ functions were Fourier-Transformed in the $\Delta k = 3 - 15$ Å^{-1} region. Fits were performed in R-space ($\Delta R = 1 - 4$ Å), using the scattering path simulated from the rutile RuO_2 CIF file.

A method combining in sequence principal component analysis (PCA) and Multivariate Curve Resolution-Alternating Least Squares (MCR-ALS) was applied to analyze the XAS data for both RuAl and Ru_{uns}, with the aim to obtain quantitative insights into the local structure modifications during the reduction process. The same approach was also applied to analyze the XRD data for RuAl to investigate the long-range structure modifications, while it was inconclusive for Ru_{uns} due to the amorphous nature of the initial state. The PyFitit software,[22] designed to perform PCA on XAS data, was employed for the first step of the analysis to gain insights on the possible number of primary components that can be extracted from each set of data. The output of the PCA was used as input information for the subsequent MCR-ALS analysis, to determine the nature and to quantify the fraction of each component at each point in time/temperature. The MCR analysis was conducted with the pyMCR Python package.[23] MCR-ALS analysis used as few constraints as possible on the experimental data. The initial-guess spectra/patterns were selected as the first and the last, respectively, for the starting and ending component. The initial-guess spectrum/pattern for the intermediate components was selected choosing the dataset at which PCA with 2 components had the greatest unexplained variance, namely where the model with 2 components failed the most to explain the dataset variance. The only component for which concentration constraints were applied was the Ru metal component. Its concentration at the beginning of the reduction is considered to be null, as confirmed by independent techniques, and it is unambiguously dominant, hence equal to 1, at the end of the reduction event. Therefore, only the first and the last point of the datasets are constrained to have Ru metal concentration equal to 0 and 1 at the start and at the end of the dataset respectively, while for the rest of the dataset its concentration was free to vary. The other two components' concentrations and profiles were not subject to any chosen constraint.

2.6 Catalytic tests

Catalytic tests were carried out at 500 rpm in a 100 mL stainless steel reactor (Parr Instrument, 4560 Mini Reactor System). The reactor was loaded with the selected catalyst, either Ru_{uns} or RuAl, suspended in 40 mL of a 0.1 M benzaldehyde solution in tetrahydrofuran (THF), corresponding to a substrate-to-catalyst molar ratio of 30:1. The system was purged three times with high-purity H_2 (99.99%) to remove atmospheric air. The reactor was then pressurized to 10 bar with high-purity H_2 and heated to the desired reaction temperature.

At the end of the reaction, the system was cooled to 10°C and the pressure was carefully released. The organic phase was then analyzed by off-line gas chromatography using tetradecane as the external standard. Analyses were performed on an Agilent 6890 gas chromatograph equipped with a wide-bore capillary column (CP-WAX 52CB, 60 m × 0.53 mm internal diameter) and a flame ionization detector (FID). Nitrogen was used as the carrier gas at a flow rate of 2 mL/min. The temperature program began with a 5-minute isotherm at 50 °C, followed by a temperature increase of 5 °C/min to 230 °C, held for 2 minutes, then further increased at 15 °C/min to 250 °C and held for 5 minutes.

Conversion and product selectivity were defined and calculated as follows:

$$\text{Conversion } (\%) = \frac{\text{mol of reacted benzaldehyde}}{\text{mol of benzaldehyde feed}} \times 100$$

$$\text{Liquid phase selectivity } (\%) = \frac{\text{mol of specific product in liquid phase}}{\text{sum of mol of all products in liquid phase}} \times 100$$

All compounds observed were calibrated with respect to tetradecane as external standard in order to determine the corresponding response factor within the appropriate concentration range. Carbon balance was evaluated by using GC-FID quantification, with carbon loss found to be below 2% in all catalytic experiments.

2.7 *In situ* FT-IR spectroscopy

The *in situ* transmission IR spectra were acquired with a Bruker INVENIO R FT-IR spectrophotometer, equipped with a mercury cadmium telluride (MCT) cryogenic detector, at a spectral resolution of 2 cm^{-1}. The samples (approximately 5–10 mg) were pressed into self-supporting thin pellets and inserted into the sandwich cell developed by Ensicaen [24] using the dedicated sample holder. The background spectrum was recorded using the empty cell under He flow (50 ml/min) and averaged over 64 scans, while the subsequent spectra were averaged over 32 scans, corresponding to an acquisition rate of approximately 1 spectrum per minute.

In situ dehydration of the catalyst was carried out by heating the sample up to 200 °C under flowing He (50 ml/min) with a temperature ramp of 3 °C/min, followed by a short isothermal hold at 200 °C to ensure effective desorption of physisorbed water and surface hydroxyl groups. The temperature was then lowered to ambient conditions under He flow (50 ml/min), followed by isothermal equilibration under a 5% H_2/He mixture (50 ml/min) for 30 min. The TPR experiment was subsequently performed by increasing the temperature to 200 °C at a rate of 3 °C/min under continuous flow of the 5% H_2/He mixture (50 ml/min).

2.8 INS spectroscopy

The Inelastic Neutron Scattering (INS) experiment were carried out on the IN1 Lagrange (LArge GRaphite ANalyser for Genuine Excitations) spectrometer at the Institute Laue Langevin (ILL, Grenoble, France).[25] Monochromators employing Si(111), Si(311) and

Cu(220) crystals were used to select the incident neutron energy, resulting in an effective beam size on the sample of approximately 3 x 3 cm^2. The scattered neutrons were collected by a pyrolytic graphite (PG) analyzer-detector system, covering a large solid angle of approximately 0.8π ≈ 2.5 Steradians. The analyzer, with a total reflecting surface of ~1 m^2, is arranged around the vertical sample-detector axis and set to reflect neutrons with a fixed average final energy of 4.5 meV. A cooled (70 K) Be filter is positioned in between sample and PG analyzer to suppress higher harmonics. Spectra were collected scanning the energy of the incident neutron beam in the range 4.5 meV to 300 meV. The transformation coefficient from the physical unit of meV used to collect the data and spectroscopic unit of cm-1 used in the plots of this thesis is 8.065.

INS measurements required prior activation of the samples under static conditions. For this purpose, approximately 8 g of catalyst were heated from 25 to 200 °C in a quartz tube connected to a vacuum line under dynamic vacuum. The sample was left to 200 °C until reaching a vacuum as low as 10^{-5} mbar. At that point, the sample was exposed to pure H_2 (~100 mbar) for 30 min, followed by evacuation of the system down to the minimum attainable pressure (~10^{-5} mbar). This H_2 dosing–evacuation cycle was repeated three times to ensure complete reduction of the Ru oxy-hydroxide nanoparticles and removal of the water produced during the reduction. After activation, the samples were transferred and stored in hermetically sealed containers inside a N^2-filled glovebox and subsequently mounted into a dedicated INS measurement cell connected with a gas handling system stick within the glove box to prevent reoxidation prior to measurements. The INS gas handling systems allow control of the atmosphere inside the measurement cell through a static gas-dosing system coupled with a vacuum line. The sample cell was shielded with a Cd mask featuring a 30x18 mm^2 window to define a well-controlled probed surface.

For the INS measurements, samples were either evacuated at the minimum attainable pressure (~10^{-7} mbar) or dosed with pure H_2 (~400 mbar) at ambient temperature, depending on the experimental protocol. Following gas dosing or evacuation, the samples were cooled down to 20 K using a closed-cycle refrigerator, to minimize Debye-Waller factor and so enhance resolution of spectral features. Cooling to cryogenic temperature also stabilizes hydrogen species on the Ru surface and suppresses diffusional motion.

2.9 CO chemisorption measurements and dispersion analysis

CO pulsed chemisorption experiments were carried out using a Micromeritics Autochem 2910 instrument, equipped with TCD detectors. All samples were activated *in situ* by isothermal reduction at 120 °C under pure H_2 for 5 minutes. This short activation step was chosen to minimize structural evolution while ensuring reduction of the Ru oxy-hydroxy phase. After reduction, samples were purged with He (50 ml/min) and cooled to 40 °C. CO was then introduced via a calibrated loop using a sequence of 10 pulses. The amount of CO not adsorbed by the catalyst was monitored by the TCD, and saturation was assumed when successive pulses produced constant peak areas. The total amount of adsorbed CO was calculated from the cumulative difference between the initial pulses and the saturated signal. Dispersion values were calculated assuming a stoichiometric CO/Ru ratio of 1. This value was used solely for comparative purposes, as discussed in the Results and Discussion, and does not imply a one-to-one adsorption stoichiometry on Ru surfaces.

References

(1) Agostini, G.; Groppo, E.; Piovano, A.; Pellegrini, R.; Leofanti, G.; Lamberti, C. Preparation of Supported Pd Catalysts: From the Pd Precursor Solution to the Deposited Pd2+ Phase. *Langmuir* **2010**, *26* (13), 11204–11211. https://doi.org/10.1021/la1005117.

(2) Pellegrini, R.; Leofanti, G.; Agostini, G.; Groppo, E.; Rivallan, M.; Lamberti, C. Pd-Supported Catalysts: Evolution of Support Porous Texture along Pd Deposition and Alkali-Metal Doping. *Langmuir* **2009**, *25* (11), 6476–6485. https://doi.org/10.1021/la900084p.

(3) Vottero, E.; Carosso, M.; Pellegrini, R.; Piovano, A.; Groppo, E. Assessing the Functional Groups in Activated Carbons through a Multi-Technique Approach. *Catal. Sci. Technol.* **2022**, *12* (4), 1271–1288. https://doi.org/10.1039/D1CY01751A.

(4) Lazzarini, A.; Piovano, A.; Pellegrini, R.; Leofanti, G.; Agostini, G.; Rudić, S.; Chierotti, M. R.; Gobetto, R.; Battiato, A.; Spoto, G.; Zecchina, A.; Lamberti, C.; Groppo, E. A Comprehensive Approach to Investigate the Structural and Surface Properties of Activated Carbons and Related Pd-Based Catalysts. *Catal. Sci. Technol.* **2016**, *6* (13), 4910–4922. https://doi.org/10.1039/C6CY00159A.

(5) Piovano, A.; Lazzarini, A.; Pellegrini, R.; Leofanti, G.; Agostini, G.; Rudić, S.; Bugaev, A. L.; Lamberti, C.; Groppo, E. Progress in the Characterization of the Surface Species in Activated Carbons by Means of INS Spectroscopy Coupled with Detailed DFT Calculations. *Advances in Condensed Matter Physics* **2015**, *2015* (1), 803267. https://doi.org/https://doi.org/10.1155/2015/803267.

(6) Pellegrini, R.; Leofanti, G.; Agostini, G.; Groppo, E.; Lamberti, C. Investigation of Carbon and Alumina Supported Pd Catalysts during Catalyst Preparation. *Stud. Surf. Sci. Catal.* **2010**, *175*, 437–440. https://doi.org/10.1016/S0167-2991(10)75079-5.

(7) Castán-Guerrero, C.; Krizmancic, D.; Bonanni, V.; Edla, R.; Deluisa, A.; Salvador, F.; Rossi, G.; Panaccione, G.; Torelli, P. A Reaction Cell for Ambient Pressure Soft X-Ray Absorption Spectroscopy. *Review of Scientific Instruments* **2018**, *89* (5), 054101. https://doi.org/10.1063/1.5019333.

(8) Frati, F.; Hunault, M. O. J. Y.; de Groot, F. M. F. Oxygen K-Edge X-Ray Absorption Spectra. *Chem. Rev.* **2020**, *120* (9), 4056–4110. https://doi.org/10.1021/acs.chemrev.9b00439.

(9) Truszkiewicz, E.; Klimaszewska, K.; Gauze, E.; Gronkiewicz, Z.; Ostrowski, A.; Gertych, A.; Wierzbicki, D.; Alxneit, I. Catalytic CO2 Methanation Over Modified Carbon-Supported Ruthenium: The Influence of the Support Type on the Properties and Activity of the Catalyst. *Top. Catal.* **2025**. https://doi.org/10.1007/s11244-025-02144-6.

(10) Truszkiewicz, E.; Latoszek, K.; Ojrzyńska, M.; Ostrowski, A.; Kępiński, L. Stability of Ruthenium/Carbon Catalytic Materials during Operation in Carbon Monoxide Methanation Process. *Catalysts* **2023**, *13* (12). https://doi.org/10.3390/catal13121518.

(11) Lan, G.; Tang, H.; Zhou, Y.; Han, W.; Liu, H.; Li, X.; Li, Y. Direct Synthesis of Ruthenium-Containing Ordered Mesoporous Carbon with Tunable Embedding Degrees by Using a Boric Acid-Assisted Approach. *ChemCatChem* **2014**, *6* (1), 353–360. https://doi.org/https://doi.org/10.1002/cctc.201300693.

(12) Rodríguez, V. I.; Mendow, G.; Sánchez, B. S.; García, J. R.; Pujro, R. A.; de Miguel, S. R.; Veizaga, N. S. Ruthenium Catalysts Supported on Hydrothermally Treated Carbon from Rice Husk: The Effect of Reduction Temperature on the Hydrogenation Reaction of Levulinic Acid to γ-Valerolactone. *Processes* **2023**, *11* (5). https://doi.org/10.3390/pr11051421.

(13) Bonavia D.; Ricchebuono A.; Lazzarini P.; Vottero E.; Pellegrini R.; Piovano A.; Chizallet C.; Raybaud P.; Dejoie C.; Alxneit I.; Checchia S.; Ferri D.; Groppo E. Pt Nanoparticles Breathe and Reversibly Detach from Al2O3 in Hydrogen. *Nat. Commun.* **2025**, No. accepted.

(14) Bonavia, D.; Ferri, D.; Lazzarini, P.; Piovano, A.; Ricchebuono, A. CH-6702 - Structural Ductility in Ru/Al2O3 Catalysts Induced by H2 and CO: Gas-Phase vs. Liquid Phase Conditions. **2024**. https://doi.org/10.15151/ESRF-ES-1430230544.

(15) Knudsen, E. B.; Sørensen, H. O.; Wright, J. P.; Goret, G.; Kieffer, J. FabIO: Easy Access to Two-Dimensional X-Ray Detector Images in Python. *J. Appl. Crystallogr.* **2013**, *46* (2), 537–539. https://doi.org/10.1107/S0021889813000150.

(16) Ashiotis, G.; Deschildre, A.; Nawaz, Z.; Wright, J. P.; Karkoulis, D.; Picca, F. E.; Kieffer, J. The Fast Azimuthal Integration Python Library: PyFAI. *J. Appl. Crystallogr.* **2015**, *48* (2), 510–519. https://doi.org/10.1107/S1600576715004306.

(17) Juhás, P.; Davis, T.; Farrow, C. ~L.; Billinge, S. ~J. ~L. PDFgetX3: A Rapid and Highly Automatable Program for Processing Powder Diffraction Data into Total Scattering Pair Distribution Functions. *J. Appl. Crystallogr.* **2013**, *46* (2), 560–566. https://doi.org/10.1107/S0021889813005190.

(18) Bonavia, D.; Checchia, S.; Deplano, G.; Giacchero, A.; Lazzarini, P.; Ricchebuono, A.; Seminerio, E. CH-6850 - "Adsorbate-Induced Phenomena at Pt- and Ru-Based Catalysts in Liquid Phase." **2024**. https://doi.org/10.15151/ESRF-ES-1581094387.

(19) Rosa, A. D.; G., G.; J. E., R.; E., M.; J., J.; D., B.; S., P.; G., B.; A., M.; C., C.; F., P.; S., A.; C., M.; F., O.; X., Z.; N., I.; T., S.; S., B.; R., T.; J.-A., H.; C. J. S., H.; S., D.; G., M.; D., A.; S., P.; B., W.; M., M.; G., K.; W., M.; M., W.; A., D. C.; M. A., B.; T., I.; K. A., L.; and Mathon, O. New Opportunities for High Pressure X-Ray Absorption Spectroscopy at ID24-DCM and BM23 with the Extremely Brilliant Source of the ESRF. *High Press. Res.* **2024**, *44* (3), 248–276. https://doi.org/10.1080/08957959.2024.2364281.

(20) Newville, M. IFEFFIT : Interactive XAFS Analysis and FEFF Fitting. *J. Synchrotron Radiat.* **2001**, *8* (2), 322–324. https://doi.org/https://doi.org/10.1107/S0909049500016964.

(21) Ravel, B.; Newville, M. ATHENA, ARTEMIS, HEPHAESTUS: Data Analysis for X-Ray Absorption Spectroscopy Using IFEFFIT. *J. Synchrotron Radiat.* **2005**, *12* (4), 537–541. https://doi.org/10.1107/S0909049505012719.

(22) Martini, A.; Guda, S. A.; Guda, A. A.; Smolentsev, G.; Algasov, A.; Usoltsev, O.; Soldatov, M. A.; Bugaev, A.; Rusalev, Yu.; Lamberti, C.; Soldatov, A. V. PyFitit: The Software for Quantitative Analysis of XANES Spectra Using Machine-Learning Algorithms. *Comput. Phys. Commun.* **2020**, *250*, 107064. https://doi.org/https://doi.org/10.1016/j.cpc.2019.107064.

(23) Camp Jr, C. PyMCR: A Python Library for MultivariateCurve Resolution Analysis with Alternating Regression (MCR-AR). *J. Res. Natl. Inst. Stand. Technol.* **2019**, *124*. https://doi.org/10.6028/jres.124.018.

(24) Wuttke, S.; Bazin, P.; Vimont, A.; Serre, C.; Seo, Y.-K.; Hwang, Y. K.; Chang, J.-S.; Férey, G.; Daturi, M. Discovering the Active Sites for C3 Separation in MIL-100(Fe) by Using Operando IR Spectroscopy. *Chemistry – A European Journal* **2012**, *18* (38), 11959–11967. https://doi.org/https://doi.org/10.1002/chem.201201006.

(25) Piovano Andrea; Bonavia Daniele; Checchia Stefano; Jimenez Ruiz Monica; Lazzarini Paolo; Ricchebuono Alberto; Vottero Eleonora. *ILL proposal n.7-05-568*. **2023**.

Chapter 3

3 The Ru oxide-hydroxide phase obtained with deposition-precipitation method

3.1 Chapter overview and scope

In this chapter the theme of the Ru oxide-hydroxide phase will be discussed addressing a pivotal question regarding the characterization heterogeneous catalysts obtained via deposition-precipitation: what is the true structural and chemical nature of the oxidized Ru phase and how do support and synthesis conditions influence its reducibility? The goal is to perform a global characterization of the oxy-hydroxy Ru phase obtained in the pristine catalysts coupling bulk- and surface-sensitive techniques to electron microscopy qualitative observations and H_2-TPR measurements. This experimental approach allows for a coherent description of the as-synthetized oxy-hydroxide phase, laying the foundation for the interpretation of the reduction process.

While O K-edge NEXAFS spectroscopy was performed on all the four catalysts presented in this work, for the structural characterization performed by means of X-ray total scattering and X-ray absorption experiments, only two catalysts were selected as references, namely RuAl and Ru_{uns}, as they represent the limit scenarios in terms of metal-support interactions. The selection of bulk techniques having complementary sensitivities towards local and long-range order allowed for the complete description of inherently heterogeneous systems where very small nanoparticles coexist with larger aggregates. The surface properties of the four catalysts have marked support-induced differences; however, they preserve a common theme: a high level of hydration and/or protonation of the oxygenated surface species leads to the stabilization of the uncommon peroxo Ru-O-O groups.

The reducibility of the four catalysts was measured by means of H_2-TPR, highlighting how the oxy-hydroxide phase obtained by deposition-precipitation method is not reduced through a simple redox mechanism, since all samples exhibit complex thermograms. Support-induced differences in the oxy-hydroxide Ru phase have a direct influence on the reduction process, effectively describing kinetic H_2-TPR fingerprints for each catalyst. Furthermore, H_2-TPR revealed that and that the consistent overconsumption measured across all samples can be explained by the presence of peroxo species.

3.2 Morphological features of pristine catalysts

Figure 3.1 shows representative FE-SEM images of Ru_{uns} at increasing magnifications, revealing irregularly shaped particles composed of aggregated nanostructures a few tens of nanometers in size. This indicates that during the precipitation the growth of Ru oxy-hydroxy species into large particles is hindered, in agreement with the reported stability of colloidal Ru oxy-hydroxy in H_2O.[1] Moreover, these images suggest that the mild conditions of the drying thermal treatment (90° C) were not sufficient to cause massive sintering.

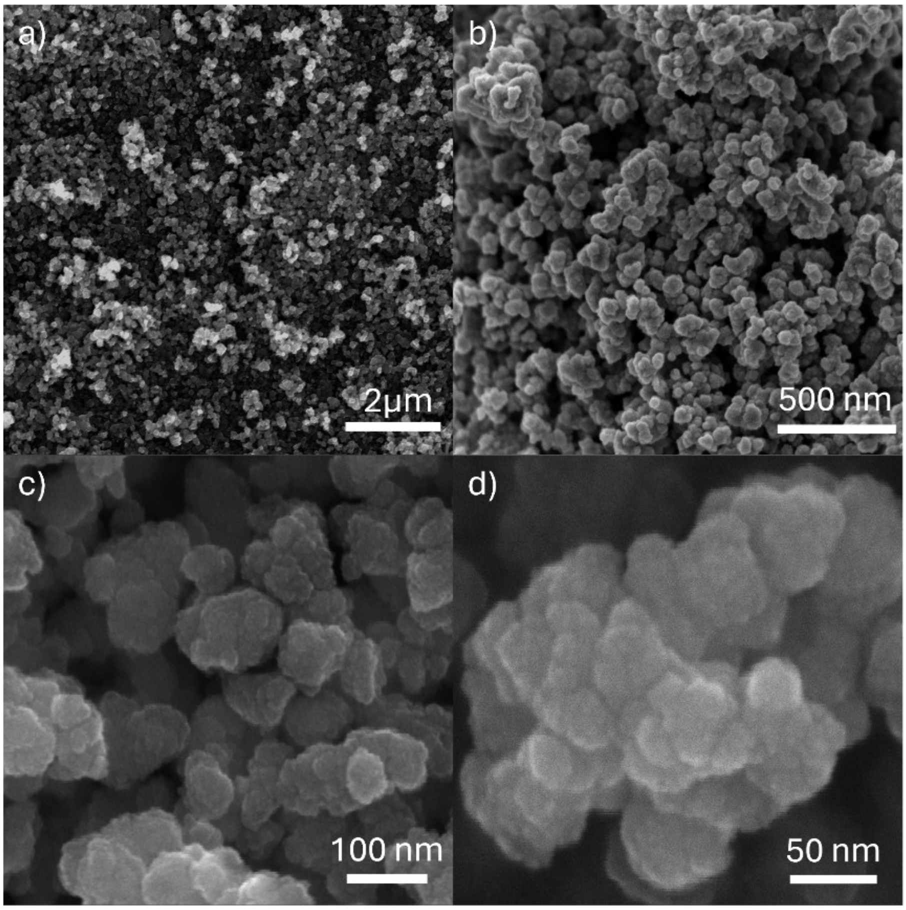

Figure 3.1 Representative FE-SEM pictures of Ru_{uns} at magnifications: (a) 30kx, (b) 150kx, (c) 500kx and (d) 1090kx.

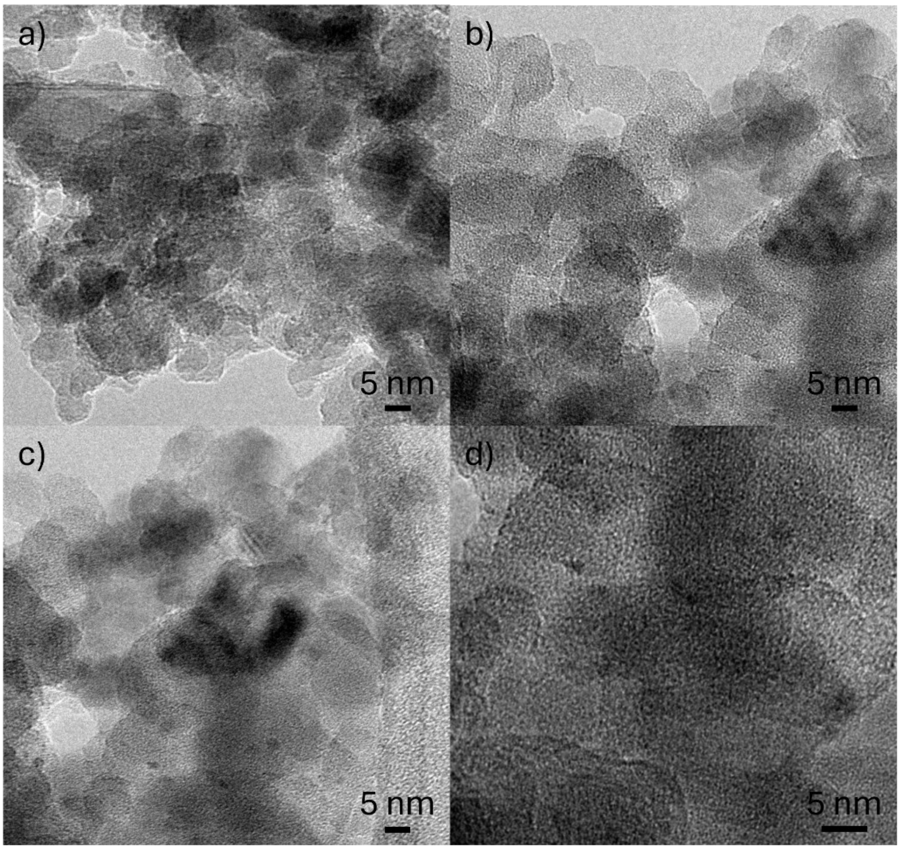

Figure 3.2 Representative HR-TEM micrographs of RuAl at 250kx magnification.

RuAl was investigated by HR-TEM (Figure 3.2) to obtain morphological information on the supported Ru oxy-hydroxy nanoparticles, as well as to determine their size distribution. It was possible to detect isolated Ru oxy-hydroxy nanoparticles of few nanometers, as well as much larger dark spots. The small nanoparticles, averaging around 1 nm in size, point out that the synthesis procedure yielded a highly dispersed Ru oxy-hydroxy phase despite the high Ru loading. The large dark spots instead can be attributed to agglomerates of smaller Ru-containing entities with a high degree of hydration, forming likely as a consequence of the change in the surface charge of the first deposited particles, which in turn behave as secondary nucleation points.[1] These agglomerates appear spatially localized on specific regions of the Al_2O_3 surface, while the smallest nanoparticles are more homogeneously distributed across the support. Due to the inherent poor contrast between fully oxidized Ru species and the alumina support, arising from their similar electron density, a statistically reliable particle size distribution could not be extracted.

In contrast, RuCw (Figure 3.3) displays a more homogeneous morphology, characterized by a narrow population of very small nanoparticles with an average size close to 1 nm. Hydrated $RuO_x(OH)_y$ agglomerates are still detected but are significantly less abundant than in RuAl. RuCch (Figure 3.4) presents an intermediate situation between RuAl and RuCw. Very small nanoparticles are observed, with a broader size distribution than in RuCw, but still smaller on average than those supported on alumina. At the same time, the occurrence and size of hydrated $RuO_x(OH)_y$ agglomerates more closely resemble those observed for RuAl, albeit to a lower extent. The lower density of the carbon support enhances the contrast between Ru species and the support; however, the lack of sharp particle contours prevents a reliable determination of the particle size distribution.

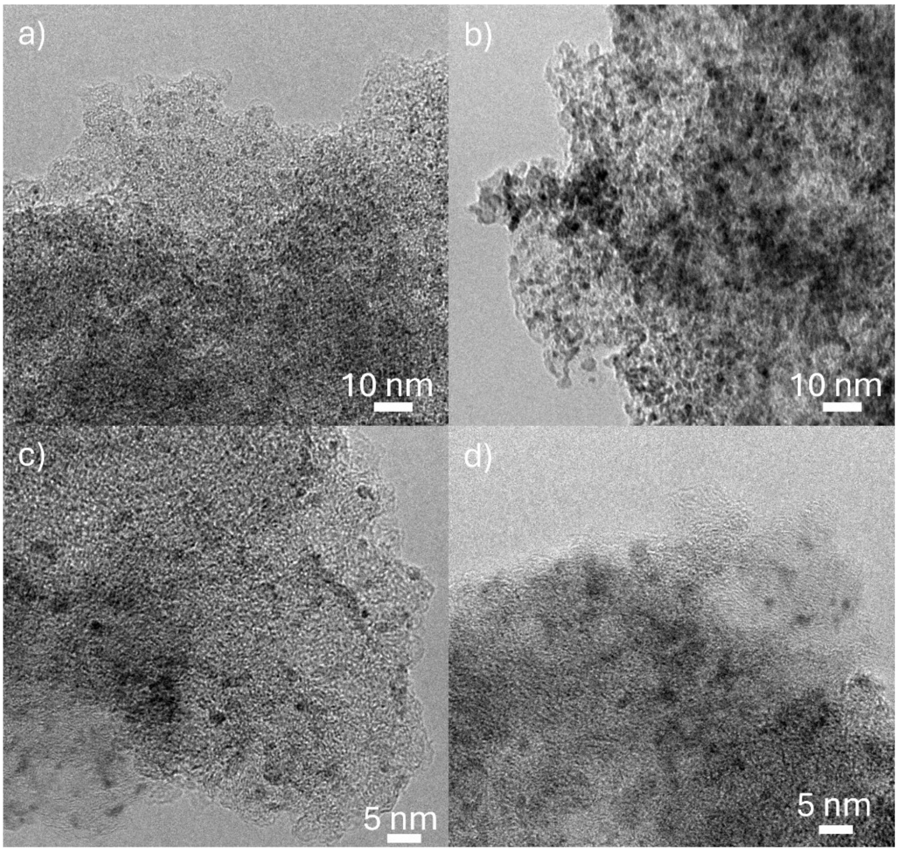

Figure 3.3 Representative HR-TEM micrographs of RuCw at (a,b) 200kx and (c,d) 300kx magnification.

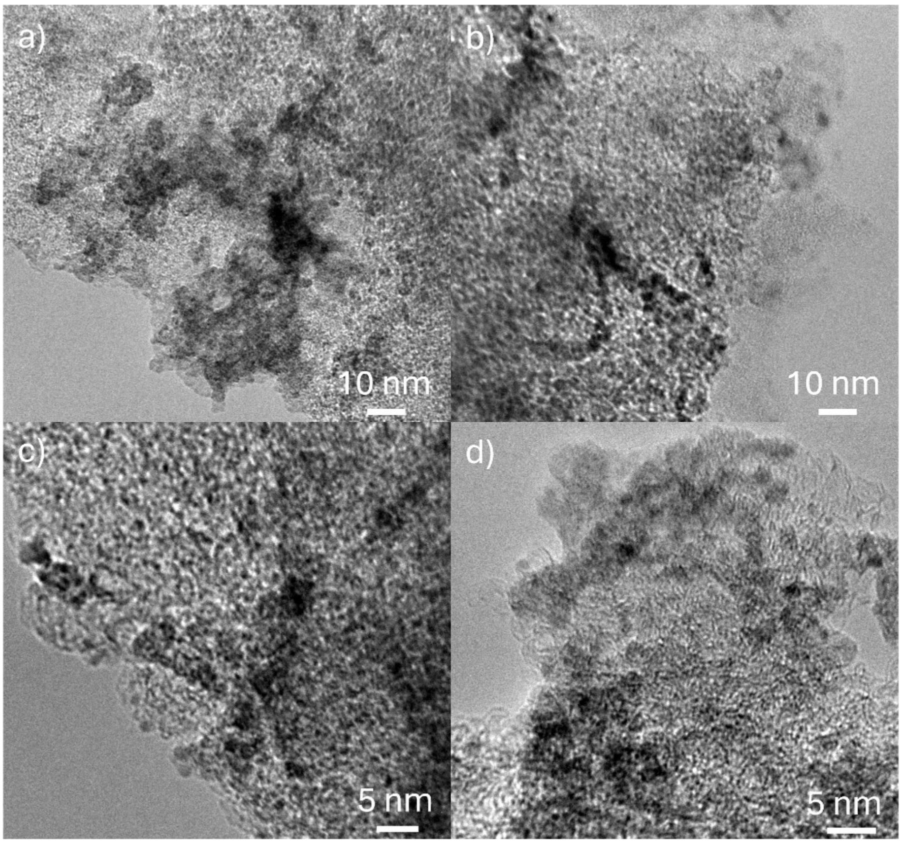

Figure 3.4 Representative HR-TEM micrographs of RuCch at (a,b) 200kx, (c) 400kx and (d) 500kx magnification.

Overall, these observations indicate that deposition–precipitation leads to a highly dispersed Ru-containing phase on all supports, simultaneously promoting the formation of hydrated agglomerates whose abundance and morphology depend strongly on the nature and surface chemistry of the support. In particular, the relative amount of agglomerated Ru oxy-hydroxy species appears to follow a qualitative trend, being lowest on the physically activated carbon (RuCw), intermediate on the chemically activated carbon (RuCch), and highest on alumina (RuAl). This trend suggests a correlation between the density and reactivity of surface oxygen-containing functional groups on the support and the propensity of Ru hydroxide species to nucleate and grow into larger hydrated agglomerates during deposition–precipitation. While TEM alone does not provide information on the oxidation state of the Ru species, it clearly highlights support-dependent differences in dispersion and aggregation that are expected to influence the subsequent chemical evolution of the Ru phase.

3.3 Structural properties of the unsupported and alumina-supported Ru oxy-hydroxy phase

While the morphological analyses discussed in Sections 3.1 were systematically extended to all pristine catalysts, a detailed investigation of the bulk and local structure of the Ru oxy-hydroxide phase by X-ray diffraction (XRD), pair distribution function (PDF) analysis and Ru K-edge X-ray absorption spectroscopy (XAS) was carried out only for selected representative systems. Specifically, the Ru_{uns} and RuAl were chosen as reference cases for in-depth structural analysis. These two systems represent limiting scenarios in terms of metal–support interaction and structural organization of the Ru phase and therefore provide a robust framework for identifying the fundamental structural motifs of the Ru oxy-hydroxide phase obtained by deposition–precipitation. Although activated carbon supports are, in principle, highly suitable for total scattering and XAS measurements due to their weak and featureless scattering background, the limited availability of synchrotron beamtime required a focused experimental strategy. As a result, priority was given to systems expected to exhibit the largest degree of structural differentiation in the oxidized state. The insights gained from Ru_{uns} and RuAl are subsequently used as structural benchmarks for interpreting support-dependent trends observed for all catalysts using complementary techniques.

The Δ-XRD patterns (Figure 3.5a) indicate that: i) Ru_{uns} is completely amorphous; ii) at least a fraction of the supported Ru-phase in RuAl is present as crystalline RuO_2 nanoparticles with rutile structure (with an average particle size ~5 nm estimated through the Scherrer equation[2] applied to the 110 and 211 peaks, at 2.0 and 3.7 $Å^{-1}$), which can be associated with the larger dark spots in the HR-TEM images; iii) the crystalline RuO_2 phase sits atop an amorphous background, suggesting that the distribution of particle sizes comprises a mode (~5 nm) and a broad tail of much smaller amorphous nanoparticles.

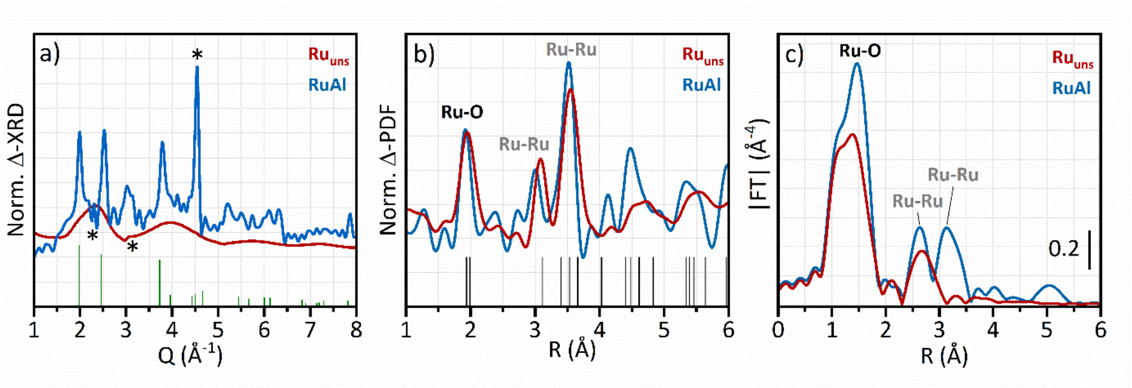

Figure 3.5 Structural results for Ru_{uns} (red) and RuAl (blue) pristine samples measured in inert flow at 25°C. (a) Diffraction patterns after subtraction of the cell contribution and, for RuAl, of the pattern of alumina collected in the same experimental conditions, normalized to the amount of Ru by multiplying RuAl pattern by 15.2=76/5. The main reflections of rutile RuO_2 are also reported (green lines). The stars refer to the main artefacts induced by the non-perfect subtraction of the alumina and glassy carbon signals for RuAl. (b) Pair distribution functions after subtraction of the cell contribution and, for RuAl, of the pattern of alumina collected in the same experimental conditions, normalized to the amount of Ru. The main Ru-O (black) and Ru-Ru (grey) contributions of the rutile RuO_2 reference are also reported. (c) Not phase-corrected |FT| of the k^3-weighted Ru K-edge EXAFS signals.

The Δ-PDFs (Figure 3.5b) reveal that the short-range structure (up to the third-nearest neighbor) is the same for both samples and corresponds to that of rutile RuO_2.[3–5] Namely, Ru is surrounded by six neighboring O atoms, with Ru-O distances at 1.94–1.98 Å in a 2:4 multiplicity ratio (first peak in the Δ-PDF patterns). These $[RuO_6]$ elongated octahedra share their edges to form chains along the c axis, and their vertices to form a three-dimensional structure, where each $[RuO_6]$ octahedra chain is linked to other four chains. Consequently, the Δ-PDF shows two Ru-Ru peaks: around 3.1 Å (i.e. $[RuO_6]$ octahedra sharing the edges, multiplicity 2) and around 3.5 Å (i.e. $[RuO_6]$ octahedra sharing the vertices, multiplicity 8). Ru_{uns} is more disordered than the Ru-phase in RuAl, as evidenced by: i) the broader peaks (e.g. full-width-at-half-maximum, FWHM, of the Ru-Ru peak at ≈ 3.5 Å is 0.211 ± 0.006Å for RuAl and 0.287 ± 0.002 Å for Ru_{uns}); and ii) the much shorter coherence length (i.e. the maximum distance within which the positions of the atoms are significantly correlated). The Δ-PDF signal vanishes before 10 Å for Ru_{uns}, while for RuAl it does not decrease significantly even at 35 Å (Figure A1). Moreover, the peaks of Ru_{uns} are systematically shifted to longer distances, suggesting a slightly expanded framework compared to that of the Ru-phase in RuAl.

Complementary information on the local structure of the two pristine catalysts is obtained from the Ru K-edge EXAFS radial distribution functions (Figure 3.5c and Figure A2) and their fit results (Figure 3.6). Fit results on the first shell Ru-O (Table 3.1) indicate six first-shell oxygen neighbors in both cases, but at a slightly shorter distance for Ru_{uns} and with a higher Debye-Waller factor (0.011 vs. 0.006 $Å^{-2}$). In the |FT| of the EXAFS signal, two peaks associated with Ru neighbors are observed for RuAl (around 2.6 and 3.2 Å, not phase-corrected), corresponding to the Ru-Ru distance of two $[RuO_6]$ octahedra sharing an edge or a vertex, respectively. The second Ru-Ru peak has been found to be sensitive to the hydration state and disappears for $RuO_2{*}nH_2O$ samples with $n>2$.[6] In RuAl, these two contributions exhibit similar intensity, despite their different multiplicity. Similar spectra were reported for $RuO_2{*}nH_2O$ with $n{\sim}0.29$.[6] The lower number of Ru neighbors estimated by the fit (Table 3.1) with respect to bulk RuO_2 could be due to the presence of a fraction of small RuO_2 particles, as evidenced by HR-TEM (Figure 3.2). In fact, the Debye-Waller factors associated with the Ru-Ru scattering paths (0.004 $Å^{-2}$) do not suggest a large structural disorder.

In contrast, only the shorter Ru-Ru contribution is present for Ru_{uns} in the EXAFS |FT|. The fact that the longer Ru-Ru peak is, instead, observed in the Δ-PDF of Ru_{uns} can be explained by the higher sensitivity of EXAFS to local disorder, defects, and multiple scattering effects beyond the second-nearest neighbours.[7–10] In EXAFS, contributions from several scattering atoms at similar distances may interfere destructively due to their complex phase components, cancelling each other out and reducing the visibility of certain peaks. In contrast, PDF analysis provides local structural information through a Fourier transform of the total scattering pattern, which includes the summed contributions from all atom pairs within the probed volume. This makes PDF more robust in detecting atomic structural correlations, even in systems with significant disorder or overlapping atomic distances.[5,7,11] The fit of the Ru_{uns} EXAFS spectrum resulted in an overestimated number of Ru neighbors at ~3.1 Å with respect to that in crystalline RuO_2 and with a large associated error, which is likely the consequence of the presence of additional Ru neighbors at longer distances, as observed in the Δ-PDF, whose contribution to the EXAFS was not possible to simulate.

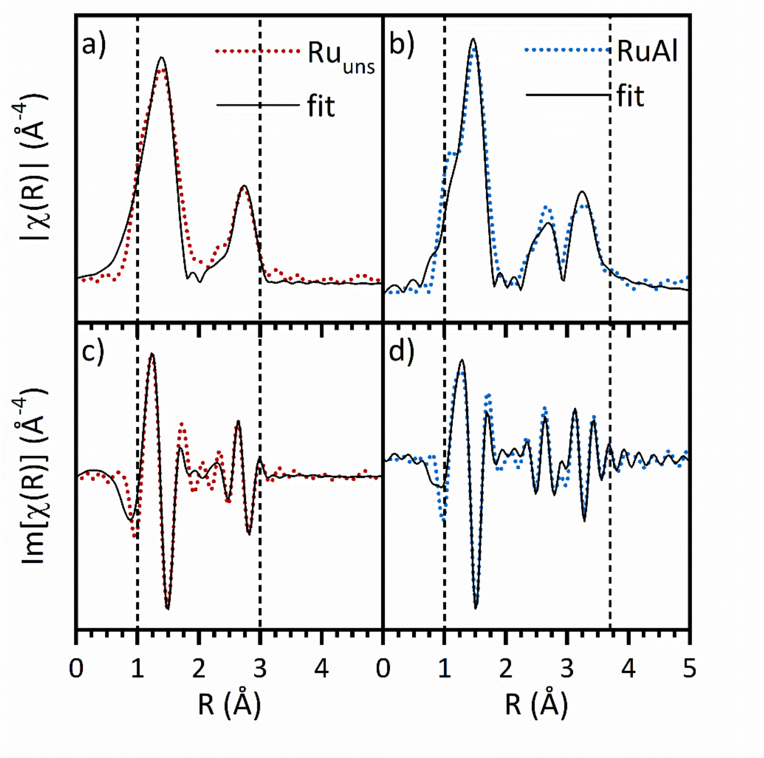

Figure 3.6 |FT| (a and b) and Im(FT) (c and d) of the k^3-weighted EXAFS functions for pristine Ru_{uns} (a and c) and RuAl (b and d) and their fit. The dotted vertical lines indicate the windows considered for the fitting procedure.

Table 3.1 Results of the EXAFS data analysis for pristine Ru_{uns} and RuAl.

	Scattering species	**N_C (atoms)**	**R (Å)**	**σ^2 ($Å^{-2}$)**	**X^2_v**	**R factor (%)**
Ru_{uns}	O_1	1.9 ± 0.4	1.904 ± 0.015	0.011 ± 0.002	17	4.9
	O_2	3.8 ± 0.8	1.954 ± 0.015	0.011 ± 0.002		
	Ru_1	2.8 ± 2.0	3.092 ± 0.018	0.011 ± 0.004		
RuAl	O_1	1.9 ± 0.3	1.932 ± 0.010	0.0062 ± 0.0010	62	4.4
	O_2	3.8 ± 0.6	1.984 ± 0.010	0.0064 ± 0.0010		
	Ru_1	1.1 ± 0.5	3.091 ± 0.010	0.004 ± 0.002		
	Ru_2	2.1 ± 1.0	3.553 ± 0.010	0.004 ± 0.002		

Overall, the structural data shown in Table 3.1 demonstrate that, despite the identical synthesis conditions, the resulting Ru-oxide/hydroxide phase is different between the two samples. Ru_{uns} is amorphous, more hydrated, and its local structure is characterized by a larger contribution from edge-sharing [RuO_6] octahedra. The alumina-supported RuAl, instead, consists of Ru-oxide/hydroxide particles with a broad size distribution. Large (around 5 nm) RuO_2 nanoparticles with an ordered rutile structure dominate the Δ-XRD, Δ-PDF and EXAFS signals. However, the structural data can be fully explained only by considering also the presence of very small nanoparticles (around 1 nm), which are indeed observed by HR-TEM as discussed in Chapter 3.

3.4 Local oxygen environment of Ru oxy-hydroxy phase as a function of the support

The structural analysis discussed in Section 3.2 provides detailed insight into the bulk and medium-range organization of the Ru oxy-hydroxide phase for selected reference systems. However, such techniques are inherently limited in their ability to capture subtle variations in surface chemistry and local oxygen coordination, particularly when extending the comparison across different supports. To overcome these limitations and to enable a systematic comparison of all pristine catalysts investigated in this work, the analysis is here extended to a surface- and local-environment-sensitive spectroscopic probe. To this end, the local oxygen coordination environment of Ru species in the pristine catalysts was investigated by O K-edge NEXAFS spectroscopy (Figure 3.7a-d and Figure A3). This technique probes transitions from O(1s) core levels to unoccupied hybridized O(2p) states. Those transitions involving O(2p) hybridized with Ru(4d) orbitals are sensitive to the chemical environment and coordination geometry of oxygen species associated with Ru, such as terminal oxygen (μ_1(O)), bridging oxygen (μ_2(O)) and peroxo-like moieties.[12,13] Marked differences in the O K-edge spectral profiles are observed depending on the nature of the support, indicating that the Ru oxy-hydroxide phase generated by deposition–precipitation does not share a unique local structure across different supports.

The O K-edge XAS spectra are dominated by a broad, absorption peak centered around 540 eV (Figure A3), which is attributed to transitions involving antibonding O(2p) states hybridized with metal (3s, 3p, 3sp) states and, in the case of supported catalysts, is dominated by the spectroscopic fingerprints of the supports.[14] For all samples, three pre-edge peaks are observed in the 526 – 532.5 eV region (labelled A, B, X in Figure 3.7d) and are distinctive of the oxygen species interacting with the oxy-hydroxy Ru phase. Peaks A and B, which are not observed in the spectrum of bare Al_2O_3 and active carbon supports measured in the same conditions,[14] are ascribed to electronic transitions from O(1s) to hybridized O(2p)-Ru(4dt2$_g$) and O(2p)-Ru(4de$_g$) orbitals, respectively. [14] Fit results are reported in Table 3. *2*.

In the O K-edge XAS spectrum of Ru$_{uns}$, peaks A and B are located at 529.1 eV and 532.0 eV, i.e. the crystal field splitting between Ru(4de$_g$) and Ru(4dt2$_g$) orbitals is Δ=2.9 eV, in agreement with that reported by Occhialini et al. for bulk RuO_2.[15] The relative intensity of these two peaks is about 1.1. According to the DFT calculation of Deka et al.[12] the position and the relative intensity of peak A is highly sensitive to the local coordination and protonation state of the oxygen species, allowing to distinguish μ_1(O), μ_2(O), or μ_3(O) oxygen species (i.e. oxygen atoms bound to 1, 2, or 3 Ru atoms, respectively) and $\mu_{1,2}$(OH) species (i.e. protonated linear (μ_1) and bridged (μ_2) oxygen species). In general, a progressive shift of peak A toward higher photon energies is accompanied by a marked decrease in intensity when moving from low- to high-coordination oxygen environments. Following this assignment, the position of peak A at 529.1 eV is compatible with a majority of μ_1(O) species.

The O K-edge spectrum of RuAl is very similar to that of Ru$_{uns}$, even though the pre-edge peaks are much less intense relative to the broad feature at 540 eV, which is a consequence of the low Ru loading in RuAl. Peaks A and B are positioned at 529.4 and 531.9 eV (crystal field splitting Δ=2.5 eV), with a A/B relative intensity of approximately 0.84. While the energy separation between these features is comparable to that of stoichiometric RuO_2,[15] their relative intensity (0.84) deviates significantly from the ratio obtained for crystalline rutile RuO_2 (1.18)[12] , indicating a structurally disordered Ru oxide phase enriched in low-coordination oxygen species. Importantly, the energy position and relative intensity of the Ru(4dt$_{2g}$) related feature indicate a significant contribution from terminal μ_1(O) species, i.e. oxygen atoms singly coordinated to Ru centers.[12] These species are fingerprints of RuO_2-like crystalline local environments and require a sufficiently extended Ru–O network to be stabilized and have been previously observed also in unsupported Ru oxy-hydroxide system.[12,13]

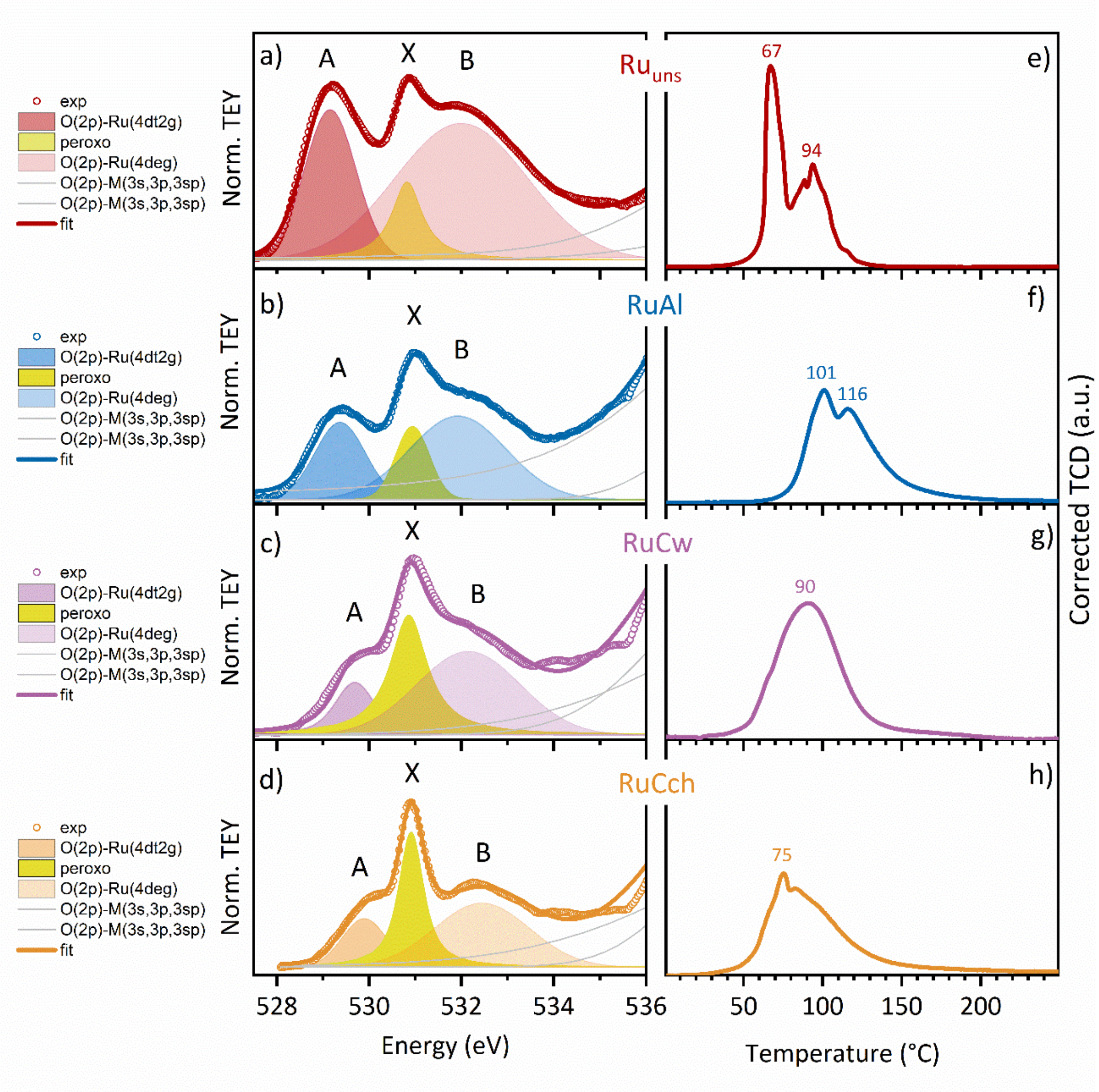

Figure 3.7 Normalized O K-edge NEXAFS spectra of (a) Ru$_{uns}$, (b) RuAl, (c) RuCw and (d) RuCCh in the pre-edge region, together with best-fit components, highlighting support-dependent differences in the local oxygen coordination of the Ru phase. Baseline corrected H_2-TPR profiles of (e) Ru$_{uns}$, (f) RuAl, (g) RuCw and (h) RuCch, showing the corresponding reduction behavior and the position of the main reduction maxima.

The assignment of the intermediate peak X around 530.9 eV,[14] observed in the O K-edge spectra of all samples, is more complicated. Even though its position coincides with that of the O(1s)→O(π*) transition in molecular O_2, its stability in He flow at 25°C and the observation that it declines upon increasing the temperature (*vide infra*) suggest it is more likely associated with intrinsic O-containing species in the samples. A peak in this position is often linked to the presence of surface O-O species or O dangling bonds caused by radiation damage.[16,17] In the context of the oxygen evolution reaction using Ru-oxides/hydroxides anodes, it has been proposed that peroxo O-O species can be formed by interaction of μ_1(O) with H_2O.[13,18–20]

Table 3. 2 Main results of the fit of the O K-edge NEXAFS data for pristine Ru_{uns}, RuAl, RuCw and RuCch.

	Peak A		**Peak X**		**Peak B**	
	Center (eV)	**Area Int**	**Center (eV)**	**Area Int**	**Center (eV)**	**Area Int**
Ru_{uns}	529.154±0.006	1.12±0.02	530.818±0.006	0.51±0.05	531.99±0.03	2.59±0.09
RuAl	529.37±0.03	0.32±0.05	530.942±0.012	0.2±0.2	531.9±0.3	0.6±0.2
RuCw	529.70±0.03	0.22±0.07	530.863±0.011	0.5±0.2	532.13±0.11	0.7±0.2
RuCch	529.89±0.04	0.18±0.07	530.912±0.009	0.39±0.08	532.44±0.09	0.54±0.13

The assignment of the intermediate peak X around 530.9 eV,[14] observed in the O K-edge spectra of all samples, is more complicated. Even though its position coincides with that of the O(1s)→O(π*) transition in molecular O_2, its stability in He flow at 25°C and the observation that it declines upon increasing the temperature (*vide infra*) suggest it is more likely associated with intrinsic O-containing species in the samples. A peak in this position is often linked to the presence of surface O-O species or O dangling bonds caused by radiation damage.[16,17] In the context of the oxygen evolution reaction using Ru-oxides/hydroxides anodes, it has been proposed that peroxo O-O species can be formed by interaction of μ_1(O) with H_2O.[13,18–20]

The O K-edge NEXAFS spectra of both carbon-supported catalysts (Figure 3.7c,d and Figure A3c,d) differ markedly from that of Ru_{uns} and RuAl. In both cases, the Ru($4dt_{2g}$) related feature (peak A) is shifted toward higher photon energy. This position is compatible with contributions from bridging μ_2(O) species and from protonated μ_1(OH) groups,[12] while it does not support the presence of terminal μ_1(O) species. The absence of μ_1(O) signatures indicates that RuO_2-like local environments are not stabilized on carbon supports, and that the Ru oxy-hydroxy phase remains predominantly amorphous and hydroxylated. In addition, both carbon-supported catalysts exhibit spectral features (peak X) attributable to peroxo-like Ru–O–O species, indicating that such moieties are stabilized also in the absence of terminal μ_1(O) groups. The coexistence of hydroxylated and peroxo species suggests that, on carbon supports, the Ru phase remains highly hydrated and structurally disordered at the surface.

This behavior can be rationalized by the limited ability of carbon supports to promote condensation reactions between Ru–OH species and the support surface. In the absence of oxide sites capable of forming Ru–O–support linkages, surface hydroxyl groups remain protonated and stabilized by hydration and hydrogen bonding, preventing the formation of extended RuO_2-like networks required for μ_1(O) stabilization. In contrast, on alumina, condensation of Ru–OH groups leads to Ru–O–Al anchoring, which promotes local structural ordering and enables the stabilization of RuO_2-like domains featuring terminal μ_1(O) species.

3.5 Reducibility of Ru oxy-hydroxy phase as a function of the support

Figure 3.7 (e-h) shows the H_2-TPR profiles of the four samples collected from –70°C and normalized to the Ru amount. For the carbon-supported catalysts, the thermograms were baseline-corrected as described in Chapter 2 to remove contributions associated with the reduction of the support (Figure 2.3). Clear differences in reduction onset temperature, profile shape and peak resolution are observed, highlighting the strong influence of the support on the reducibility of the Ru-based phase formed by deposition–precipitation. The main quantitative parameters extracted from the H_2-TPR profiles, including the reduction onset temperature (T_{start}) and the temperature of the maximum reduction rates (T_{max}), are summarized in Table 3.3.

The thermogram of Ru_{uns} spans over the 40 – 130 °C temperature range, in which a sharp and intense peak at 67 °C is followed by a second broader peak around 94 °C (with a shoulder at 88 °C). The thermogram of RuAl spans the 70 – 200 °C range and shows two main peaks around 101 °C (shoulder at 93°C) and 116 °C (with a long asymmetrical tail at high temperatures). Even though less reducible than Ru_{uns}, RuAl is still highly reducible compared to other alumina-supported Ru-based catalysts of similar Ru loading reported in the literature.[21–25] The higher reducibility of Ru_{uns} with respect to RuAl can be rationalized considering a more defective and disordered structure, enabling H_2 activation already at ambient temperature thus shifting the whole reduction to lower temperatures. The lower reducibility of RuAl is instead associated with higher particle stability due to strong metal-support interaction. Two main H_2 consumption events are observed for both samples that can be related to: i) two families of nanoparticles differing in size; ii) two types of Ru species of different oxidation state, or iii) the occurrence of a two-step consecutive reduction process.[21–25] As it will be clarified extensively in Chapter 4, *in situ* experiments support the interpretation of the two-step reduction process.

The reduction onset temperature of RuAl is higher than that of both carbon-supported catalysts, consistent with stronger metal–support interactions and with the larger average size of Ru-containing entities observed by HR-TEM. For both RuCw and RuCch, complete reduction is achieved above approximately 150 °C. The RuAl thermogram (Figure 3.7f) is characterized by relatively sharp and well-resolved features, indicative of a more regular reduction behavior compared to RuCw and RuCch, which instead exhibit broader and less resolved profiles.

RuCw displays a single dominant reduction feature centered at approximately 90 °C, with no clearly resolved secondary peaks (Figure 3.7e). Given the NEXAFS evidence for a predominantly hydroxylated Ru environment and the absence of μ_1(O) signatures, this profile is best interpreted as a regime where the transformations are strongly overlapped, and the reduction intermediate does not accumulate. As a result, reduction proceeds through a series of activation energies, too close in value to one another to be kinetically resolved, giving rise to a single broad reduction feature.

RuCch exhibits a more complex H_2-TPR profile compared to RuCw, characterized by a sharp low-temperature reduction feature at approximately 75 °C followed by a broader and asymmetric contribution extending to higher temperatures (Figure 3.7f). This behavior indicates a partial kinetic separation of reduction events, intermediate between the fully overlapped regime observed for RuCw and the well-resolved two-step reduction characteristic of RuAl. The more heterogeneous oxygen coordination inferred from NEXAFS, and the higher degree of aggregation suggested by microscopy, plausibly broaden the reduction barrier distribution and allow partial kinetic stabilization of the reduction intermediate on a subset of sites, without fully resolving the two intrinsic redox steps. However, the absence of μ_1(O) features in NEXAFS indicates that even in RuCch these domains do not evolve into RuO_2-like ordered structures, explaining why the two intrinsic redox steps result only partially resolved.

In all cases, the total H_2 consumption exceeds the theoretical value expected for the reduction of stoichiometric RuO_2 (H_2(ratio) in Table 3.3). This overconsumption cannot be attributed to experimental artefacts and reflects additional hydrogen-consuming processes occurring during reduction. It can be attributed to several factors: i) presence of a second phase beside RuO_2 in which Ru has an average oxidation state higher than four; ii) presence of surface peroxo groups,[13,18–20] which can react with H_2 to form water; iii) spillover of H atoms on the support triggered by the formed metallic Ru. The O K-edge XAS data discussed above strongly support hypothesis ii), therefore the excess H_2 uptake is attributed to the reduction of non-stoichiometric oxygen species, such as peroxo-like Ru–O–O moieties. Importantly, these contributions affect the overall hydrogen balance but are not expected to give rise to distinct, well-separated reduction peaks.

Table 3.3 Reduction onset temperature (T_{start}), temperature of the main reduction maxima (T_{max}), H_2(ratio), defined as the experimental H_2 consumption determined from H_2-TPR measurements normalized to the theoretical value expected for complete reduction of RuO_2, and apparent Ru dispersion values obtained from pulsed CO chemisorption measurements, calculated assuming a CO/Ru adsorption stoichiometry of 1. All data refers to catalysts from the first aliquot, dried overnight at 90 °C and stored under ambient conditions prior to characterization.

Sample	**H_2-TPR**			**D (%)**
	T_{start} (°C)	**T_{max} (°C)**	**H_2(ratio)**	
Ru_{uns}	45	67 | 94	1.10	0
RuAl	68	101 | 116	1.16	22
RuCw	46	90	1.35	84
RuCch	49	75 | 85	1.10	66

A qualitative correlation between the excess hydrogen consumption measured by H_2-TPR and the relative intensity of peroxo-related features observed by O K-edge NEXAFS is shown in Figure 3.8. When plotting the normalized intensity of the peroxo-related band against the H_2 consumption ratio, a linear trend is observed for three samples, indicating that an increasing peroxo contribution is associated with increasing hydrogen overconsumption. This trend includes RuAl and RuCw and Ru_{uns}, while RuCch deviates from this correlation. The deviation of RuCch is likely due to the substantial contribution of oxygen-containing functional groups associated with the chemically activated carbon support to the O K-edge signal, which complicates a quantitative comparison.

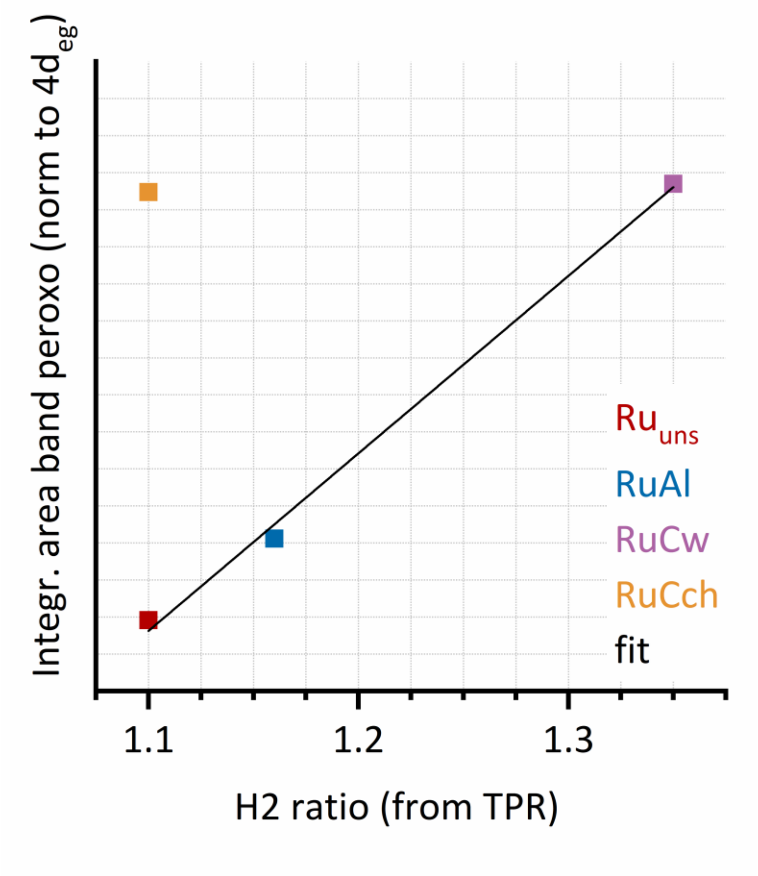

Figure 3.8 Fitted integrated area of peak X (peroxo moieties) as function of the H_2 consumption ratio. Area values have been normalized *to the area of 4d$_{eg}$ resonance for quantitative comparison*.

3.6 Conclusions

This chapter provided a comparative description of the oxidized Ru oxy-hydroxide phase generated by deposition–precipitation (and related precipitation routes) on industrially relevant supports, with the aim of identifying how morphology and local oxygen coordination govern the apparent reducibility observed by H_2-TPR.

Electron microscopy showed that all synthesis routes considered lead to highly dispersed Ru-containing species, despite the relatively high metal loading. On alumina, very small nanoparticles coexist with hydrated agglomerates localized on specific regions of the support, whereas on activated carbons the Ru phase is generally more uniformly dispersed and agglomerates are less abundant. Although the intrinsic contrast limitations prevent a robust particle size distribution for some supported samples, the qualitative trend is clear: the extent of aggregation of the oxidized Ru phase depends strongly on the support surface chemistry, being highest on alumina, intermediate on chemically activated carbon, and lowest on physically activated carbon.

Bulk- and local-structure probes applied to selected reference systems (Ru_{uns} and RuAl) indicate that the oxidized Ru phase cannot be described as a single, well-defined RuO_2 phase. Instead, it spans a continuum from highly disordered and short-coherence-length RuO_2-like motifs (dominant in the unsupported sample) to more ordered rutile-like RuO_2 domains coexisting with a fraction of highly dispersed and hydrated species (in the alumina-supported catalyst). These results establish that identical synthesis conditions can yield markedly different degrees of structural ordering depending on whether Ru species evolve in the absence of a support or are anchored to an oxide surface.

Surface-sensitive TEY-NEXAFS O K-edge revealed that the local oxygen environment of the oxidized Ru phase is strongly support-dependent. Unsupported and alumina-supported samples display clear signatures consistent with the presence of terminal low-coordination oxygen species (μ_1(O)), indicative of partially RuO_2-like local ordering. In contrast, carbon-supported catalysts lack μ_1(O) fingerprints and are dominated by hydroxylated oxygen environments, consistent with a more amorphous and highly hydrated Ru oxy-hydroxide phase. In all systems, an additional pre-edge contribution is observed and attributed to peroxo-like Ru–O–O species, whose stabilization is favored by hydration and surface disorder.

These differences in local oxygen coordination directly determine the reduction behavior observed by H_2-TPR. Catalysts exhibiting a higher degree of RuO_2-like domains display more resolved reduction features, while highly hydrated and structurally disordered systems show broader and more overlapped reduction events. In all cases, the total hydrogen consumption exceeds the stoichiometric value expected for RuO_2 reduction. The combined NEXAFS and TPR evidence supports the interpretation that this “overconsumption” primarily originates from the reduction of non-stoichiometric oxygen species, including peroxo-like Ru–O–O moieties, rather than from experimental artefacts.

Overall, the results demonstrate that the Ru oxy-hydroxide phase obtained by deposition–precipitation is not a universal precursor, but a support-dependent family of hydrated and partially ordered structures. This support-controlled local oxygen coordination governs both the shape of H_2-TPR profiles and the hydrogen balance during reduction. The structural identity and evolution of the reduced and intermediate states implied by the multi-feature TPR thermograms will be addressed in the following chapter through bulk-sensitive *in situ* investigations.

References

(1) Fernández, C.; Sassoye, C.; Flores, N.; Escalona, N.; Gaigneaux, E. M.; Sanchez, C.; Ruiz, P. Insights in the Mechanism of Deposition and Growth of RuO2 Colloidal Nanoparticles over Alumina. Implications on the Activity for Ammonia Synthesis. *Appl. Catal. A Gen.* **2015**, *502*, 48–56. https://doi.org/https://doi.org/10.1016/j.apcata.2015.05.023.

(2) Patterson, A. L. The Scherrer Formula for X-Ray Particle Size Determination. *Physical Review* **1939**, *56* (10), 978–982. https://doi.org/10.1103/PhysRev.56.978.

(3) Over, H. Ruthenium Dioxide, a Fascinating Material for Atomic Scale Surface Chemistry. *Applied Physics A* **2002**, *75* (1), 37–44. https://doi.org/10.1007/s003390101053.

(4) Over, H. Surface Chemistry of Ruthenium Dioxide in Heterogeneous Catalysis and Electrocatalysis: From Fundamental to Applied Research. *Chem. Rev.* **2012**, *112* (6), 3356–3426. https://doi.org/10.1021/CR200247N.

(5) Donakowski, M. D.; Mansour, A. N.; Pala, I. R.; Chervin, C. N.; DeSario, P. A.; Long, J. W.; Rolison, D. R. Trapping a Ru2O3 Corundum-like Structure at Ultrathin, Disordered RuO2 Nanoskins Expressed in 3D. *The Journal of Physical Chemistry C* **2018**, *122* (50), 28895–28900.

(6) McKeown, D. A.; Hagans, P. L.; Carette, L. P. L.; Russell, A. E.; Swider, K. E.; Rolison, D. R. Structure of Hydrous Ruthenium Oxides: Implications for Charge Storage. *J. Phys. Chem. B* **1999**, *103* (23), 4825–4832. https://doi.org/10.1021/jp990096n.

(7) Dimitrov, D. A.; Ankudinov, A. L.; Bishop, A. R.; Conradson, S. D. Pair Distribution Function and X-Ray Absorption Signatures of Rotational and Radial Local Distortions in a Model System with Average Long-Range Order. *Phys. Rev. B* **1998**, *58* (21), 14227–14237. https://doi.org/10.1103/PhysRevB.58.14227.

(8) Frenkel, A.; Stern, E. A.; Voronel, A.; Qian, M.; Newville, M. Solving the Structure of Disordered Mixed Salts. *Phys. Rev. B* **1994**, *49* (17), 11662–11674. https://doi.org/10.1103/PhysRevB.49.11662.

(9) Ankudinov, A. L.; Rehr, J. J. Development of XAFS Theory. *J. Synchrotron Radiat.* **2003**, *10* (5), 366–368. https://doi.org/10.1107/S0909049503009130.

(10) Finzel, J.; Sanroman Gutierrez, K. M.; Hoffman, A. S.; Resasco, J.; Christopher, P.; Bare, S. R. Limits of Detection for EXAFS Characterization of Heterogeneous Single-Atom Catalysts. *ACS Catal.* **2023**, *13* (9), 6462–6473. https://doi.org/10.1021/acscatal.3c01116.

(11) Petkov, V. Pair Distribution Functions Analysis. In *Characterization of Materials*; **2012**; pp 1–14. https://doi.org/https://doi.org/10.1002/0471266965.com159.

(12) Deka, N.; Jones, T. E.; Falling, L. J.; Sandoval-Diaz, L.-E.; Lunkenbein, T.; Velasco-Velez, J.-J.; Chan, T.-S.; Chuang, C.-H.; Knop-Gericke, A.; Mom, R. V. On the Operando Structure of Ruthenium Oxides during the Oxygen Evolution Reaction in Acidic Media. *ACS Catal.* **2023**, *13* (11), 7488–7498. https://doi.org/10.1021/acscatal.3c01607.

(13) Di Liberto, G.; Pacchioni, G.; Shao-Horn, Y.; Giordano, L. Role of Water Solvation on the Key Intermediates Catalyzing Oxygen Evolution on RuO2. *The Journal of Physical Chemistry C* **2023**, *127* (21), 10127–10133. https://doi.org/10.1021/acs.jpcc.3c02733.

(14) Frati, F.; Hunault, M. O. J. Y.; de Groot, F. M. F. Oxygen K-Edge X-Ray Absorption Spectra. *Chem. Rev.* **2020**, *120* (9), 4056–4110. https://doi.org/10.1021/acs.chemrev.9b00439.

(15) Occhialini, C. A.; Bisogni, V.; You, H.; Barbour, A.; Jarrige, I.; Mitchell, J. F.; Comin, R.; Pelliciari, J. Local Electronic Structure of Rutile RuO2. *Phys. Rev. Res.* **2021**, *3* (3), 33214. https://doi.org/10.1103/PhysRevResearch.3.033214.

(16) Ayoola, H. O.; Li, C.-H.; House, S. D.; Bonifacio, C. S.; Kisslinger, K.; Jinschek, J.; Saidi, W. A.; Yang, J. C. Origin and Suppression of Beam Damage-Induced Oxygen-K Edge Artifact from γ-Al2O3 Using Cryo-EELS. *Ultramicroscopy* **2020**, *219*, 113127. https://doi.org/https://doi.org/10.1016/j.ultramic.2020.113127.

(17) Jiang, N.; Spence, J. C. H. On the Dose-Rate Threshold of Beam Damage in TEM. *Ultramicroscopy* **2012**, *113*, 77–82. https://doi.org/https://doi.org/10.1016/j.ultramic.2011.11.016.

(18) Shi, Z.; Li, J.; Wang, Y.; Liu, S.; Zhu, J.; Yang, J.; Wang, X.; Ni, J.; Jiang, Z.; Zhang, L.; Wang, Y.; Liu, C.; Xing, W.; Ge, J. Customized Reaction Route for Ruthenium Oxide towards Stabilized Water Oxidation in High-Performance PEM Electrolyzers. *Nat. Commun.* **2023**, *14* (1), 843. https://doi.org/10.1038/s41467-023-36380-9.

(19) Zhang, J.; Fu, X.; Kwon, S.; Chen, K.; Liu, X.; Yang, J.; Sun, H.; Wang, Y.; Uchiyama, T.; Uchimoto, Y.; Li, S.; Li, Y.; Fan, X.; Chen, G.; Xia, F.; Wu, J.; Li, Y.; Yue, Q.; Qiao, L.; Su, D.; Zhou, H.; Goddard, W. A.; Kang, Y. Tantalum-Stabilized Ruthenium Oxide Electrocatalysts for Industrial Water Electrolysis. *Science (1979).* **2025**, *387* (6729), 48–55. https://doi.org/10.1126/science.ado9938.

(20) Tang, J.; Guan, D.; Xu, H.; Zhao, L.; Arshad, U.; Fang, Z.; Zhu, T.; Kim, M.; Pao, C.-W.; Hu, Z.; Ge, J.; Shao, Z. Undoped Ruthenium Oxide as a Stable Catalyst for the Acidic Oxygen Evolution Reaction. *Nat. Commun.* **2025**, *16* (1), 801. https://doi.org/10.1038/s41467-025-56188-z.

(21) Quintero-Ramos, D.; Checa, M.; Jordá, J. L.; Sabater, M. J. Study on the Hydrogenation of Ethyl Stearate to the Fatty Alcohol 1-Octadecanol over Ru on Tungstated Zirconia. *Catalysts* **2023**, *13* (10). https://doi.org/10.3390/catal13101362.

(22) Balaraju, M.; Rekha, V.; Devi, B. L. A. P.; Prasad, R. B. N.; Prasad, P. S. S.; Lingaiah, N. Surface and Structural Properties of Titania-Supported Ru Catalysts for Hydrogenolysis of Glycerol. *Appl. Catal. A Gen.* **2010**, *384* (1), 107–114. https://doi.org/https://doi.org/10.1016/j.apcata.2010.06.013.

(23) Balint, I.; Miyazaki, A.; Aika, K. Methane Reaction with NO over Alumina-Supported Ru Nanoparticles. *J. Catal.* **2002**, *207* (1), 66–75. https://doi.org/https://doi.org/10.1006/jcat.2001.3489.

(24) Pavan Kumar, V.; Priya, S. S.; Harikrishna, Y.; Kumar, A.; Chary, K. V. R. Catalytic Functionalities of Nano Ruthenium/γ-Al2O3 Catalysts for the Vapour Phase Hydrogenolysis of Glycerol. *J. Nanosci. Nanotechnol.* **2016**, *16* (2), 1952–1960.

(25) García-García, F. R.; Fernández-García, M.; Newton, M. A.; Rodríguez-Ramos, I.; Guerrero-Ruiz, A. Following the Evolution of Ru/Activated Carbon Catalysts during the Decomposition–Reduction of the Ru(NO)(NO3)3 Precursor. *ChemCatChem* **2013**, *5* (8), 2446–2452. https://doi.org/https://doi.org/10.1002/cctc.201300065.

Chapter 4

4 From oxidized Ru oxy-hydroxide to metallic Ru: bulk and surface pathways

4.1 Chapter overview and scope

Building on Chapter 3, where support-dependent differences in the oxidized Ru oxy-hydroxide precursor and its H_2-TPR fingerprints were established, this chapter addresses a central chemical question: how does the DP-derived oxidized Ru phase transform under activation conditions, and which transient states and surface species govern hydrogen uptake and reactivity? While temperature-programmed techniques provide clear phenomenological evidence of complex reduction behavior, they do not directly reveal the structural identity of the species involved nor the role played by the catalyst surface during activation.

To answer this, bulk-sensitive *in situ* synchrotron methods (Ru K-edge XAS, high-energy total scattering/PDF, and XRD) were coupled with surface-sensitive spectroscopies (*in situ* IR, O K-edge NEXAFS and INS). This integrated experimental strategy allows for direct monitoring of the evolution of the Ru phase across multiple length scales, from long- and medium-range structural motifs in the bulk to local coordination environments of oxygen- and hydrogen-containing species at the surface and at the metal–support interface. This multiscale approach effectively connects i) the multi-event features observed in H_2-TPR thermograms, ii) the formation of transient bulk intermediate phases, and iii) the evolution of oxygenated and hydrogen-containing surface species responsible for H_2 activation and transfer. By explicitly correlating kinetic signatures with time-resolved structural and spectroscopic information, the chapter aims to move beyond a purely descriptive interpretation of reducibility toward a mechanistic understanding of Ru activation.

Ru_{uns} and RuAl are used as reference systems to disentangle intrinsic properties of the Ru oxy-hydroxide network from support effects, representing two limiting cases in terms of structural order, hydration and metal–support interaction. The surface study is then focused on RuAl, where the Ru/support interface can be probed directly. This choice enables a detailed investigation of how surface dehydration, oxygen restructuring and hydrogen adsorption cooperate with bulk reduction processes to determine the active state of Ru-based catalysts under hydrogenation conditions.

4.2 Bulk reduction pathway: identification of a transient Ru(III) phase

4.2.1 Two-step reduction fingerprints: kinetic evidence from *in situ* Ru K-edge XAS

In view of the sensitivity of Ru K-edge XAS spectroscopy to the defective local structure of the Ru phases, the reduction behavior of both Ru_{uns} and RuAl was investigated by means of *in situ* XAS spectroscopy. As described in Chapter 2, the H_2-TPR experiment started at 25°C with an isothermal step in H_2/Ar at 25°C, followed by the temperature ramp and by another isothermal step in H_2/Ar at 200°C.

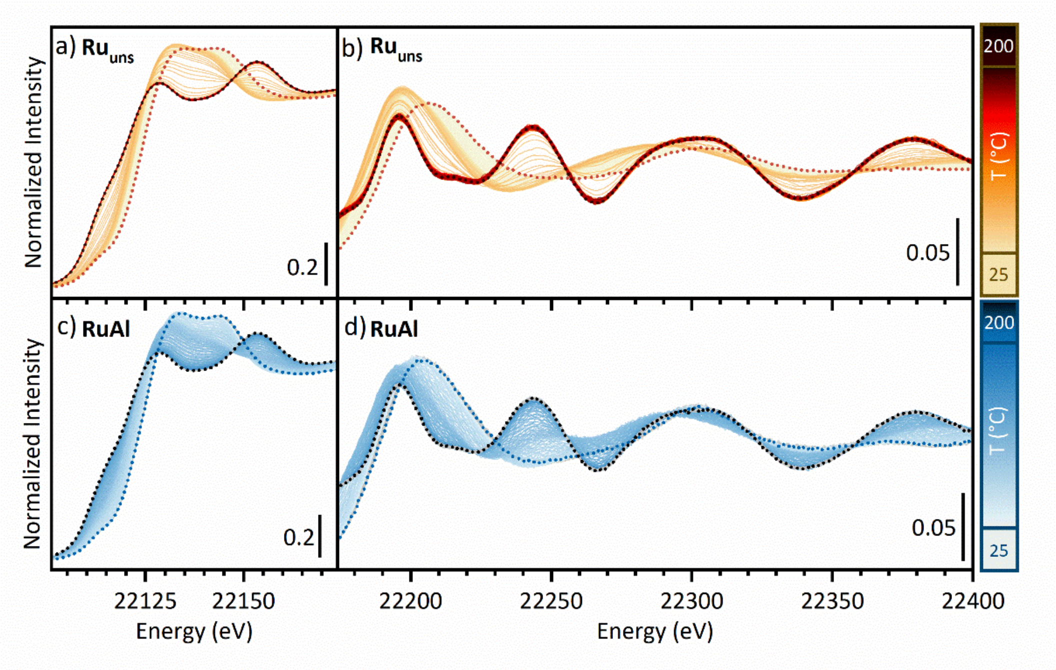

Figure 4.1 Evolution of the normalized Ru K-edge XAS spectra of (a-b) Ru_{uns} and (c-d) RuAl during the H_2-TPR experiment in the (a-c) XANES and (b-d) EXAFS regions. The first and last spectra are reported with dotted lines.

Figure 4.1 shows the evolution of the normalized Ru K-edge XAS spectra for both samples in the XANES (a-c) and EXAFS (b-d) regions. Not only the initial (Figure A2a-c), but also the final spectra (Figure A2d-f) of both catalysts are very similar. The EXAFS spectra at the end of the experiments have been fitted with R-factors ≤ 1% (Figure A4 and Table A1) using scattering paths calculated from Ru hcp metal CIF file with FEFF. While in both cases the Ru-oxide/hydroxide phase has been completely reduced to metallic Ru at the end of the temperature ramp in H_2/Ar, the reduction kinetics are clearly different: Ru_{uns} is substantially reduced already during the isothermal step in H_2 at 25°C, in marked contrast to RuAl whose spectra do not change appreciably in the same conditions.

To better understand the reduction behavior of the two samples, the two experimental datasets of Figure 4.1 were analyzed by means of a PCA/MCR-ALS approach. The outcomes of this analysis are reported in Figure 4.2. For both Ru_{uns} (Figure 4.2a-b) and RuAl (Figure 4.2d-e), the XAS spectra of the initial and final components optimized by MCR coincide with the first and last experimental spectra. This indicates that the initial state and the final state of each sample are each well described by a single, distinct spectral component – one for the oxidized state (Ru-ox) and one for the metallic state (Ru-met). Additionally, a third component (Ru-interm) is required to accurately reconstruct both datasets, capturing a transitional phase between the two stable states.

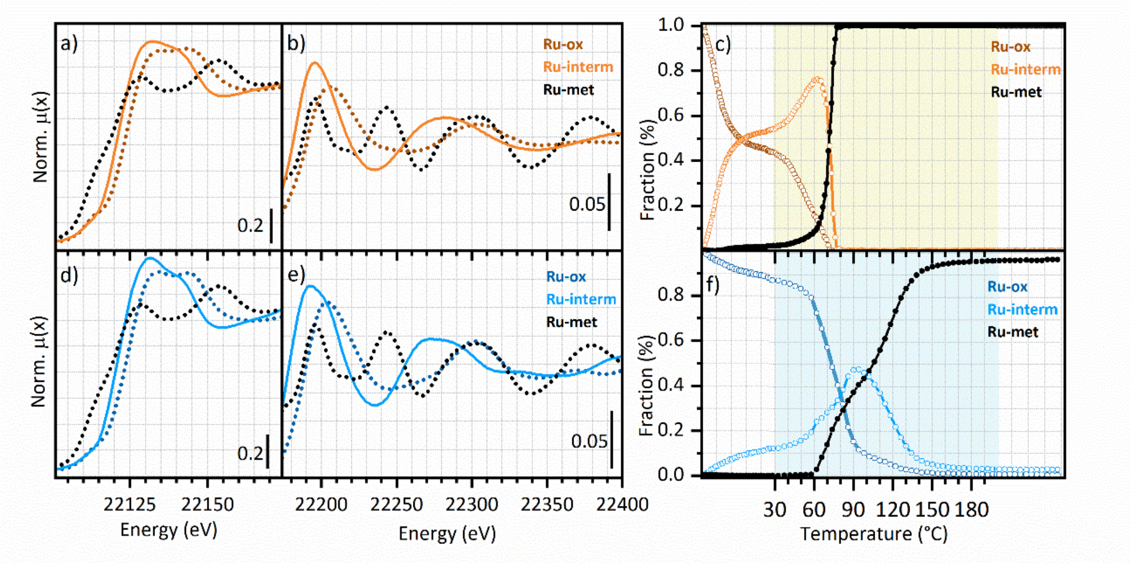

Figure 4.2 Results of the MCR analysis on the Ru K-edge XAS spectra of Figure 4. Optimized components for Ruuns in the (a) XANES and (b) EXAFS regions and (c) evolution of their relative fraction as a function of time and temperature (yellow area). Optimized components for RuAl in the (d) XANES and (e) EXAFS regions and (f) evolution of their relative fractions as a function of time and temperature (blue area).

Starting the discussion from Ru_{uns}, the relative fraction of the initial Ru-ox component rapidly declines already during the isotherm in H_2/Ar at 25°C in favor of the Ru-interm component, which accounts for ~ 50% of the total Ru-phase at the end of the isothermal step (Figure 4.2c). Almost no Ru-met is formed at this stage. The relative fraction of the Ru-interm phase peaks (80% of the total) at the beginning of the temperature ramp, around 60 °C. Then, between 60 and 80°C, the concentration of the Ru-interm component drops to zero, while that of Ru-met quickly goes from less than 10% to 100% completing the reduction around 90°C. Thus, the profiles reported in Figure 4.2c reveal that the H_2-reduction of Ru_{uns} proceeds through two consecutive steps: before reaching 60°C the initial Ru-oxide/hydroxide phase is almost completely converted into an intermediate phase, which in turn is rapidly reduced to Ru metal with a maximum in the conversion rate around 73°C. This is in accord with the two reduction events observed in the H_2-TPR profile. Notably, the temperatures values corresponding to the maximum rate of the two consecutive reactions are very similar to those of the two peaks observed in the H_2-TPR performed in the same conditions (*i.e.* starting from 25°C, Figure A5).

As to the H_2-reduction behavior of RuAl (Figure 4.2f), during the isothermal treatment in H_2/Ar at 25°C only around 10% of the initial Ru-ox component is converted into Ru-interm, while no Ru-met is formed. Only int the range 60-90°C does the Ru-ox component rapidly drop (to about 10% of the total) and Ru-met starts to appear. Ru-interm peaks at 90°C, while Ru-met still accounts for about 40%. From that point on, both Ru-interm and the residual Ru-ox are converted into Ru-met, and the reduction is completed at around 130 °C. Even though less clearly than for Ru_{uns}, also in this case the MCR analysis (Figure 4.2f) suggests that reduction of the supported Ru-oxide/hydroxide phase to Ru metal proceeds through an intermediate phase. The first derivative of the composition profile for Ru-interm as a function of temperature (Figure A6) displays three main peaks: two positive around 60 and 85°C, which correspond to the formation of Ru-interm from Ru-ox, and one negative around 120°C, corresponding to the conversion of Ru-interm to Ru-met. Very similar peaks are observed in the H_2-TPR thermogram collected starting from 25°C (Figure A5).

4.2.2 Structural fingerprints of the intermediate phase: EXAFS evidence for a Ru(III)-containing motif

To clarify the nature of the intermediate phases, the XAS spectra for the Ru-interm components optimized with MCR-ALS were Fourier-Transformed ($\Delta k = 3 - 15$ Å^{-1}) and fitted in R space. The results are shown in Figure 4.3 and Table 4.1, and are very similar for Ru_{uns} and RuAl. The results of the fitting procedure indicate a slight decrease in the number of first shell oxygen neighbors with respect to the pristine state, and an elongation of the average Ru-O bond lengths by about 5%. At longer distance, the fits indicate the presence of a Ru contribution at around 2.5 Å (phase corrected), i.e. much shorter than the Ru-Ru distance in rutile lattice (3.1 Å). A similar contribution was previously observed in the EXAFS data for amorphous and partially hydrated $RuO_2 * nH_2O$ with $n \approx 2$,[1] and in the PDF patterns of RuO_x materials prepared by electroless deposition.[2] It was proposed that this short Ru-Ru contribution fits the metastable corundum-like Ru_2O_3 structure, where neighboring $[RuO_6]$ octahedra share a face instead of edges and vertices.[2]

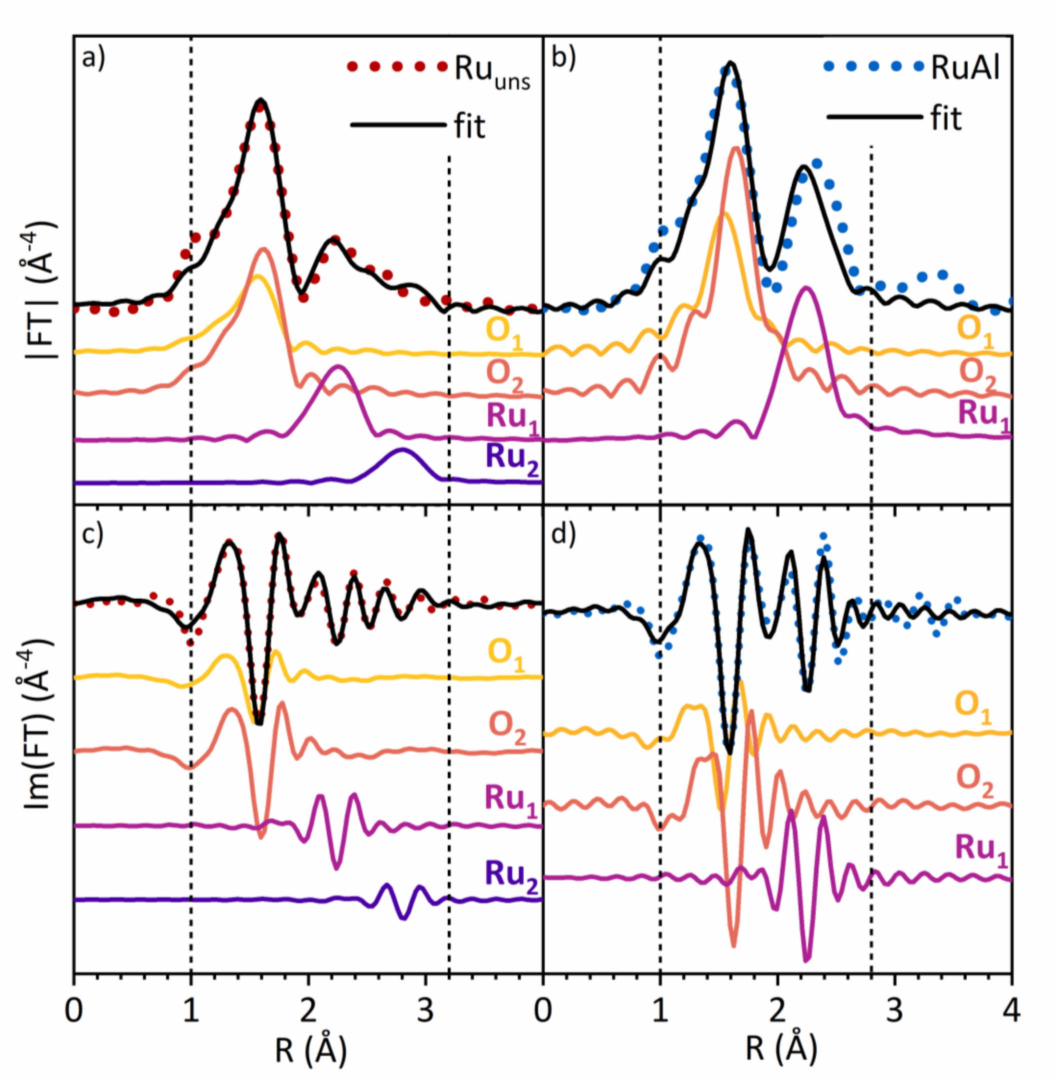

Figure 4.3 (a,b) Phase-uncorrected |FT| and (c,d) Im(FT) of the k^3-weighted optimized spectra (dotted) of the Ru-interm components obtained from the PCA-MCR analysis of the XAS dataset for Ru_{uns} (a,c) and RuAl (b,d), compared to the best fits (full lines). The fitted single scattering paths are also reported (vertically translated). The dotted vertical lines indicate the windows considered for the fitting procedure.

Table 4.1 Results of the fit of the Fourier-Transformed EXAFS spectrum for the Ru-interm component defined by MCR for both Ru_{uns} and RuAl.

	Scattering species	**N_C (ATOMS)**	**R (Å)**	**σ^2 ($Å^{-2}$)**	**χ^2_v**	**R factor (%)**
Ru_{uns}	O_1	1.8 ± 0.3	2.012 ± 0.010	0.0040 ± 0.0010	129	2.0
	O_2	3.6 ± 0.5	2.055 ± 0.010	0.0040 ± 0.0010		
	Ru_1	0.7 ± 0.5	2.539 ± 0.012	0.0040 ± 0.0005		
	Ru_2	0.5 ± 0.2	3.121 ± 0.013	0.0040 ± 0.0005		
RuAl	O_1	1.8 ± 0.3	1.96 ± 0.05	0.001 ± 0.003	7489	3.5
	O_2	3.7 ± 0.6	2.06 ± 0.02	0.001 ± 0.003		
	Ru_1	0.9 ± 0.4	2.549 ± 0.007	0.003 ± 0.002		

4.2.3 Capturing the intermediate in real space: PDF evidence for short Ru-Ru correlations

The same *in situ* H_2-reduction experiments discussed above were repeated using high energy X-rays total scattering. The resulting PDF data provides a complementary perspective to that offered by EXAFS. The discussion will focus here on the case of Ru_{uns}, where the PDF signals originate exclusively from the Ru phase and are not affected by interference from the support. Figure 4.4 for Ru_{uns} shows the evolution of the Δ-PDF patterns, obtained by subtracting the first pattern of the dataset from the subsequent ones, during both the isothermal reduction at 25 °C (a) and the temperature ramp (b).

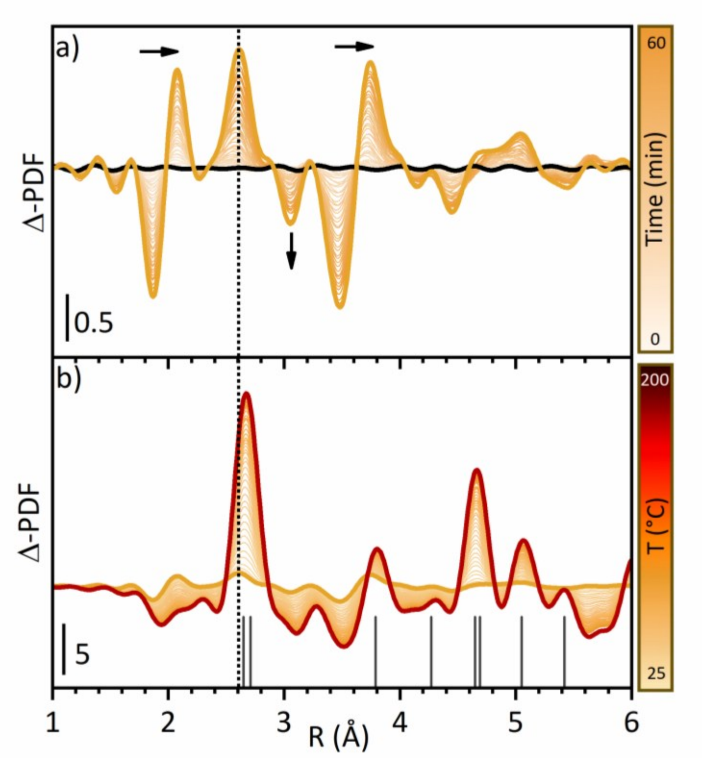

Figure 4.4 Evolution of the Δ-PDF patterns of Ru_{uns}, obtained by subtracting the first pattern of the dataset from the subsequent ones during H_2-TPR experiment: (a) isothermal segment at 25 °C; (b) TPR ramp from 25 °C up to 200 °C. Dark grey vertical lines show Ru-Ru distances in the hcp lattice from CIF file.[3,4]

During the isothermal segment three main features are observed: i) the first Ru-O (~1.9 Å) and the second Ru-Ru (~3.5 Å) peaks shift to higher distances, as evidenced by the derivative-like shape of the differential signal; ii) the intensity of the first Ru-Ru peak (~3.1 Å), characteristic of the RuO_2 rutile motif, decreases; iii) a new peak emerges at ~2.6 Å. These changes indicate an overall expansion of Ru-O bond lengths within the amorphous rutile-like structure and the replacement of the original Ru–Ru distance with a shorter one, consistent with the condensed face and edge-sharing octahedra in the proposed Ru_2O_3 motif. This transformation likely occurs via the formation of oxygen vacancies, which at first induce longer octahedral Ru-O distances rather than the suppression of Ru-O distances. During the temperature ramp, the features associated with this intermediate Ru_2O_3-like phase gradually give way to peaks characteristic of metallic Ru, in agreement with the results obtained from complementary techniques. The peak observed at the end of the isotherm (2.61 Å) is ~3% shorter than the final Ru–Ru distance in metallic Ru (2.68 Å) (Figure 4.4b), and this cannot be explained by thermal expansion alone (which would account for ~0.3%).

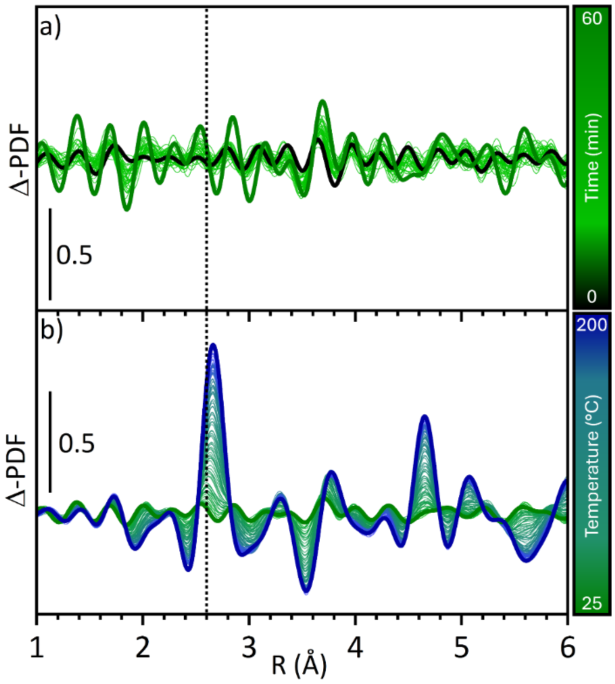

Figure 4.5 Evolution of the Δ-PDF patterns of RuAl, obtained by subtracting the first pattern of the dataset from the subsequent ones, during H_2-TPR experiment: (a) isothermal segment at 25 °C; (b) TPR ramp from 25 °C up to 200 °C.

A similar trend is observed in the PDF data for RuAl during the temperature ramp (Figure 4.5b), where the most intense Ru metal signal rising (~2.7 Å) initially shows a shoulder centered around 2.6 Å, attributable to the intermediate phase. During the isothermal equilibration step it is more difficult to spot the same trends in signals as in Ru_{uns}. Foremost the Ru amount probed is significantly lower in the cell (5wt% in RuAl against 76% in Ru_{uns}), worsening the signal to noise ratio. In this case, the varying scattering contribution of the support can be sidestepped by applying the PCA/MCR-ALS approach described previously to the XRD data collected during the same experiment (Figure 4.6a).

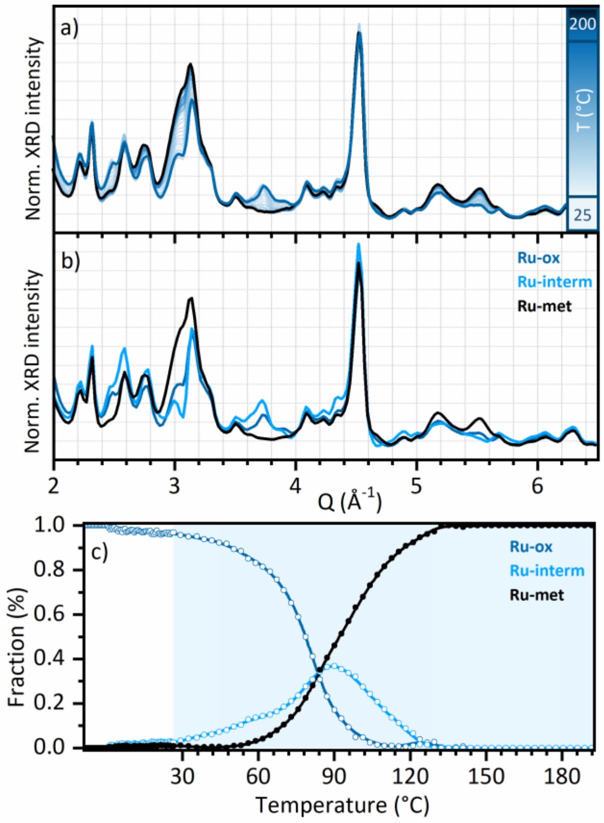

Figure 4.6. (a) Evolution of the XRD patterns of RuAl during the whole H_2-TPR experiment. (b) MCR optimized components, and (c) MCR optimized fraction profiles (c) as a function of time (white background) or temperature (blue background).

The analysis identified three components in the raw data (Figure 4.6b), corresponding to the initial and final patterns of the dataset, and a third component distinctive of the intermediate phase (Ru-interm). The evolution of the relative concentration of these three components over time/temperature (Figure 4.6c) closely matches the concentration profiles derived from the XAS data (Figure 4.2f), confirming with an independent technique the origin of the two reduction events observed by H_2-TPR.

Concerning the nature of the intermediate phase, the corresponding optimized pattern (Figure 4.6b) resembles that of rutile RuO_2, but with peaks shifted to lower Q values, indicating lattice expansion. Similar effects were reported for oxygen-deficient RuO_2 systems, *i.e.* RuO_{2-x},[5,6] and are well-documented in other reducible metal oxides, such as CeO_2.[7–9] The formation of oxygen vacancies leads to partial reduction of the metal ions, which have larger ionic radii, and also to a decrease in the covalency between the metal and the oxygen (*i.e.* a decrease in M-O bond strength). Both phenomena contribute to the observed lattice expansion. Although it was not possible to isolate distinct XRD signals confirming the presence of a corundum-like Ru_2O_3 intermediate phase, the observed lattice expansion and the formation of oxygen vacancies are consistent with the emergence of a less densely packed structure, such as corundum Ru_2O_3. XRD is more sensitive to the large crystalline RuO_2 domains (such as those detected by HR-TEM, Figure 3.2). In these domains, the formation of a corundum-like structure is likely confined to defects, unstable exposed surfaces, or interfaces with the support. In contrast, the small amorphous Ru nanoparticles are more likely to host the intermediate phase, but due to their lack of long-range order, they do not contribute significantly to the XRD signal. This structural heterogeneity within the RuAl system, where crystalline and amorphous domains coexist, can therefore explain the discrepancies observed between different characterization techniques.

4.3 Surface evolution during activation of RuAl

4.3.1 Thermal dehydration in He

The bulk-sensitive analysis presented in Section 4.2 demonstrated that the reduction of DP-derived Ru oxy-hydroxide phases proceeds through a non-trivial pathway involving a transient Ru(III)-containing intermediate. However, bulk structural information alone does not capture how the catalyst surface (i.e. where hydrogen activation and catalytic reactions occur) evolves during activation. In particular, it remains unclear how dehydration, oxygen restructuring and hydrogen exposure modify the population of surface oxygen species and the availability of reactive Ru sites. To address these questions, the evolution of surface species was investigated by combining *in situ* IR spectroscopy and O K-edge NEXAFS under activation conditions analogous to those employed in Section 4.2. RuAl was selected as a model system, as it provides a well-defined Ru–alumina interface and allows the direct correlation between bulk reduction phenomena and surface chemistry.

As a first step, RuAl was subjected to a mild thermal treatment under flowing He up to 200°C, aimed at progressively removing physisorbed water. This dehydration step was intentionally introduced as preconditioning for surface sensitive spectroscopies, aimed at progressively removing molecularly adsorbed water to enhance the visibility of the intrinsic spectroscopic fingerprints of surface oxygen species and, in subsequent steps, hydrogen-derived intermediates. The process was monitored by means of *in situ* IR spectroscopy and O K-edge NEXAFS (Figure 4.7), allowing a direct correlation between the evolution of surface hydrogen-containing species and the coordination environment of oxygen at the Ru–support interface.

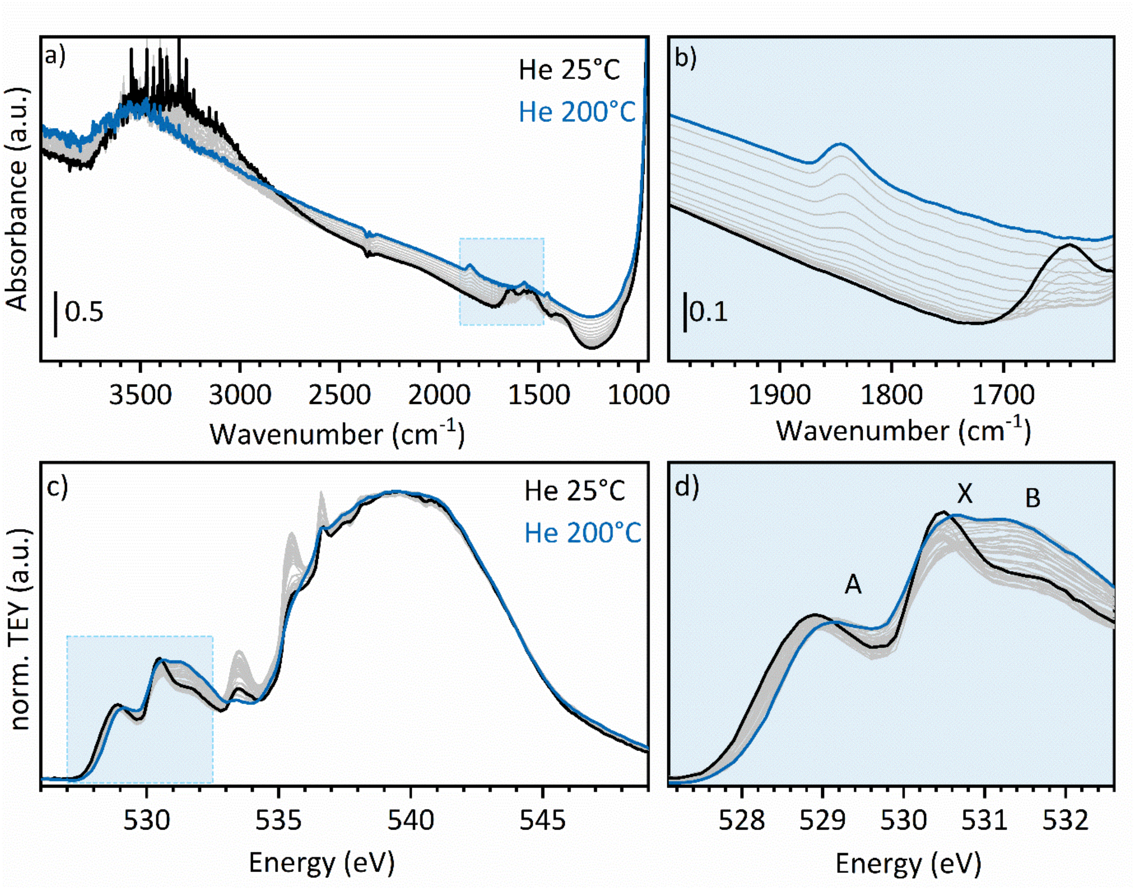

Figure 4.7 (a) *In situ* IR spectra and (c) normalized O K-edge NEXAFS spectra of RuAl collected during dehydration under inert flow in the 25 – 200 °C temperature range. Panels (b) and (d) report a magnification of the most relevant spectral regions.

The initial IR spectrum (Figure 4.7 a) is dominated by vibrational features characteristic of a hydrated alumina surface.[10,11] In particular, a broad and intense absorption centered around ~3500 cm^{-1} is observed, arising from the stretching vibrations of surface hydroxyl groups and physisorbed water molecules engaged in an extended hydrogen-bonding network. A band at 1644 cm^{-1} is also present and is assigned to the bending mode of molecular water. In the 1700-1300 cm^{-1} region, a few additional bands are observed, likely arising from a combination of water-related modes and weakly adsorbed surface species. At this stage, the IR response is therefore dominated by support-related contributions, and the strong vibrational signatures of adsorbed water largely mask any potential contribution from Ru-associated surface species. The O K-edge NEXAFS spectrum of the pristine catalyst (Figure 4.7 c,d) has been extensively analyzed in Chapter 3.

As shown in Figure 4.7 a, increasing the temperature under He flow leads to a progressive depletion of the IR bands associated with physisorbed water indicating effective dehydration of the surface. In parallel, the overall absorption baseline of the spectra progressively increases with temperature, an effect attributed to enhanced thermal scattering. This behavior is commonly observed during *in situ* heating experiments and does not carry specific chemical significance. As the dominant water-related contributions are progressively suppressed, a weak but reproducible IR band becomes discernible around 1840 cm^{-1} region (Figure 4.7 b). The assignment of this band is far from trivial. Features in this spectral region are rarely observed for pristine catalysts and mostly associated with overtones of various fundamental Ru-O stretching vibrations expected to occur in the 800-1000 cm^{-1} region.[12–14] IR spectroscopy alone does not provide sufficient specificity to discriminate among these possibilities, and the origin of this band must be analyzed in conjunction with complementary information on the evolution of surface oxygen species. In this respect, O K-edge NEXAFS provides direct insight into the restructuring of oxygen-containing species at the RuO_{2-x} surface during dehydration.

The temperature-dependent evolution of the NEXAFS spectra (Figure 4.7 d) provides the required chemical context to rationalize the emergence of the IR band. During the dehydration, peak A (associated with the Ru(4dt_{2g}) orbitals) progressively shifts towards higher energy, indicating a modification of the oxygen coordination and electronic environment at the Ru-oxide surface upon water removal. This evolution reflects a progressive depletion of weakly bound and protonated μ_1(OH) species (poorly visible), which are converted into more strongly bound μ_2(O) species via dihydroxylation. The onset of this transformation coincides with the appearance of the IR band around 1840 cm^{-1}. At the same time, peak X (associated with peroxo species) decreases in intensity and shifts to higher energy, indicating partial consumption or transformation of these species during dehydration. Concomitantly, the A/B peak intensity ratio decreases to ~0.6, and a −0.5 eV shift in the Ru M_2-edge is observed (Figure A7), providing independent evidence for partial surface reduction and the formation of a sub-stoichiometric RuO_{2-x} phase. Within this framework, the loss of μ_1(O)/μ_1(OH) species is therefore not a simple desorption process, but is intrinsically connected to oxygen condensation, vacancy formation, and the electronic reduction of the Ru-oxide surface.

In parallel to these changes in the Ru-related spectral features, additional sharp resonances appear at 533.4, 535.4, and 536.6 eV in the O K-edge spectra. These features are characteristic of gas-phase H_2O and arise from electronic transitions associated with molecular water released during dehydration and surface de-hydroxylation. The observation of these gas-phase contributions is strongly influenced by the geometry of the experimental cell, which partially confines reaction products and allows transient accumulation of desorbed species in the probed volume. As a result, the intensity of the gas-phase H_2O peaks increases during the dehydration ramp, reaches a maximum, and then gradually decreases, following a kinetic behavior governed by the balance between H_2O production at the surface and its removal by the inert gas flow. The exact temporal evolution of these features is therefore determined by cell geometry and by the efficiency of gas exchange, rather than by intrinsic changes in surface chemistry.

Based on these combined spectroscopic observations, the IR absorption band appearing at ~1840 cm^{-1} is proposed to be reflecting the vibrational signature of peroxo-related surface species undergoing a coordination rearrangement during dehydration. At low temperature, Ru-O-O groups are likely present in “bent” configuration, stabilized by hydrogen bonding with neighboring surface hydroxyls. In this highly hydrated and heterogeneous environment, their vibrational modes are expected to be weak, broadened, and largely obscured by intense OH-related features. Progressive removal of surface hydroxyl groups upon heating disrupts these stabilizing interactions, favoring a reorganization of peroxo species into a more symmetric side-on (η^2) coordination geometry at the Ru-oxide surface. Coordination-driven rearrangements of peroxo species and their impact on metal–oxygen electronic coupling have been highlighted by recent density functional theory studies, including the work of Di Liberto et al.,[15] who showed that changes in peroxo geometry are accompanied by substantial modifications of the electronic structure and bonding character at oxide surfaces. Such a configuration enhances metal–oxygen orbital overlap and vibrational coupling, rendering overtone or combination modes of the O–O and Ru–O stretches more likely to become observable. In this context, the band observed at ~1840 cm^{-1} can be rationalized as an overtone associated with side-on coordinated peroxo species, rather than as the overtone of a single Ru=O vibration.

Overall, the combined IR and O K-edge NEXAFS data reveal that thermal dehydration is not a passive removal of water, but an active restructuring process of the Ru-oxide surface. This process involves hydroxyl condensation, peroxo rearrangement, partial surface reduction, oxygen vacancy formation, and the stabilization of a defective RuO_{2-x} phase. The IR band at ~1840 cm^{-1} thus emerges as a sensitive marker of this surface reorganization, while NEXAFS provides the chemical specificity required to rationalize its origin.

4.3.2 H_2 reduction of the RuO_{2-x} phase and transient hydride formation

The reducibility of the supported RuO_{2-x} phase and the evolution of surface species under hydrogen were investigated by *in situ* IR spectroscopy and O K-edge NEXAFS, following a temperature program analogous to classical H_2-TPR experiments after the dehydration treatment (Figure 4.8).

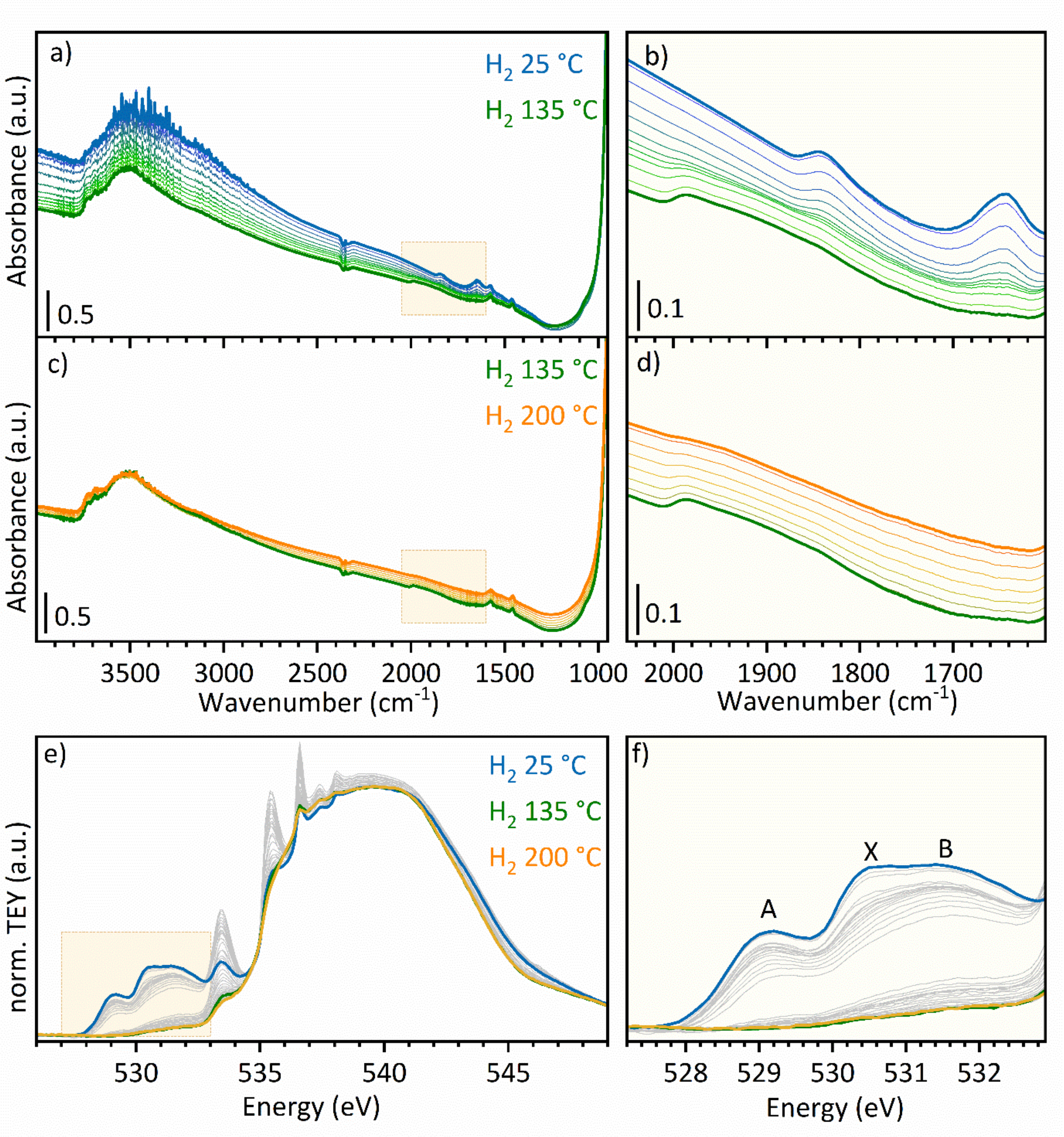

Figure 4.8 (a,c) *In situ* IR and (e) normalized O K-edge spectra of RuAl collected during H_2-TPR in the 25 – 200°C temperature range. Parts (b,d) and (f) report a magnification of the most relevant spectral regions.

Upon exposure of the dehydrated catalyst to H_2, the IR band observed after dehydration at ~1840 cm^{-1} rapidly vanishes (Figure 4.8 a,b). This abrupt disappearance occurs in parallel with the attenuation of the NEXAFS peak X previously associated with peroxo-like Ru–O–O surface species (Figure 4.8 e,f), indicating that these oxygenated functionalities do not survive under reducing conditions and are removed at the early stages of hydrogen activation. This behavior is fully consistent with the expected instability of peroxo upon hydrogen activation, which promotes O–O bond cleavage and oxygen removal as H_2O.

As reduction proceeds, the IR spectra reveal the transient formation of new hydrogen-containing surface species. A and weak envelope of contributions in the ~2000-1850 cm^{-1} region appears (Figure 4.8 a,b), which is characteristic of an ensemble of ν(Ru–H) stretching vibrations.[16–18] These bands reach a maximum intensity at approximately 135 °C and then disappear upon further heating (Figure 4.8 c,d), indicating the formation of Ru–hydride species as short-lived intermediates during the reduction of the RuO_{2-x} phase. Importantly, the disappearance of these bands does not necessarily imply a decrease in the total amount of hydrogen adsorbed on the surface of Ru nanoparticles. The IR response selectively probes IR-active Ru–H species, which are predominantly linear (atop) hydrides, whereas at increasing temperature hydrogen atoms are expected to preferentially occupy multi-coordinated (bridged or hollow) and/or subsurface sites that are significantly less IR-visible or effectively IR-silent. The attenuation of the ν(Ru–H) band is therefore more appropriately interpreted as a redistribution of hydrogen among different adsorption geometries rather than as the loss of hydride species altogether.

During the hydrogen reduction ramp, the IR spectra also display an unconventional evolution of the absorption background (Figure 4.8 a). With increasing temperature, a gradual increase of the baseline would normally be expected due to enhanced thermal scattering, as observed during the dehydration step. In contrast, under H_2 the baseline decreases up to ~135 °C before rising again at higher temperature. This opposite trend cannot be attributed to purely thermal effects and is instead interpreted as the disappearance of a low-energy electronic contribution associated with the defective RuO_{2-x} phase. Such a contribution, arising from electronic transitions or band-gap-related tails extending into the mid-IR region, is progressively suppressed as the oxide phase is reduced and its electronic structure collapses toward a metallic state. Indeed, semiconductor properties of the RuO_2 phase have been proposed for some crystal phases[19,20] and generally RuO_2 is well employed to produce electrodes being a conductive oxide.[21–25]

The hydrogen-induced reduction pathway is consistently captured by O K-edge NEXAFS (Figure 4.8 e,f). The progressive disappearance of Ru–O-related features (Figure

4.8 f), together with the appearance and subsequent decline of sharp resonances associated with gas-phase H_2O (Figure 4.8 e), provides direct evidence for oxygen removal via water formation. At the end of the reduction ramp, no residual oxidic signatures are detected, indicating that the reduction proceeds efficiently and essentially to completion. This behavior is likely facilitated by the high dispersion of Ru species on the alumina surface and by oxygen vacancies generated during the preceding dehydration step, which lower the kinetic barriers for hydrogen-induced oxygen removal.

4.3.3 Anchoring of Ru nanoparticles, hydride formation and hydrogen spillover: direct evidence from INS

The reduced Ru/Al_2O_3 catalyst was subsequently investigated by INS, a technique uniquely sensitive to hydrogen-containing species and free from the selection-rule limitations affecting IR spectroscopy. INS therefore provides direct access to hydrogen populations that are invisible or only indirectly inferred by vibrational spectroscopies, making it ideally suited to validate the conclusions drawn from the combined IR and NEXAFS analysis discussed above. In particular, it is complementary to IR because it accesses low wavenumbers region where bridged/hollow hydrides contribute.

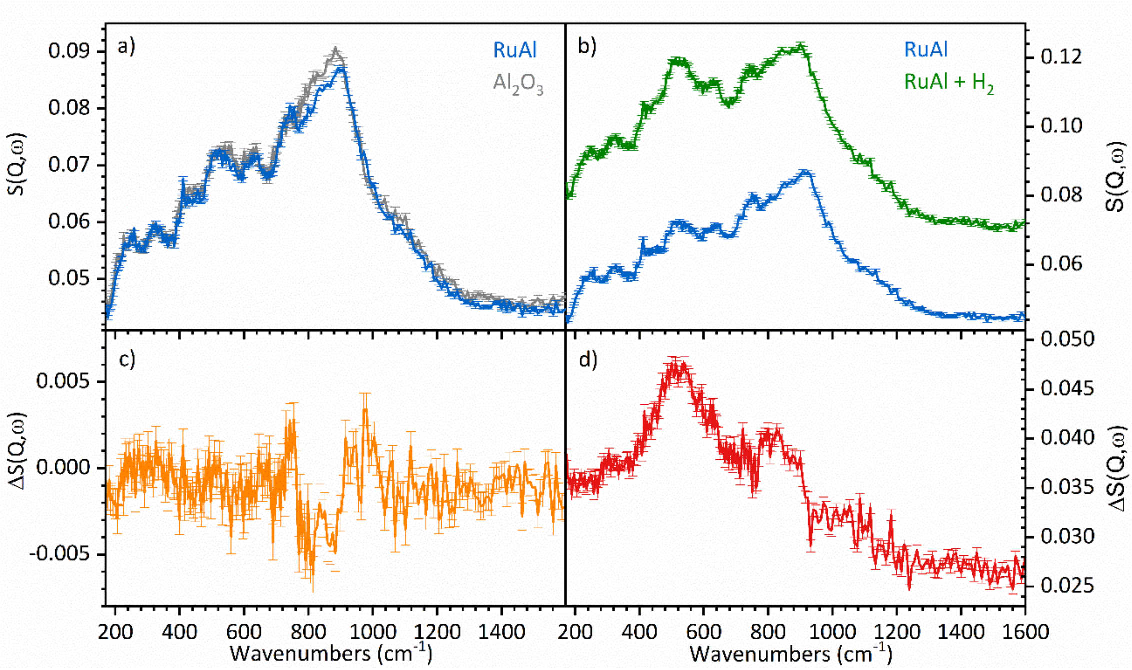

Figure 4.9 (a) INS spectra of RuAl after H_2-reduction, compared to that of the bare alumina support treated under identical conditions, and (c) result of the subtraction of Al_2O_3 from RuAl . (b) INS spectra of reduced RuAl before and after dosing H_2 (~400 mbar) and (d) result of the subtraction of RuAl from RuAl + H_2.

Figure 4.9 a compares the INS spectrum of the reduced Ru/Al_2O_3 catalyst with that of the bare Al_2O_3 support activated under identical conditions. The spectra are very similar, reflecting the dominant contribution of the alumina lattice.[26,27] However, significant differences emerge in the spectral region associated with surface hydroxyl groups. To isolate these effects, a difference spectrum RuAl- Al_2O_3 was calculated (Figure 4.9 c), revealing a dominating negative contribution with minima around 814 cm^{-1} and 883 cm^{-1}, along with positive sharp and weak bands centered around 754 cm^{-1} and 980 cm^{-1}. The negative features correspond to bending modes of surface OH groups on alumina, indicating that the presence of the Ru nanoparticles leads to a measurable depletion of surface hydroxyls on the support. This can be interpreted as evidence of chemical anchoring of RuO_{2-x} species, and subsequently reduced Ru nanoparticles, onto the alumina surface via condensation reactions involving surface hydroxyls, in line with the loss of μ_1(OH) species inferred from O K-edge NEXAFS during dehydration. The positive contributions observed, on the other hand, indicate the formation of other localized surface OH groups having similar vibration energies. This is compatible with O K-edge NEXAFS observations supporting the presence of μ_1(OH) and μ_2(OH) in the pristine catalyst.

To further probe hydrogen-related species, the experiment was continued by dosing excess H_2 at room temperature and subsequently cooling the system to 20 K to kill Debie-Waller factor and stabilize hydrogen on the surface. Figure 4.9 b compares INS spectra collected under vacuumed and after H_2 dosing. After subtraction of the spectrum of the reduced catalyst from that recorded in the presence of H_2 (Figure 4.9 d), a broad feature centered around 518 cm^{-1} becomes evident. This band is assigned to vibrational modes of multi-coordinated Ru–H species, such as bridged and/or hollow hydrides, rather than to terminal Ru–H groups. Both experimental INS studies and density functional theory calculations on Ru clusters and nanoparticles have shown that hydrogen occupying multi-coordinated or subsurface sites gives rise to intense low-frequency modes in the 400–600 cm^{-1} range, while being weakly IR-active or effectively IR-silent.[28–33] The observation of the ~500 cm^{-1} INS feature therefore provides direct evidence for hydrogen populations that persist on the Ru surface even when IR signatures of ν(Ru–H) vanish, consistent with a redistribution of hydrogen toward more stable, multi-coordinated adsorption sites at increasing temperature.

Remarkably, the difference INS spectrum also shows a partial recovery of the OH-related features around 815 cm^{-1} and 887 cm^{-1} upon H_2 exposure. The simultaneous appearances of Ru–H vibrational modes and regeneration of alumina OH groups constitute direct and unambiguous evidence of hydrogen spillover, whereby hydrogen atoms activated on Ru migrate onto the support and recombine with surface oxygen to form hydroxyl species. Such a process, frequently invoked in heterogeneous catalysis but rarely observed directly, is here captured thanks to the intrinsic hydrogen sensitivity of INS.

Taken together, the INS results provide a unifying picture that extends the IR and NEXAFS observations. They demonstrate that (i) hydrogen is stored on Ru nanoparticles in forms that are largely inaccessible to IR spectroscopy, (ii) surface hydroxyls at the Ru–Al_2O_3 interface actively participate in hydrogen exchange, and (iii) hydrogen spillover is operative under the investigated conditions. This dynamic interplay between Ru nanoparticles and the alumina support is expected to play a key role in hydrogenation catalysis, by extending the reactive hydrogen reservoir beyond the metal surface and enabling synergistic reaction pathways involving both metal and support sites.

4.4 Catalytic tests: identifying the active catalytic species in the hydrogenation of benzaldehyde

The surface-sensitive spectroscopic results discussed above reveal that the activation of RuAl is not a simple reduction process, but involves a sequence of coupled surface phenomena, including dehydration-induced restructuring of the oxidized Ru phase, transient hydride formation, and hydrogen spillover at the metal–support interface. These processes define the chemical nature and availability of hydrogen at the catalyst surface and, therefore, are expected to have direct consequences for hydrogenation reactivity. Importantly, the spectroscopic evidence indicates that different surface states, ranging from hydrated and partially reduced RuO_{2-x} species to fully metallic Ru nanoparticles, can coexist or emerge sequentially depending on temperature and atmosphere. This raises a critical question that cannot be addressed by structural and spectroscopic analysis alone: which of these states is actually responsible for catalytic hydrogenation activity, and under which conditions?

To answer this question, the structural and surface evolution framework developed in Sections 4.2 and 4.3 was tested against catalytic performance data. In the following section, the hydrogenation of benzaldehyde is employed as a probe reaction to assess the relative activity of unsupported and alumina-supported Ru catalysts under mild conditions, allowing the contribution of oxidic, partially reduced and metallic Ru states to be directly compared. The hydrogenation of benzaldehyde in tetrahydrofuran (THF) under 10 bar of H_2 for 3 h was studied at four different temperatures: 50, 75, 100, and 125 °C. THF was intentionally selected as an aprotic, chemically inert solvent to avoid hydrogen transfer mechanisms, such as the Meerwein–Ponndorf–Verley (MPV) reaction, which might obscure the intrinsic catalytic contributions of the Ru phases, particularly in RuAl catalyst where Al_2O_3 can promote catalytic transfer hydrogenation (CTH) reactions.[34,35] Both catalysts were introduced in their pristine, oxidized forms without pre-reduction. The selected reaction time allowed for gradual *in situ* activation, offering a window into the evolution of catalytic performance as a function of temperature.

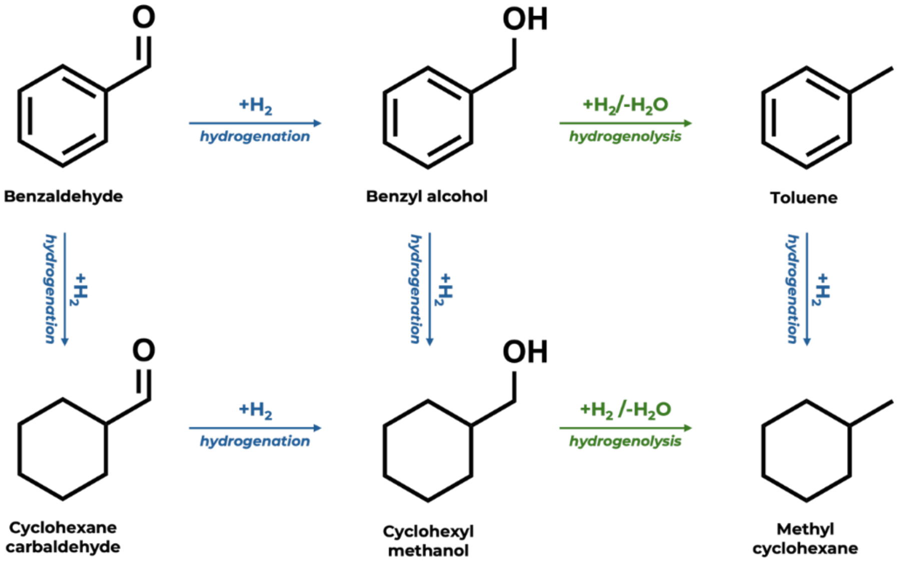

Figure 4.10 Reaction pathways in the hydrogenation and hydrogenolysis of benzaldehyde.

Under all experimental conditions and with both catalysts, no side products were detected. This level of selectivity, achieved despite the known propensity of benzaldehyde to undergo competing pathways such as hydrogenolysis and aromatic saturation (Figure 4.10),[36] is particularly noteworthy and ensures that the observed reactivity is exclusively associated with the hydrogenation of the carbonyl group. This allows for a direct and meaningful comparison of the intrinsic catalytic activity of the two catalysts toward the selective transformation of the C=O bond in benzaldehyde.

The catalytic behavior of Ru_{uns} and RuAl is significantly different, particularly at lower temperatures (Figure 4.11). RuAl exhibits a low activity at 50 °C, and even at 75 °C, the observed conversion remains modest (31%). This behavior can be attributed to the higher reduction threshold of the supported rutile-like RuO_2 nanoparticles evidenced by H_2-TPR. The emergence of significant activity only above 100 °C, culminating in 72% conversion at 150 °C, mirrors the progressive *in situ* formation of metallic Ru, the known active phase under such conditions.

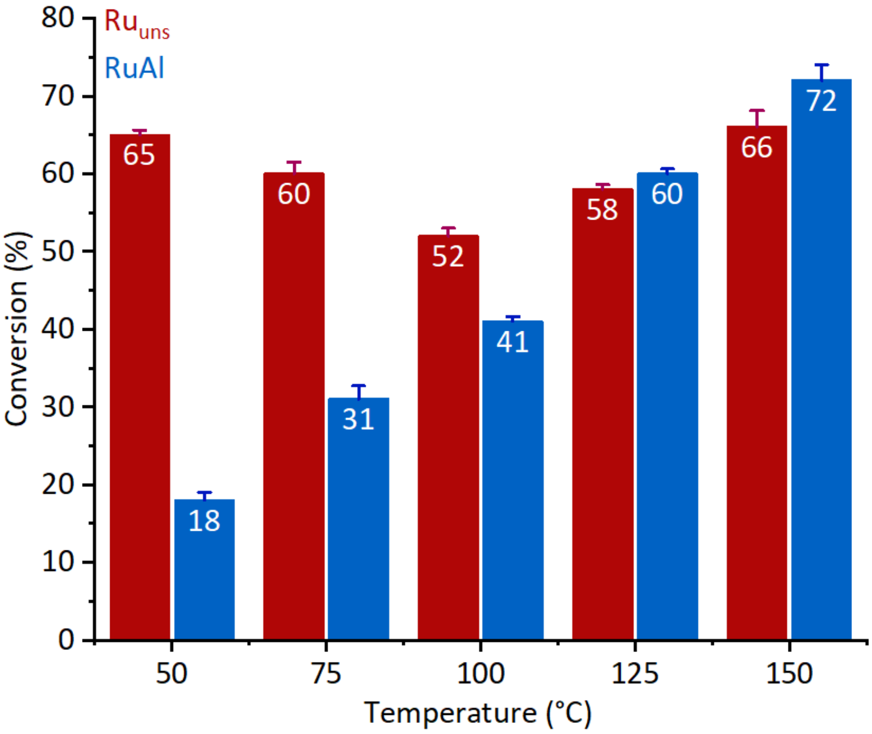

Figure 4.11 Effect of the reaction temperature in the hydrogenation of benzaldehyde over Ru$_{uns}$ and RuAl catalysts.

In marked contrast, the catalytic performance of unsupported Ru$_{uns}$ displays a non-monotonic dependence on temperature. Surprisingly, it achieves a peak conversion of 65% at only 50 °C, despite the minimal extent of reduction at this temperature. XAS and PDF data revealed that the starting material is an amorphous, highly hydrated $RuO_x(OH)_Y$ network comprising edge-sharing [RuO_6] octahedra. This disordered architecture appears to unlock reactivity inaccessible to the more crystalline RuO_2 analogue supported on alumina. These findings are consistent with previous surface studies showing that molecular H_2 can dissociate heterolytically on RuO_2(110) at low temperatures, forming reactive hydride–hydroxyl pairs through cooperative interactions between fivefold-coordinated Ru sites and bridging oxygen atoms.[37,38] RuO_2 is also known to be able to incorporate hydrogen in the bulk. Hydrous $RuO_2{\cdot}xH_2O$ is commonly used in the context of supercapacitors, where its superior performance is attributed to intercalation of hydrogen (in the form of protons) and one-dimensional diffusion along the RuO_6 chains. Accordingly, a hydrogenated RuO_2 phase (e.g., H_xRuO_2) was successfully employed for selective hydrogenation reactions in the absence of metallic Ru.[39] Together, these results support the conclusion that the amorphous and partially hydrated $RuO_x(OH)_y$ phase characterizing Ru$_{uns}$ is not merely a precursor, but an intrinsically active catalyst, capable of activating H_2 and enabling carbonyl hydrogenation under thermodynamically mild conditions.

Upon increasing the reaction temperature, the activity of RuO_2 declines to 60% at 75 °C and further to 52% at 100 °C. *In situ* characterization reveals this regime coincides with the formation of a Ru_2O_3-like intermediate, which disrupts the original amorphous motif. This phase, although structurally defined, is less catalytically active. Interestingly, catalytic activity is recovered above 125 °C, which is likely related to the formation of metallic Ru nanoparticles. Yet, the maximum activity in this fully reduced state remains lower than that of the pristine oxidic phase at 50 °C and of RuAl at equivalent temperatures. Structural data reveal that sintering and particle coalescence dominate in Ru_{uns} at high temperature, reducing the active surface area and undermining its effectiveness.

To further clarify the role of the active species, additional catalytic tests were performed on both catalysts after pre-reduction in H_2 at 150 °C. At 150 °C, both pre-reduced catalysts exhibit catalytic activities comparable to their pristine counterparts (**Error! Reference source not found.**), which undergo *in situ* reduction under these conditions. However, as the reaction temperature decreases, distinct differences emerge. Pre-reduced RuAl catalyst exhibits a linear decrease in activity with decreasing temperature, consistently outperforming the unreduced RuAl. This behavior indicates that metallic Ru is the active phase and that pre-reduction enhances its performances, particularly at low reaction temperatures. Similarly, the activity of the pre-reduced Ru_{uns} also decreases linearly with the temperature, but remains lower than that of RuAl, likely due to the absence of a stabilizing support for metallic Ru species. A particularly striking result is obtained at 50 °C, where the pre-reduced Ru_{uns} catalyst shows markedly low activity, with a conversion of only 14%, in sharp contrast to 65% conversion achieved by the unreduced Ru_{uns} under identical conditions. This pronounced difference clearly demonstrates that in Ru_{uns} the active species at low-temperature are not metallic Ru^0 sites, but rather oxidized $RuO_X(OH)_Y$ species present in the pristine material. This conclusion is further supported by XRD analysis of Ru_{uns} recovered after reaction at 50 °C (Figure A *9*), confirming that the amorphous structure remains largely intact, thereby indicating that no significant *in situ* reduction occurred under these conditions.

To assess the practical viability of this unconventional oxidic phase, five consecutive reaction cycles were performed at 50 °C (Figure A *10*). Ru_{uns} retained approximately 70% of its initial activity (conversion decreased from 65% to 46%). This moderate decline may be attributed to partial surface poisoning by adsorbed species. Moreover, the unchanged phase composition obtained by XRD analysis of Ru_{uns} recovered after catalytic testing at 50 °C (Figure A *9*) also supports the notion that the hydrated

$RuO_x(OH)_y$ network is not only catalytically active but also structurally stable under liquid-phase reaction conditions at low temperature.

Altogether, these catalytic insights highlight a paradigm shift: catalytic efficiency is not exclusively governed by the presence of metallic Ru, but also by the nature, hydration and disorder of oxidic precursors. Understanding and exploiting these unconventional reactivity patterns opens a new frontier for the design of advanced Ru-based catalysts operating under mild conditions.

4.5 Conclusions

This chapter provided a multiscale mechanistic description of the activation of DP-derived Ru catalysts, integrating bulk-sensitive techniques and surface-sensitive spectroscopies with catalytic testing. By combining H_2-TPR with *in situ* synchrotron techniques (Ru K-edge XAS, high-energy total scattering PDF and XRD), the reduction of both Ru_{uns} and RuAl was shown to proceed through a non-trivial pathway involving a transient Ru(III)-containing intermediate. Multivariate analysis of the XAS and XRD datasets demonstrated that this intermediate is a genuine bulk phase, whose formation and consumption account for the multiple reduction events observed in TPR thermograms. Structural fingerprints extracted from EXAFS and PDF revealed a characteristic short Ru–Ru distance (~2.6 Å) and lattice expansion effects consistent with oxygen-vacancy formation, supporting the assignment of a corundum-like Ru_2O_3 intermediate. Differences between Ru_{uns} and RuAl highlight the role of structural heterogeneity and metal–support interactions in stabilizing or masking this intermediate within specific domains, such as defects, amorphous regions, exposed surfaces and interfaces.

Focusing on RuAl, surface-sensitive *in situ* IR spectroscopy, O K-edge NEXAFS and INS revealed that activation is governed by a sequence of coupled surface processes. Thermal dehydration under inert atmosphere was shown to be an active restructuring step rather than a passive removal of water, promoting hydroxyl condensation, rearrangement of peroxo-like Ru–O–O species, partial surface reduction and the stabilization of a defective RuO_{2-x} phase. Upon exposure to hydrogen, oxygenated surface species are rapidly consumed through water formation, while transient Ru–hydride species are generated during the reduction process. IR spectroscopy selectively detected terminal Ru–H species, whereas INS provided direct evidence for hydrogen populations in multi-coordinated and subsurface configurations that remain largely inaccessible to IR probes. Crucially, INS measurements also delivered direct spectroscopic proof of hydrogen spillover at the Ru–

alumina interface, demonstrating dynamic hydrogen exchange between Ru nanoparticles and alumina surface hydroxyls.

Catalytic tests in the selective hydrogenation of benzaldehyde validated the mechanistic framework established by the combined bulk and surface investigations. The marked differences observed between Ru_{uns} and RuAl demonstrate that catalytic activity cannot be interpreted solely in terms of the presence of metallic Ru. The amorphous and partially hydrated $RuO_x(OH)_y$ phase characterizing Ru_{uns} exhibits significant activity under mild conditions, indicating that oxidic and partially reduced Ru states can directly participate in hydrogen activation and transfer. In contrast, RuAl requires higher temperatures to achieve substantial activity, consistent with the progressive formation of metallic Ru sites stabilized by the support. These results challenge the conventional assumption that fully reduced metallic Ru is the exclusive active phase in Ru-based hydrogenation catalysis and highlight the functional relevance of precursor structure, hydration and disorder.

Overall, this chapter establishes a coherent picture in which bulk reduction through a transient Ru(III) intermediate, surface oxygen restructuring, hydride formation and hydrogen spillover are intimately coupled processes governing hydrogen activation on DP-derived Ru catalysts. By explicitly linking structural evolution across length scales to catalytic performance, the results lay the mechanistic foundation for the final chapter, where the roles of drying, ageing and water content are discussed as key variables controlling the stability, reproducibility and performance of Ru catalysts prepared by deposition–precipitation.

References

(1) McKeown, D. A.; Hagans, P. L.; Carette, L. P. L.; Russell, A. E.; Swider, K. E.; Rolison, D. R. Structure of Hydrous Ruthenium Oxides: Implications for Charge Storage. *J. Phys. Chem. B* **1999**, *103* (23), 4825–4832. https://doi.org/10.1021/jp990096n.

(2) Donakowski, M. D.; Mansour, A. N.; Pala, I. R.; Chervin, C. N.; DeSario, P. A.; Long, J. W.; Rolison, D. R. Trapping a Ru2O3 Corundum-like Structure at Ultrathin, Disordered RuO2 Nanoskins Expressed in 3D. *The Journal of Physical Chemistry C* **2018**, *122* (50), 28895–28900.

(3) Owen, E. A.; Pickup, L.; Roberts, I. O.; Sc., M. Lattice Constants of Five Elements Possessing Hexagonal Structure. **1935**, *91* (1–6), 70–76. https://doi.org/doi:10.1524/zkri.1935.91.1.70.

(4) *https://www.osti.gov/dataexplorer/biblio/dataset/1206459*.

(5) Yang, J.; An, K.; Yu, Z.; Qiao, L.; Cao, Y.; Zhuang, Y.; Liu, C.; Li, L.; Peng, L.; Pan, H. Effect of Cation and Anion Vacancies in Ruthenium Oxide on the Activity and Stability of Acidic Oxygen Evolution. *ACS Catal.* **2024**, *14* (23), 17739–17747. https://doi.org/10.1021/acscatal.4c02779.

(6) Ping, X.; Liu, Y.; Zheng, L.; Song, Y.; Guo, L.; Chen, S.; Wei, Z. Locking the Lattice Oxygen in RuO2 to Stabilize Highly Active Ru Sites in Acidic Water Oxidation. *Nat. Commun.* **2024**, *15* (1), 2501. https://doi.org/10.1038/s41467-024-46815-6.

(7) Jaffari, G. H.; Imran, A.; Bah, M.; Ali, A.; Bhatti, A. S.; Qurashi, U. S.; Ismat Shah, S. Identification and Quantification of Oxygen Vacancies in CeO2 Nanocrystals and Their Role in Formation of F-Centers. *Appl. Surf. Sci.* **2017**, *396*, 547–553. https://doi.org/https://doi.org/10.1016/j.apsusc.2016.10.193.

(8) Choudhury, B.; Choudhury, A. Ce3+ and Oxygen Vacancy Mediated Tuning of Structural and Optical Properties of CeO2 Nanoparticles. *Mater. Chem. Phys.* **2012**, *131* (3), 666–671. https://doi.org/https://doi.org/10.1016/j.matchemphys.2011.10.032.

(9) Hailstone, R. K.; DiFrancesco, A. G.; Leong, J. G.; Allston, T. D.; Reed, K. J. A Study of Lattice Expansion in CeO2 Nanoparticles by Transmission Electron Microscopy. *The Journal of Physical Chemistry C* **2009**, *113* (34), 15155–15159. https://doi.org/10.1021/jp903468m.

(10) Busca, G. Structural, Surface, and Catalytic Properties of Aluminas. *Advances in Catalysis* **2014**, *57*, 319–404. https://doi.org/10.1016/B978-0-12-800127-1.00003-5.

(11) Busca, G. Acid Catalysts in Industrial Hydrocarbon Chemistry. *Chem. Rev.* **2007**, *107* (11), 5366–5410. https://doi.org/10.1021/cr068042e.

(12) Hadjiivanov, K.; Lavalley, J.-C.; Lamotte, J.; Maugé, F.; Saint-Just, J.; Che, M. FTIR Study of CO Interaction with Ru/TiO2Catalysts. *J. Catal.* **1998**, *176* (2), 415–425. https://doi.org/https://doi.org/10.1006/jcat.1998.2038.

(13) Opre, Z.; Ferri, D.; Krumeich, F.; Mallat, T.; Baiker, A. Insight into the Nature of Active Redox Sites in Ru-Containing Hydroxyapatite by DRIFT Spectroscopy. *J. Catal.* **2007**, *251* (1), 48–58. https://doi.org/10.1016/J.JCAT.2007.07.017.

(14) Guglielminotti, E.; Boccuzzi, F.; Manzoli, M.; Pinna, F.; Scarpa, M. Ru/ZrO2 Catalysts: I. O2, CO, and NO Adsorption and Reactivity. *J. Catal.* **2000**, *192* (1), 149–157. https://doi.org/10.1006/JCAT.2000.2835.

(15) Di Liberto, G.; Pacchioni, G.; Shao-Horn, Y.; Giordano, L. Role of Water Solvation on the Key Intermediates Catalyzing Oxygen Evolution on RuO2. *The Journal of Physical Chemistry C* **2023**, *127* (21), 10127–10133. https://doi.org/10.1021/acs.jpcc.3c02733.

(16) Izumi, Y.; Hoshikawa, M.; Aika, K. Adsorbed Hydrogen Effect on the Adsorption and Reactivity of N2 Molecules on Ru/MgO and Ru–Cs+/MgO: Hydrogen Dipole Effect Enhanced by Doped Cs+. *Bull. Chem. Soc. Jpn.* **1994**, *67* (12), 3191–3200. https://doi.org/10.1246/bcsj.67.3191.

(17) Copéret, C.; Estes, D. P.; Larmier, K.; Searles, K. Isolated Surface Hydrides: Formation, Structure, and Reactivity. *Chem. Rev.* **2016**, *116* (15), 8463–8505. https://doi.org/10.1021/acs.chemrev.6b00082.

(18) Kubota, J.; Aika, K. FTIR Spectra of Terminal and Bridged Hydrogen Atoms Adsorbed on Ruthenium Metal Particles Dispersed on Magnesium Oxide. *J. Chem. Soc. Chem. Commun.* **1992**, No. 8, 661–662. https://doi.org/10.1039/C39920000661.

(19) Mehtougui, N.; Rached, D.; Khenata, R.; Rached, H.; Rabah, M.; Bin-Omran, S. Structural, Electronic and Mechanical Properties of RuO2 from First-Principles Calculations. *Mater. Sci. Semicond. Process.* **2012**, *15* (4), 331–339. https://doi.org/https://doi.org/10.1016/j.mssp.2012.02.001.

(20) Ko, D.-S.; Lee, W.-J.; Sul, S.; Jung, C.; Yun, D.-J.; Kim, H.-G.; Son, W.-J.; Chung, J. G.; Jung, D. W.; Kim, S. Y.; Kim, J.; Lee, W.; Kwak, C.; Shin, J. K.; Kim, J.-H.; Roh, J. W. Understanding the Structural, Electrical, and Optical Properties of Monolayer h-Phase RuO2 Nanosheets: A Combined Experimental and Computational Study. *NPG Asia Mater.* **2018**, *10* (4), 266–276. https://doi.org/10.1038/s41427-018-0020-y.

(21) Over, H. Ruthenium Dioxide, a Fascinating Material for Atomic Scale Surface Chemistry. *Applied Physics A* **2002**, *75* (1), 37–44. https://doi.org/10.1007/s003390101053.

(22) Over, H. Surface Chemistry of Ruthenium Dioxide in Heterogeneous Catalysis and Electrocatalysis: From Fundamental to Applied Research. *Chem. Rev.* **2012**, *112* (6), 3356–3426. https://doi.org/10.1021/CR200247N.

(23) Adeyemo, A.; Hunter, G.; Dutta, P. K. Interaction of CO with Hydrous Ruthenium Oxide and Development of a Chemoresistive Ambient CO Sensor. *Sens. Actuators B Chem.* **2011**, *152* (2), 307–315. https://doi.org/https://doi.org/10.1016/j.snb.2010.12.027.

(24) Qin, X.; Durbach, S.; Wu, G. Electrochemical Characterization on RuO2·XH2O/Carbon Nanotubes Composite Electrodes for High Energy Density Supercapacitors. *Carbon N. Y.* **2004**, *42*, 451–453. https://doi.org/10.1016/j.carbon.2003.11.012.

(25) Majumdar, D.; Maiyalagan, T.; Jiang, Z. Recent Progress in Ruthenium Oxide-Based Composites for Supercapacitor Applications. *ChemElectroChem* **2019**, *6* (17), 4343–4372. https://doi.org/https://doi.org/10.1002/celc.201900668.

(26) Vottero, E.; Carosso, M.; Ricchebuono, A.; Jiménez-Ruiz, M.; Pellegrini, R.; Chizallet, C.; Raybaud, P.; Groppo, E.; Piovano, A. Evidence for H2-Induced Ductility in a Pt/Al2O3 Catalyst. *ACS Catal.* **2022**, *12* (10), 5979–5989. https://doi.org/10.1021/acscatal.2c00606.

(27) Carosso, M.; Vottero, E.; Lazzarini, A.; Morandi, S.; Manzoli, M.; Lomachenko, K. A.; Ruiz, M. J.; Pellegrini, R.; Lamberti, C.; Piovano, A.; Groppo, E. Dynamics of Reactive Species and Reactant-Induced Reconstruction of Pt Clusters in Pt/Al2O3 Catalysts. *ACS Catal.* **2019**, *9* (8), 7124–7136. https://doi.org/10.1021/acscatal.9b02079.

(28) Yu, X.; Cheng, Y.; Li, Y.; Polo-Garzon, F.; Liu, J.; Mamontov, E.; Li, M.; Lennon, D.; Parker, S. F.; Ramirez-Cuesta, A. J.; Wu, Z. Neutron Scattering Studies of Heterogeneous Catalysis. *Chem. Rev.* **2023**, *123* (13), 8638–8700. https://doi.org/10.1021/acs.chemrev.3c00101.

(29) Heise, W. H.; Lu, K.; Kuo, Y. J.; Udovic, T. J.; Rush, J. J.; Tatarchuk, B. J. Neutron Scattering Study of Hydrogen on Ruthenium Sulfide. *J. Phys. Chem.* **1988**, *92* (18), 5184–5188. https://doi.org/10.1021/j100329a024.

(30) Cusinato, L.; Martínez-Prieto, L. M.; Chaudret, B.; del Rosal, I.; Poteau, R. Theoretical Characterization of the Surface Composition of Ruthenium Nanoparticles in Equilibrium with Syngas. *Nanoscale* **2016**, *8* (21), 10974–10992. https://doi.org/10.1039/C6NR01191H.

(31) Gutmann, T.; Walaszek, B.; Yeping, X.; Wächtler, M.; del Rosal, I.; Grünberg, A.; Poteau, R.; Axet, R.; Lavigne, G.; Chaudret, B.; Limbach, H.-H.; Buntkowsky, G. Hydrido-Ruthenium Cluster Complexes as Models for Reactive Surface Hydrogen Species of Ruthenium Nanoparticles. Solid-State 2H NMR and Quantum Chemical

Calculations. *J. Am. Chem. Soc.* **2010**, *132* (33), 11759–11767. https://doi.org/10.1021/ja104229a.

(32) Pery, T.; Pelzer, K.; Buntkowsky, G.; Philippot, K.; Limbach, H.-H.; Chaudret, B. Direct NMR Evidence for the Presence of Mobile Surface Hydrides on Ruthenium Nanoparticles. *ChemPhysChem* **2005**, *6* (4), 605–607. https://doi.org/https://doi.org/10.1002/cphc.200400621.

(33) Lara, P.; Philippot, K.; Chaudret, B. Organometallic Ruthenium Nanoparticles: A Comparative Study of the Influence of the Stabilizer on Their Characteristics and Reactivity. *ChemCatChem* **2013**, *5* (1), 28–45. https://doi.org/https://doi.org/10.1002/cctc.201200666.

(34) Wang, D.; Astruc, D. The Golden Age of Transfer Hydrogenation. *Chem. Rev.* **2015**, *115* (13), 6621–6686. https://doi.org/10.1021/acs.chemrev.5b00203.

(35) Gilkey, M. J.; Xu, B. Heterogeneous Catalytic Transfer Hydrogenation as an Effective Pathway in Biomass Upgrading. *ACS Catal.* **2016**, *6* (3), 1420–1436. https://doi.org/10.1021/acscatal.5b02171.

(36) Bhanushali, J. T.; Kainthla, I.; Keri, R. S.; Nagaraja, B. M. Catalytic Hydrogenation of Benzaldehyde for Selective Synthesis of Benzyl Alcohol: A Review. *ChemistrySelect* **2016**, *1* (13), 3839–3853. https://doi.org/https://doi.org/10.1002/slct.201600712.

(37) Dahal, A.; Mu, R.; Lyubinetsky, I.; Dohnálek, Z. Hydrogen Adsorption and Reaction on RuO2(110). *Surf. Sci.* **2018**, *677*, 264–270. https://doi.org/https://doi.org/10.1016/j.susc.2018.07.014.

(38) Jadon, A.; Rossi, C.; Djafari-Rouhani, M.; Estève, A.; Pech, D. Interaction of Hydrogen with the Bulk, Surface and Subsurface of Crystalline RuO2 from First Principles. *Physics Open* **2021**, *7*, 100059. https://doi.org/https://doi.org/10.1016/j.physo.2021.100059.

(39) Yang, H. J.; Redington, M.; Miller, D. P.; Zurek, E.; Kim, M.; Yoo, C.-S.; Lim, S. Y.; Cheong, H.; Chae, S.-A.; Ahn, D.; Hur, N. H. New Monoclinic Ruthenium Dioxide with Highly Selective Hydrogenation Activity. *Catal. Sci. Technol.* **2022**, *12* (21), 6556–6565. https://doi.org/10.1039/D2CY00815G.

Chapter 5

5 Drying, ageing and reducibility of Ru catalysts obtained via deposition-precipitation: the hidden role of water

5.1 Chapter overview and scope

In this chapter I will present the outcome of the systematic investigation of reducibility and accessibility of the oxy-hydroxide Ru phase obtained by deposition-precipitation. The results discussed in the previous chapters consistently point to water as a key, yet often implicit, variable in governing the structure and surface chemistry of supported Ru catalysts prepared by deposition–precipitation. While bulk and surface-sensitive spectroscopies revealed how hydration influences local coordination, reduction pathways and hydrogen activation, the specific role of water as a controllable synthetic and post-synthetic parameter has not yet been addressed explicitly. This chapter therefore focuses on water as an active structural component of the Ru oxy-hydroxide phase, rather than as residual moisture or an experimental artefact, to answer a key question that the previous chapters have outlined but never addressed directly: what is the role of water in the determination of structure, reducibility and stability of Ru-based catalysts synthesized by deposition-precipitation?

Investigating the effect of hydration in a controlled and reproducible manner required a dedicated experimental strategy, with particular attention to post-synthesis handling, storage and drying history of the catalysts. In contrast to the activation studies discussed previously, such long-term and systematic investigations are inherently incompatible with synchrotron-based techniques, which operate within limited experimental time windows. As a result, the present study deliberately relies on laboratory-scale techniques, namely H_2-TPR and CO pulsed chemisorption, which allow for extended, statistically robust investigations over multiple samples and conditions. This constraint was turned into an opportunity to establish a simple and transferable methodology, directly applicable to both academic studies and industrial catalyst development.

5.2 Effects of post-synthesis dehydration on reducibility and accessibility of Ru sites

To decouple support effects from hydration effects, the influence of the temperature employed during the overnight post-synthesis drying step was systematically investigated. Aliquots of RuAl, RuCw and RuCch were stored in the wet state after synthesis and dried immediately prior to characterization at controlled temperatures, yielding RuAl(w), RuCw(w) and RuCch(w). The evolution of reducibility and Ru site accessibility as a function of drying temperature was then quantified by H_2-TPR and CO chemisorption, providing a direct link between controlled dehydration, redox behavior and accessible surface Ru sites. The main quantitative parameters extracted from these experiments for all catalysts dried at different temperatures are summarized in Table 5. 1.

Figure 5.1 shows the evolution of the H_2-TPR profiles of RuAl as a function of drying temperature (part a), together with the corresponding fitting results (part b) and dispersion values obtained by CO chemisorption (part c). Drying below 90 °C yields thermograms dominated by a single broad reduction feature centered around 90 °C, whereas drying at and above 90 °C leads to the appearance of additional reduction contributions at higher temperature and to an overall shift of the profiles toward lower reducibility (higher temperature). To rationalize these changes, the H_2-TPR profiles of RuAl were fitted using three or four components, depending on the drying temperature (Figure 5.1a), as explained in Chapter 2. At low drying temperatures (< 90 °C), the reduction behavior is dominated by two contributions, peaks II and III. Peak III, which accounts for the largest fraction of H_2 consumption, is associated with reduction of hydrated $RuO_x(OH)_y$ agglomerates, characterized by a highly disordered and water-rich Ru–O–OH network in which the intrinsic Ru(IV) → Ru(III) → Ru(0) redox steps are kinetically overlapped. Peak II, present over the entire drying temperature range, is attributed to very small, highly defective Ru oxy-hydroxide nanoparticles that remain dispersed and do not participate in the formation of hydrated agglomerates. Owing to their limited structural extension, these nanoparticles undergo reduction through concerted redox processes in which intermediate Ru(III) species do not accumulate, resulting in a single unresolved contribution.

Table 5. 1 Reduction onset temperature (T_{start}), temperature of the main reduction maxima (T_{max}), H_2(ratio), defined as the experimental H_2 consumption determined from H_2-TPR measurements normalized to the theoretical value expected for complete reduction of RuO_2, and apparent Ru dispersion values obtained from pulsed CO chemisorption measurements, calculated assuming a CO/Ru adsorption stoichiometry of 1. All data refer to catalysts from the second aliquot, stored in the wet state after synthesis and dried overnight at the indicated temperatures (T_{dry}=70–120 °C) immediately prior to characterization.

Sample	**T_{dry} (°C)**	**H_2-TPR**			**D (%)**
		T_{start} (°C)	**T_{max} (°C)**	**H_2(ratio)**	
RuAl(w)	70	52	73 | 91	1.39	59
	80	50	76 | 97	1.42	57
	90	58	80 | 119	1.20	31
	100	56	79 | 124	1.14	33
	110	55	85 | 129	1.12	31
	120	62	85 | 132	1.10	29
RuCw(w)	70	43	83	1.28	83
	80	44	89	1.40	85
	90	51	88	1.30	82
	100	49	94	1.30	90
	110	53	94	1.36	95
	120	49	107	1.45	94
RuCCh(w)	70	54	81 | 90	1.10	57
	80	55	79 | 88	1.08	58
	90	54	81 | 90	1.16	58
	100	54	78 | 90	1.09	63
	110	57	82 | 91	1.13	67
	120	54	79 | 90	1.08	67

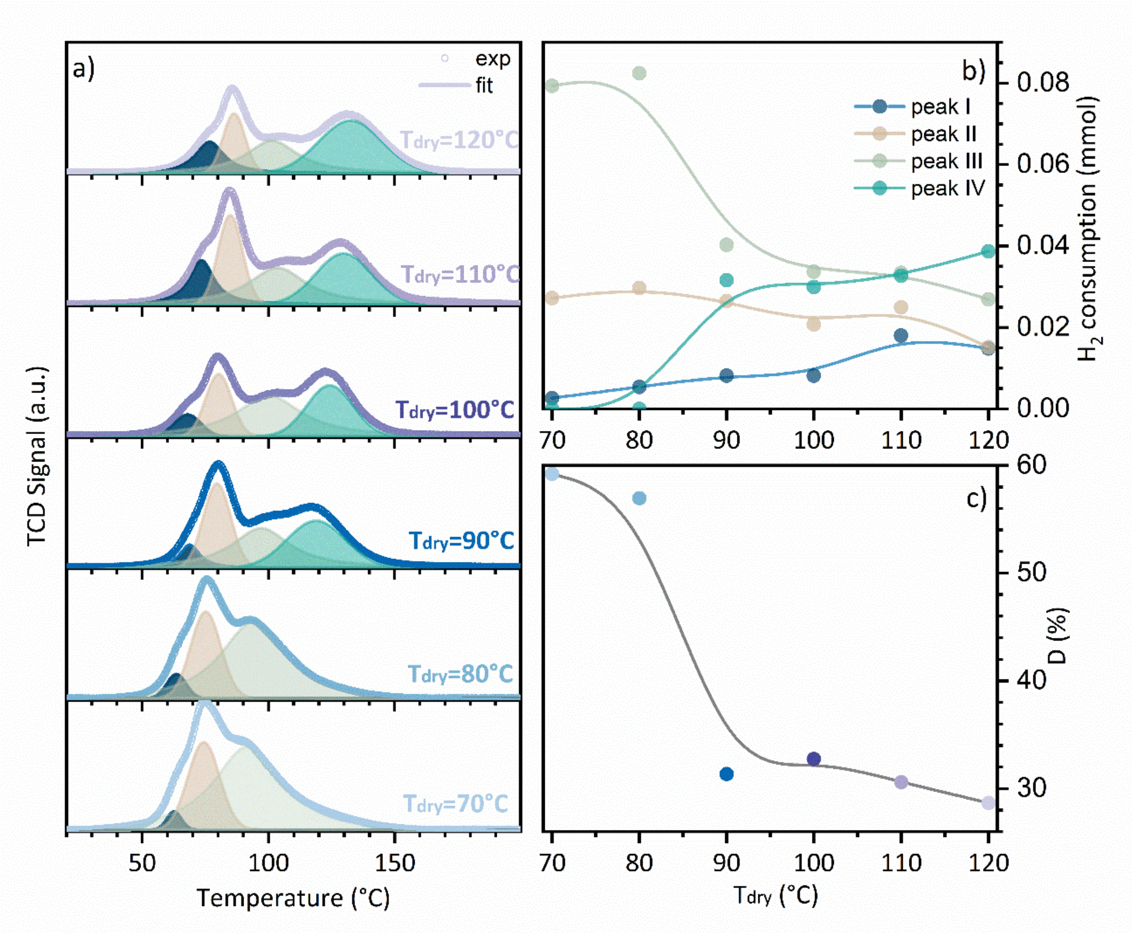

Figure 5.1 (a) H_2-TPR thermograms of RuAl(w) dried overnight at different temperatures in the 70-120 °C range: experimental data (open symbols), cumulative fit curve (solid line), and individual contributions used for the fits. (b) H_2 consumption values obtained from the integrated areas of the fitted H_2-TPR contributions, and (c) apparent Ru dispersion values from pulsed CO chemisorption, shown as a function of the drying temperature. In panels (b) and (c), the lines connecting the data points are guides to the eye.

Upon drying at 90 °C and above, the contribution of peak III progressively decreases and is replaced by two distinct components, peaks I and IV. Importantly, peaks I and IV originate from reduction of the same agglomerated Ru oxy-hydroxide domains responsible for peak III after partial dehydration. This dehydration is accompanied by partial structural reorganization of these agglomerates into more ordered RuO_2-like domains, consistent with the emergence of terminal μ_1(O) species observed by NEXAFS,[1,2] allowing the intrinsic Ru(IV) → Ru(III) and Ru(III) → Ru(0) redox steps to become kinetically separable and experimentally resolvable, consistent with what discussed so far on RuAl in previous chapters.

The redistribution of H_2 consumption among the fitted contributions is accompanied by a progressive decrease in total H_2 overconsumption with increasing drying temperature (Figure 5.1b). The H_2 consumption ratio decreases from approximately 40% overestimation at 70–80 °C to ~20% at 90 °C and ~10% at 120 °C (Table 5. 1), indicating a reduction in the population of non-stoichiometric oxygen species, such as peroxo-like Ru–OO moieties, and of highly defective, hydrated Ru sites. CO chemisorption measurements (Figure 5.1c) reveal a parallel decrease in apparent Ru dispersion with increasing drying temperature, from nearly $D \approx 60\%$ at low drying temperatures to ~30% at 120 °C. Although absolute dispersion values are affected by the formation of multi-carbonyl species and should not be interpreted as direct measures of particle size (see Chapter 1.2.3),[3–9] the relative trend indicates a loss of accessible low-coordination Ru sites upon dehydration and partial structural consolidation of the Ru oxy-hydroxide phase. The short activation step used prior to CO chemisorption (120 °C, 5 min) preserves the structural features established during overnight drying, enabling meaningful comparison across samples.

Overall, controlled dehydration enables the transformation of a fraction of the hydrated Ru oxy-hydroxide matrix into RuO_2-like domains, rendering the intrinsic two-step redox pathway experimentally resolvable. Consequently, as water is removed, reduction evolves from a single broad event associated with hydrated agglomerates to two kinetically resolved redox steps within the same domains, while the contribution of small, highly defective Ru oxy-hydroxide nanoparticles remains essentially unchanged.

The effect of drying temperature was also investigated for the carbon-supported catalysts RuCw(w) and RuCch(w), as shown in Figure 5.2. In both cases, increasing the drying temperature does not induce major qualitative changes in the H_2-TPR profiles (Figure 5.2a,c), which remain dominated by broad and poorly resolved reduction features. Only a gradual broadening of the reduction event toward higher temperatures is observed, indicating a progressive decrease in reducibility without a clear kinetic separation of redox steps. This behavior contrasts with that observed for RuAl(w) (Figure 5.1a) and reflects the distinct nature of the Ru oxy-hydroxide phase stabilized on active carbon supports. As discussed in Chapter 3, the oxidized Ru phase on carbon supports is characterized by a predominantly hydroxylated local oxygen environment and by the presence of peroxo-like species, indicating a highly hydrated and structurally disordered surface. In addition, activated carbons exhibit a complex porous network dominated by interconnected mesoporous domains and pore constrictions, which can efficiently retain water through capillary condensation.[10–13] As a result, even after drying, a significant fraction of the Ru oxy-hydroxide phase remains hydrated, preventing a clear kinetic separation of the intrinsic Ru(IV) → Ru(III) → Ru(0) redox steps and leading to largely overlapped reduction events in H_2-TPR. Importantly, water retention in these systems is not solely associated with the active carbon support. The Ru oxy-hydroxide phase itself is intrinsically hydrophilic,[14] owing to the high density of polar Ru–OH groups and non-stoichiometric oxygen species evidenced by O K-edge NEXAFS. These polar surface motifs can strongly bind and stabilize water molecules at the Ru interface, reinforcing the hydrated character of the Ru phase even when partial dehydration of the carbon support is achieved. Consequently, post-synthesis drying affects primarily the degree of hydration and the reduction kinetics of Ru oxy-hydroxide domains, rather than inducing major structural transformations.

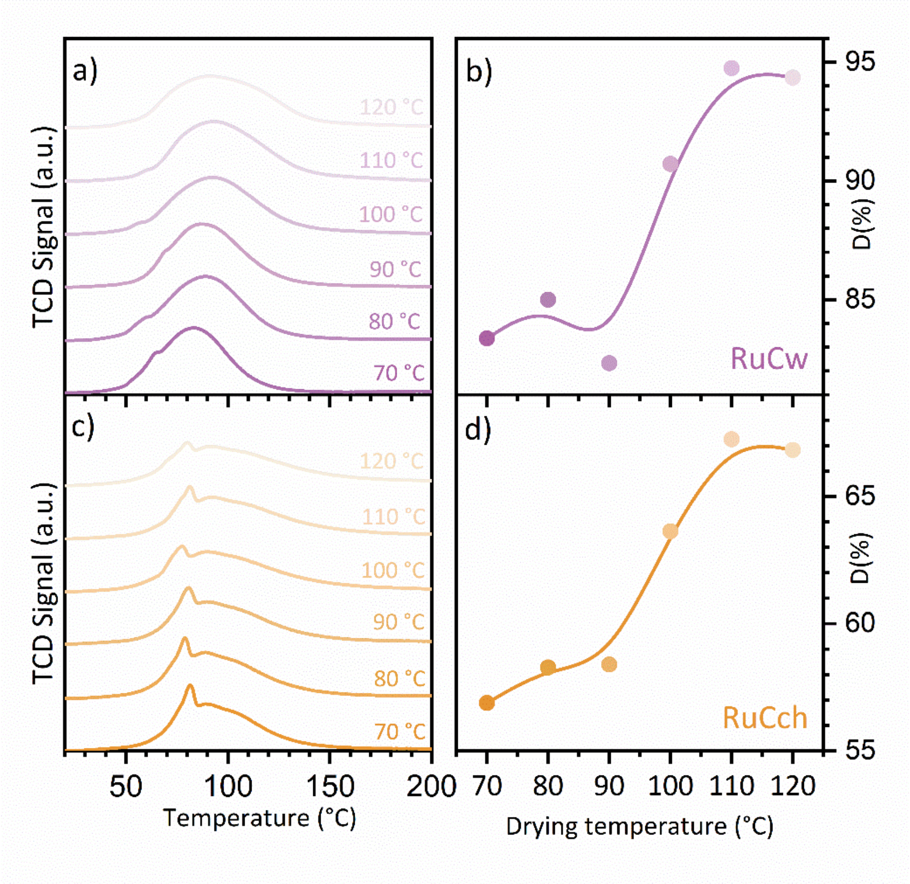

Figure 5.2 (a-c) H_2-TPR thermograms and (b-d) apparent Ru dispersion values obtained by pulsed CO chemisorption for RuCw(w) and RuCch(w) dried overnight at different temperatures in the 70-120 °C range, illustrating the effect of post-synthesis drying on reducibility and site accessibility. In panels (b) and (d), the lines connecting the data points are spline guides to the eye.

In contrast to the limited sensitivity of the TPR profiles to drying temperature, CO chemisorption reveals a pronounced increase in apparent Ru dispersion with increasing drying temperature for both RuCw(w) and RuCch(w) (Figure 5.2b,d). This trend, opposite to that observed for RuAl(w), cannot be ascribed to an actual increase in metal dispersion. Instead, it reflects changes in site accessibility associated with water removal from the porous carbon network and from the Ru oxy-hydroxide surface. At low drying temperatures, a fraction of Ru sites is effectively shielded from gas-phase probes by water retained within mesoporous domains and pore constrictions. Drying at temperatures above ~100 °C progressively removes this water, restoring access of CO to small and highly defective Ru sites and leading to an apparent increase in dispersion.

Notably, the increase in apparent dispersion is slightly more pronounced for RuCw(w) than for RuCch(w). This behavior is consistent with the higher density of oxygen-containing functional groups and the higher hydrophilicity of chemically activated carbons,[10–12] which enhance water uptake and retention within the porous network. Absolute dispersion values remain affected by the formation of multi-carbonyl species on Ru and should be interpreted with caution; nevertheless, the consistent trends observed for both carbon-supported catalysts robustly capture the dominant role of water in governing Ru site accessibility.

5.3 Catalysts stability in time: ageing monitored by H_2-TPR and CO chemisorption

The stability after drying procedure at 90°C of Ru catalysts prepared by deposition–precipitation was investigated by monitoring the evolution of reducibility and site accessibility of RuAl upon ageing under ambient conditions. Considering the results discussed in the previous paragraph, ageing can be regarded as a slow and uncontrolled dehydration process, which drives the Ru oxy-hydroxide phase along the same transformation pathway observed under controlled post-synthesis drying.

The reducibility and apparent dispersion of RuAl were monitored over a period of 32 weeks (Figure 5.3). With increasing ageing time, the H_2-TPR profiles progressively shifted towards higher temperatures by approximately 10 °C and became broader, indicating a gradual decrease in reducibility. In contrast, the total H_2 consumption remained essentially unchanged, ruling out the formation of more highly oxidized Ru species and indicating that the overall redox stoichiometry of the Ru phase is preserved. The apparent Ru dispersion decreases markedly upon ageing, from an initial value of $D \approx 33\%$ to approximately 20%, corresponding to a loss of about 40% of CO-accessible Ru sites. At this point it is worth noting that, after ageing the new batch synthesized, the dispersion measured is compatible with the value presented in Chapter 1, which was in fact measured weeks after synthesis.

This loss does not reflect the disappearance of Ru species, but rather a decrease in site accessibility associated with slow dehydration and structural consolidation of the Ru oxy-hydroxide phase. As discussed for controlled drying, ageing primarily affects hydrated $RuO_x(OH)_y$ agglomerates. The progressive water loss promotes partial structural reorganization of these agglomerates into more ordered RuO_2-like domains, consistent with the emergence of kinetically resolved redox steps and with the μ_1(O) signatures observed by NEXAFS.

Notably, the persistence of H_2 overconsumption upon ageing indicates that a significant fraction of non-stoichiometric oxygen species, such as peroxo-like Ru–O–O moieties, remains stabilized at the Ru surface even after prolonged storage. This observation is consistent with the intrinsically hydrophilic character of the Ru oxy-hydroxide phase, which contains a high density of polar Ru–OH and non-stoichiometric oxygen species capable of retaining water at the Ru interface.[14,15] Ageing therefore proceeds as a gradual, rather than abrupt, dehydration process.

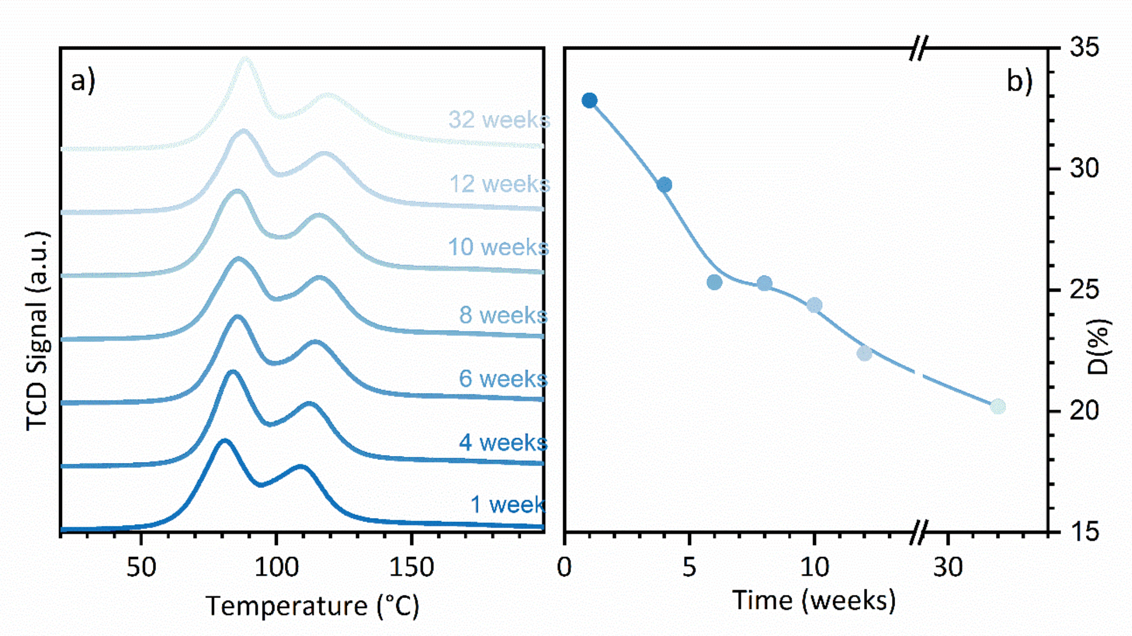

Figure 5.3 (a) Evolution of the H_2-TPR thermograms of RuAl as a function of time after synthesis, illustrating ageing-induced changes in reducibility. (b) Corresponding evolution of the apparent Ru dispersion values obtained by CO chemisorption, highlighting the progressive loss of CO-accessible Ru sites upon ageing under ambient conditions. In panel (b) the line connecting the data points is a spline guide to the eye.

Ageing effects were also evaluated for RuCw and RuCch after 40 weeks of storage (Figure A11). In agreement with the behavior observed under controlled drying, the reducibility of RuCw remains largely unchanged upon ageing, with only minor sharpening of the H_2-TPR profile, indicating a slight increase in the homogeneity of the Ru phase. In contrast, the H_2-TPR profile of RuCch shifts toward higher temperatures and becomes broader with ageing, resembling the trend observed for RuAl, albeit to a lesser extent. These differences can be rationalized by considering both the chemical affinity for water and the porous architecture of carbon supports. Chemically activated carbons such as Cch exhibit a higher density of oxygen-containing functional groups,[10–12] which increases the intrinsic hydrophilicity of both the support and the associated Ru oxy-hydroxide phase, leading to higher initial water uptake. At the same time, Cch contains a larger fraction of interconnected mesoporous domains,[10–13] which facilitate water transport and desorption during drying and storage. As a result, although more water is initially retained, gradual dehydration proceeds more rapidly, giving rise to a more pronounced ageing-induced evolution of reducibility and site accessibility. In contrast, physically activated carbons such as Cw contain fewer oxygen-containing functional groups and are less hydrophilic, but feature a higher fraction of narrow pores and pore constrictions.[10–13] These geometrical constraints can hinder water desorption and promote kinetic trapping of residual water within the pore network and at the Ru interface, resulting in a more persistent hydration of the Ru oxy-hydroxide phase and a slower ageing process.

Consistent with this interpretation, ageing leads to a decrease in apparent Ru dispersion for both carbon-supported catalysts, from $D \approx 84\%$ to 70% for RuCw and from $D \approx 66\%$ to 48% for RuCch. The larger loss observed for RuCch reflects its higher hydrophilicity and faster dehydration-driven structural consolidation, whereas the more modest change for RuCw indicates greater resistance to dehydration-induced ageing.

Notably, ageing effects are mitigated, but not fully suppressed, when catalysts are stored in the wet state and dried only immediately prior to characterization. This observation confirms that the Ru oxy-hydroxide phase obtained by deposition–precipitation is intrinsically metastable with respect to hydration and undergoes slow but measurable evolution over time, regardless of support nature and storage protocol.

Overall, ageing mirrors the effects of post-synthesis dehydration and highlights that the properties of DP-derived Ru catalysts are not static but evolve continuously as a function of water content. Changes in reducibility and accessible Ru sites arise from gradual dehydration and kinetic reorganization of hydrated Ru oxy-hydroxide domains, with partial RuO_2-like ordering occurring only on alumina-supported systems. These results emphasize that drying and storage history must be regarded as integral parameters of catalyst preparation and handling, particularly for liquid-phase hydrogenation applications where highly dispersed and partially hydrated Ru phases are often desirable.

5.4 Conclusions

In this paragraph, a lab scale systematic approach has been employed to elucidate how support chemistry and hydration jointly govern the structure, reducibility and stability of Ru catalysts prepared by deposition–precipitation (DP). By combining H_2-TPR and CO chemisorption, two techniques routinely employed in industrial catalyst development it was demonstrated that the $RuO_x(OH)_y$ phase formed by deposition-precipitation is intrinsically heterogeneous and metastable with respect to hydration, and that its evolution cannot be rationalized without explicitly considering the role of water.

Controlled post-synthesis drying and ageing of the $RuO_x(OH)_y$ phase are driven along the same transformation pathway, namely gradual dehydration and kinetic reorganization of Ru oxy-hydroxide domains. On alumina, drying temperatures below 90 °C preserves a predominantly hydrated Ru oxy-hydroxide phase, and the reduction proceeds through a single broad event. Only upon drying at temperatures $\geq$ 90 °C does partial dehydration promote the transformation of a fraction of hydrated agglomerates into RuO_2-like domains, at the expense of the amorphous oxy-hydroxide phase. This structural reorganization renders the intrinsic two-step redox pathway kinetically resolvable and is accompanied by a decrease in reducibility and CO-accessible low-coordination Ru sites. For carbon-supported catalysts, drying and ageing primarily affect site accessibility rather than intrinsic reduction kinetics, as high dispersion and a predominantly hydroxylated Ru environment suppress aggregation and prevent the formation of RuO_2-like domains.

Overall, our results demonstrate that in DP-derived Ru catalysts water is not merely residual moisture, but a transient structural component that controls both the nature of the oxidized Ru phase and its reduction kinetics. For liquid-phase hydrogenation applications, preserving a partially hydrated, highly dispersed Ru oxy-hydroxide phase is advantageous to maximize the density of low-coordination Ru sites, but only when aggregation into RuO_2-like domains is suppressed. Consequently, drying temperature, storage conditions and activation protocols must be treated as integral parameters of catalyst synthesis and handling to ensure reproducible performance. More broadly, this study highlights that the key trade-off of deposition–precipitation: while the method enables exceptionally high dispersion and defect-rich Ru phases, the intrinsic tendency of the Ru oxy-hydroxide phase to condense into RuO_2-like domains upon dehydration must be controlled. Activated carbon supports effectively suppress this condensation, whereas alumina and unsupported systems allow it. Managing this sensitivity is essential to fully exploit DP-derived Ru catalysts in industrially relevant liquid-phase processes.

References

(1) Deka, N.; Jones, T. E.; Falling, L. J.; Sandoval-Diaz, L.-E.; Lunkenbein, T.; Velasco-Velez, J.-J.; Chan, T.-S.; Chuang, C.-H.; Knop-Gericke, A.; Mom, R. V. On the Operando Structure of Ruthenium Oxides during the Oxygen Evolution Reaction in Acidic Media. *ACS Catal.* **2023**, *13* (11), 7488–7498. https://doi.org/10.1021/acscatal.3c01607.

(2) Occhialini, C. A.; Bisogni, V.; You, H.; Barbour, A.; Jarrige, I.; Mitchell, J. F.; Comin, R.; Pelliciari, J. Local Electronic Structure of Rutile RuO2. *Phys. Rev. Res.* **2021**, *3* (3), 33214. https://doi.org/10.1103/PhysRevResearch.3.033214.

(3) Hadjiivanov, K.; Lavalley, J.-C.; Lamotte, J.; Maugé, F.; Saint-Just, J.; Che, M. FTIR Study of CO Interaction with Ru/TiO2Catalysts. *J. Catal.* **1998**, *176* (2), 415–425. https://doi.org/https://doi.org/10.1006/jcat.1998.2038.

(4) Tolek, W.; Nanthasanti, N.; Pongthawornsakun, B.; Praserthdam, P.; Panpranot, J. Effects of TiO2 Structure and Co Addition as a Second Metal on Ru-Based Catalysts Supported on TiO2 for Selective Hydrogenation of Furfural to FA. *Sci. Rep.* **2021**, *11* (1), 9786. https://doi.org/10.1038/s41598-021-89082-x.

(5) Betancourt, P.; Rives, A.; Hubaut, R.; Scott, C.; Goldwasser, J. A Study of the Ruthenium–Alumina System. *Applied Catalysis A-general - APPL CATAL A-GEN* **1998**, *170*, 307–314. https://doi.org/10.1016/S0926-860X(98)00061-1.

(6) Guglielminotti, E.; Boccuzzi, F.; Manzoli, M.; Pinna, F.; Scarpa, M. Ru/ZrO2 Catalysts: I. O2, CO, and NO Adsorption and Reactivity. *J. Catal.* **2000**, *192* (1), 149–157. https://doi.org/10.1006/JCAT.2000.2835.

(7) Masthan, S. K.; Chary, K. V. R.; Rao, P. K. Measurement of Surface Dispersion of Ruthenium on γ-Al2O3 Support by Low-Temperature Oxygen Chemisorption (LTOC) Technique. *J. Catal.* **1990**, *124* (1), 289–292. https://doi.org/10.1016/0021-9517(90)90125-4.

(8) Kantcheva, M.; Sayan, S. On the Mechanism of CO Adsorption on a Silica-supported Ruthenium Catalyst. *Catal. Letters* **1999**, *60* (1), 27–38. https://doi.org/10.1023/A:1019082218590.

(9) Truszkiewicz, E.; Zegadło, K.; Wojda, D.; Mierzwa, B.; Kępiński, L. The Effect of the Ruthenium Crystallite Size on the Activity of Ru/Carbon Systems in CO Methanation. *Top. Catal.* **2017**, *60* (17), 1299–1305. https://doi.org/10.1007/s11244-017-0815-z.

(10) Vottero, E.; Carosso, M.; Pellegrini, R.; Piovano, A.; Groppo, E. Assessing the Functional Groups in Activated Carbons through a Multi-Technique Approach. *Catal. Sci. Technol.* **2022**, *12* (4), 1271–1288. https://doi.org/10.1039/D1CY01751A.

(11) Piovano, A.; Lazzarini, A.; Pellegrini, R.; Leofanti, G.; Agostini, G.; Rudić, S.; Bugaev, A. L.; Lamberti, C.; Groppo, E. Progress in the Characterization of the Surface Species in Activated Carbons by Means of INS Spectroscopy Coupled with Detailed DFT Calculations. *Advances in Condensed Matter Physics* **2015**, *2015* (1), 803267. https://doi.org/https://doi.org/10.1155/2015/803267.

(12) Lazzarini, A.; Piovano, A.; Pellegrini, R.; Leofanti, G.; Agostini, G.; Rudić, S.; Chierotti, M. R.; Gobetto, R.; Battiato, A.; Spoto, G.; Zecchina, A.; Lamberti, C.; Groppo, E. A Comprehensive Approach to Investigate the Structural and Surface Properties of Activated Carbons and Related Pd-Based Catalysts. *Catal. Sci. Technol.* **2016**, *6* (13), 4910–4922. https://doi.org/10.1039/C6CY00159A.

(13) Pellegrini, R.; Leofanti, G.; Agostini, G.; Groppo, E.; Lamberti, C. Investigation of Carbon and Alumina Supported Pd Catalysts during Catalyst Preparation. *Stud. Surf. Sci. Catal.* **2010**, *175*, 437–440. https://doi.org/10.1016/S0167-2991(10)75079-5.

(14) Di Liberto, G.; Pacchioni, G.; Shao-Horn, Y.; Giordano, L. Role of Water Solvation on the Key Intermediates Catalyzing Oxygen Evolution on RuO2. *The Journal of Physical Chemistry C* **2023**, *127* (21), 10127–10133. https://doi.org/10.1021/acs.jpcc.3c02733.

(15) McKeown, D. A.; Hagans, P. L.; Carette, L. P. L.; Russell, A. E.; Swider, K. E.; Rolison, D. R. Structure of Hydrous Ruthenium Oxides: Implications for Charge Storage. *J. Phys. Chem. B* **1999**, *103* (23), 4825–4832. https://doi.org/10.1021/jp990096n.

Chapter 6

6 General conclusions and perspectives

6.1 Context, scope and motivation

This thesis work results from a long-lasting collaboration between the Department of Chemistry at the University of Torino and Chimet S.p.A., which has contributed to the advancement of precious metals-based heterogeneous catalysts over the past decades. Recently, this collaboration was further strengthened and contextualized within the framework of the European Next Generation EU program, marking the first PhD project jointly funded by European resources and Chimet S.p.A. The project also represented the first occasion in which a PhD candidate was hosted for a six-month internship within the company, enabling first-hand exposure to industrial catalyst production, scale-up constraints and development strategies. This industrial experience was complemented by a six-month research period at the Institute Laue Langevin in Grenoble, where most of the data analysis presented in this thesis was carried out. The combination of academic research, industrial immersion and access to large-scale facilities profoundly shaped both the scientific direction and the practical relevance of this work.

While the collaboration had previously focused on Pd- and Pt-based catalysts prepared by deposition-precipitation, the growing interest in Ru-based systems motivated the extension of this approach to ruthenium. Because Ru catalysts rarely behave as simple analogues of Pd- and Pt-based systems, this transition required the development of new experimental strategies and interpretative tools, often relying on a more exploratory and open-minded approach.

In this context, it became evident that many of the assumptions commonly applied to noble-metal catalysts could not be transferred directly to Ru-based systems, particularly with respect to the nature of the oxidized precursor and its activation under hydrogen. This realization provided the scientific motivation for the present thesis, which was designed to address fundamental questions on the structure, evolution and functional role of the Ru phase obtained by deposition–precipitation.

6.2 Nature of the oxidized Ru phase obtained by deposition–precipitation

At the core of these questions lies the oxidized Ru phase formed during synthesis, which represents the true starting point of catalyst activation and ultimately determines reducibility, dispersion and catalytic behavior. The primary objective of this thesis was to clarify the nature of the hydrated oxidized Ru phase obtained by deposition-precipitation under industrially relevant conditions, and to elucidate how this phase evolved during activation and reduction. To this end, a broad multi-technique approach was employed, combining laboratory-scale methods routinely used in industry with advanced synchrotron- and neutron-based techniques.

Electron microscopy revealed that, irrespective of the synthesis route, Ru displays a strong tendency to form highly dispersed oxy-hydroxide phases, even in the absence of a support. Very small nanoparticles systematically coexist alongside larger hydrated agglomerates, whose abundance and morphology strongly depend on the surface chemistry of the support. Structural characterization by X-ray total scattering and X-ray absorption spectroscopy on selected reference systems (unsupported Ru-oxide and Ru/Al_2O_3), together with H_2-TPR analysis, confirmed an average Ru(IV) stoichiometry and a rutile-like local coordination. However, the oxidized Ru phase cannot be described as a single, well-defined RuO_2 compound. Instead, it spans a family of highly disordered RuO_2-like motifs to more crystalline domains, often coexisting within the same catalyst depending on support-related chemistry and hydration state.

Surface-sensitive O K-edge NEXAFS provided clear evidence that support chemistry plays a decisive role in stabilizing different oxygen environments. Activated carbons favor highly defective and strongly hydrated Ru oxy-hydroxide nanoparticles, whereas alumina allows partial structural ordering. Across all systems, peroxo-like Ru-O-O species were identified at the surface of the oxidized phase, and their abundance was found to correlate with the systematic overconsumption of hydrogen observed during H_2-TPR. This establishes a direct link between surface oxygen chemistry and macroscopic reducibility fingerprints.

6.3 Bulk reduction pathway and surface activation mechanisms

The complex, multi-feature H_2-TPR thermograms characteristic of DP-derived Ru catalysts clearly indicated that reduction does not follow a simple or direct pathway. By coupling H_2-

TPR with *in situ* Ru K-edge XAS, high-energy total scattering/PDF and XRD, and by applying multivariate statistical analysis, this thesis demonstrates unambiguously that reduction proceeds through a transient Ru(III)-intermediate. Structural fingerprints extracted from EXAFS and PDF, including a characteristic short Ru–Ru distance (~2.6 Å) and lattice expansion effects associated with oxygen-vacancy formation, support the assignment of a corundum-like Ru_2O_3 intermediate phase. The existence of this intermediate explains the origin of multiple reduction events in TPR thermograms and resolves a long-standing ambiguity in the interpretation of Ru reducibility.

Surface-sensitive *in situ* IR spectroscopy, O K-edge NEXAFS and INS revealed that bulk reduction is accompanied by a sequence of tightly coupled surface processes. Thermal dehydration was shown to be an active restructuring step rather than a passive removal of water, inducing hydroxyl condensation, rearrangement of peroxo species and partial surface reduction to a defective RuO_{2-x} phase. Upon exposure to hydrogen, oxygenated surface species are rapidly and completely consumed through water formation, while hydrides are transiently stabilized on Ru surfaces. IR spectroscopy selectively detected terminal Ru–H species, while INS provided direct evidence of the formation of multi-coordinated and subsurface hydrides that are largely invisible to IR probes. Crucially, INS delivered direct spectroscopic evidence of hydrogen spillover at the Ru-Al_2O3 interface, capturing a phenomenon that is often invoked but rarely observed experimentally and highlighting its relevance for hydrogen activation and transfer.

6.4 Catalytic implications and validation of the mechanistic framework

Catalytic tests in the selective hydrogenation of benzaldehyde served as a validation of the reduction mechanisms developed during characterization. Marked differences between unsupported Ru and alumina-supported Ru demonstrate that catalytic activity cannot be interpreted solely in terms of the presence of metallic Ru. The amorphous and partially hydrated $RuO_x(OH)_y$ phase characteristic of unsupported Ru exhibited significant activity under mild conditions, indicating that oxidic and partially reduced Ru states can directly participate in hydrogen activation and transfer. In contrast, Ru/Al_2O_3 required higher temperatures to achieve substantial activity, consistent with the progressive formation of metallic Ru stabilized by the support. These results challenge the widespread empirical paradigm that fully reduced Ru is the exclusive active phase in Ru-based hydrogenation catalysis and highlight the functional relevance of precursor structure, hydration and disorder in DP-derived systems. More broadly, they demonstrate the importance of linking complementary multi-technique characterization directly to catalytic performance to extract meaningful mechanistic insight from H_2-TPR thermograms.

6.5 Water as a structural variable: drying, ageing and methodological relevance

A central and unifying outcome of this thesis is the recognition of water as an active structural component of Ru catalysts prepared by deposition–precipitation. Rationalizing its role required a dedicated and time-consuming experimental strategy inherently incompatible with large-scale facilities. This constraint motivated the development of a simple, yet robust and transferable methodology based on H_2-TPR and CO chemisorption, two techniques widely employed both in academic research and industrial catalyst development.

Systematic investigations of controlled post-synthesis drying and ageing demonstrated that the observed transformations can be attributed to the same structural reorganization driven by gradual dehydration. Water regulates local coordination, reducibility, dispersion and Ru site accessibility, thereby controlling both catalyst stability and performance. These results highlight a fundamental trade-off intrinsic to deposition–precipitation synthesis: while the method enables exceptionally high dispersion at high metal loadings, it also promotes the formation of highly hydrated oxidized Ru aggregates. Controlling water content is therefore essential to prevent uncontrolled condensation into RuO_2-like domains during drying and ageing. In this context, the drying step should be regarded as a deliberate thermal treatment aimed at achieving the optimal hydration state, rather than as a simple solvent-removal operation, especially for industrially relevant liquid-phase processes.

6.6 Perspectives

The results presented in this thesis open several perspectives for future research, both in terms of fundamental characterization and methodological development, as well as in relation to industrially relevant catalytic processes.

A first and particularly promising direction concerns the direct investigation of hydrogen-derived species under reaction conditions. This work demonstrated that hydrides on Ru nanoparticles can be detected spectroscopically and that hydrogen spillover at the Ru–Al_2O_3 interface can be directly observed by inelastic neutron scattering. These findings provide a solid experimental basis to move beyond activation studies and to probe the nature, coordination and dynamics of Ru–H species during hydrogenation reactions. The experimental strategies and spectroscopic set-ups developed in this thesis could therefore be exploited to discriminate between different types of hydrides (terminal, multi-coordinated or subsurface) and to clarify their specific role in hydrogen activation and transfer under *operando* conditions.

An especially challenging but highly impactful extension would be the application of these approaches to reactions involving more demanding conditions, such as ammonia synthesis. In this case, the relevance of hydrogen spillover and surface hydride species is well recognized, yet it remains poorly characterized due to the intrinsic experimental complexity. The high pressures required for ammonia synthesis would necessitate substantial modifications of the current experimental apparatus, particularly for *operando* spectroscopic measurements. Nevertheless, the insights gained in this thesis provide a clear conceptual and methodological framework to guide such developments and to identify the most critical parameters to be addressed.

A second important perspective concerns the use of probe molecules to quantify dispersion and site accessibility, with particular reference to CO. In this thesis, CO was employed as a probe for pulsed chemisorption measurements primarily for practical and industrial reasons, as CO chemisorption is routinely used at Chimet S.p.A. to assess dispersion in Pd-based catalysts. While this choice ensured direct comparability with industrial practice, the present results also highlight the limitations of CO as a universal probe for Ru-based systems, especially in the presence of small, defective or partially oxidized nanoparticles. The literature suggests that CO adsorption on Ru can involve multiple binding geometries and stoichiometries, which may lead to a wrong estimation of dispersion. Future work should therefore aim at a more systematic evaluation of probe molecules, combining static and dynamic adsorption experiments and directly comparing CO- and H_2-based measurements. Such a comparative approach would help disentangle purely geometric effects from electronic and chemical contributions and would provide a more reliable assessment of accessible Ru sites across different oxidation and hydration states.

More broadly, the methodologies developed in this thesis, based on the integration of lab-scale techniques with advanced spectroscopies and on careful control of post-synthesis treatments, can be readily transferred to other catalyst systems prepared by deposition–precipitation. Extending these approaches to Ru catalysts supported on activated carbons, as well as to unsupported Ru oxy-hydroxide systems, would be particularly valuable. The latter, initially introduced as reference materials, exhibited unexpected structural and catalytic properties that deserve further investigation in terms of reproducibility, long-term stability and sensitivity to controlled drying and ageing.

In conclusion, this thesis not only provides mechanistic insight into Ru-based catalysts prepared by deposition–precipitation, but it also establishes a versatile experimental and conceptual toolbox. This toolbox can be exploited to tackle open questions on hydrogen activation, metal–support interactions and catalyst stability in a wide range of hydrogenation and hydrogen-involving reactions, bridging fundamental research and industrial catalyst development.

Appendix

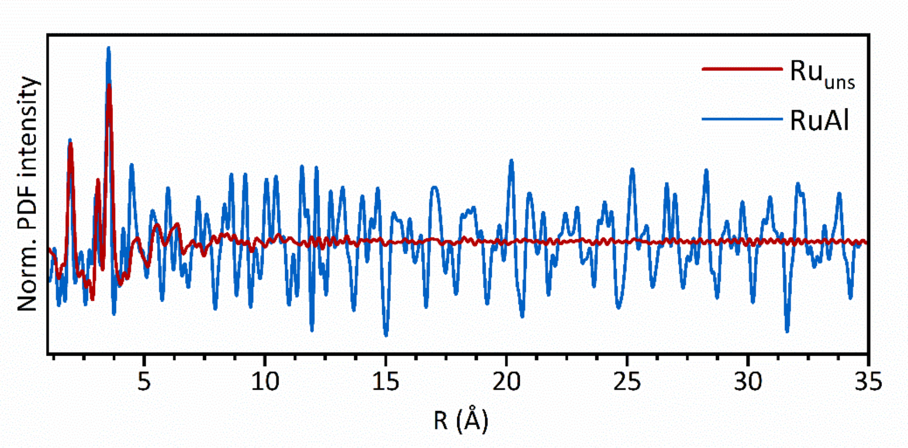

Figure A1 Normalized pair distribution functions of Ru$_{uns}$ and RuAl after subtraction of the cell contribution. For RuAl, the pattern of alumina collected in the same experimental conditions, up to R=35 Å, was subtracted.

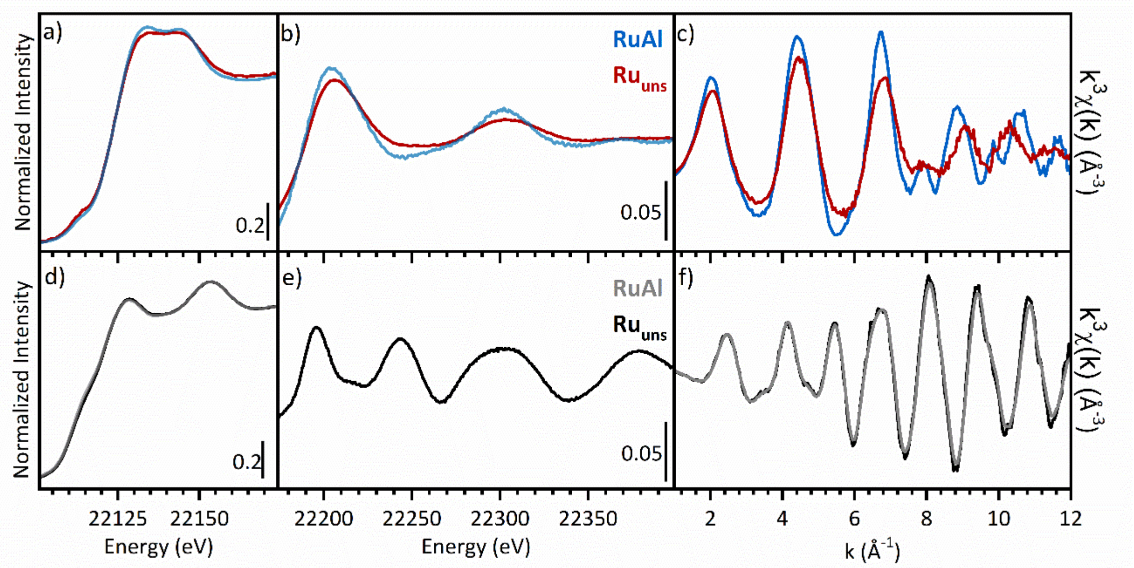

Figure A2 Normalized Ru K-edge XAS spectra of pristine Ru$_{uns}$ and RuAl in the XANES (a) and EXAFS (b) regions, and k^3-weighted χ(k) functions (c). Same for RuAl and Ru$_{uns}$ at 200°C in H_2 (d,e and f).

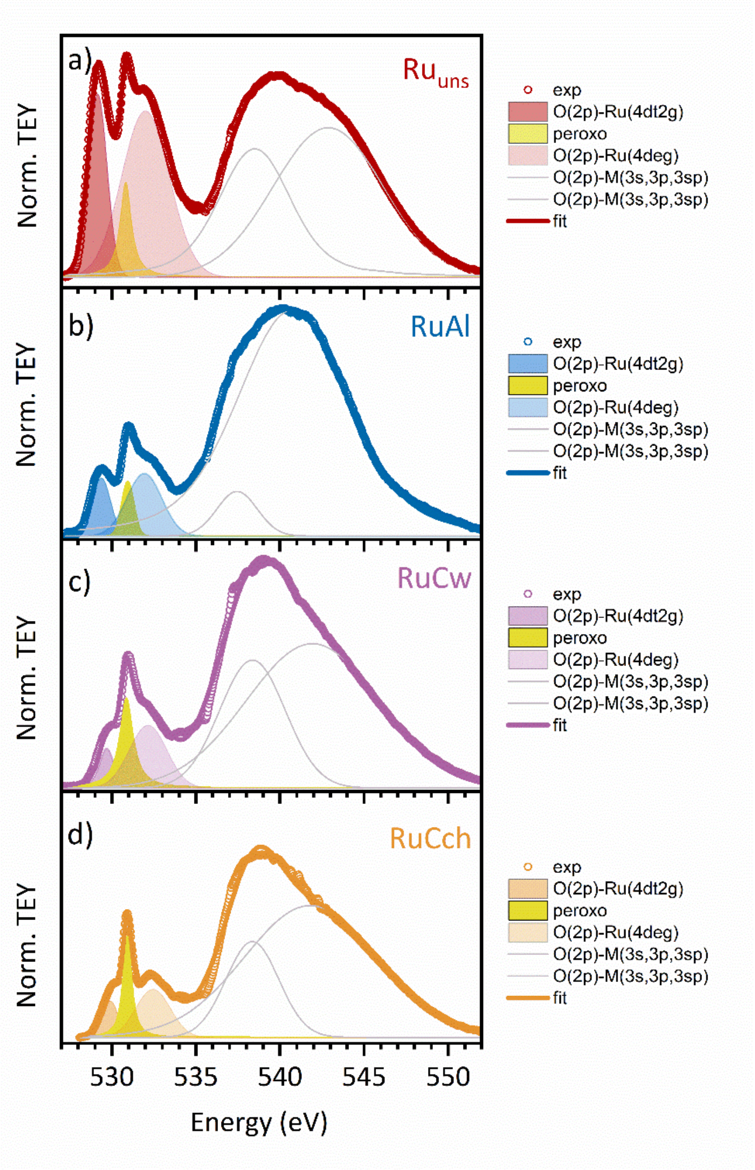

Figure A3 Normalized O K-edge NEXAFS spectra of (a) Ru_{uns}, (b) RuAl, (c) RuCw and (d) RuCCh in the pre-edge region, together with best-fit components, highlighting support-dependent differences in the local oxygen coordination of the Ru phase.

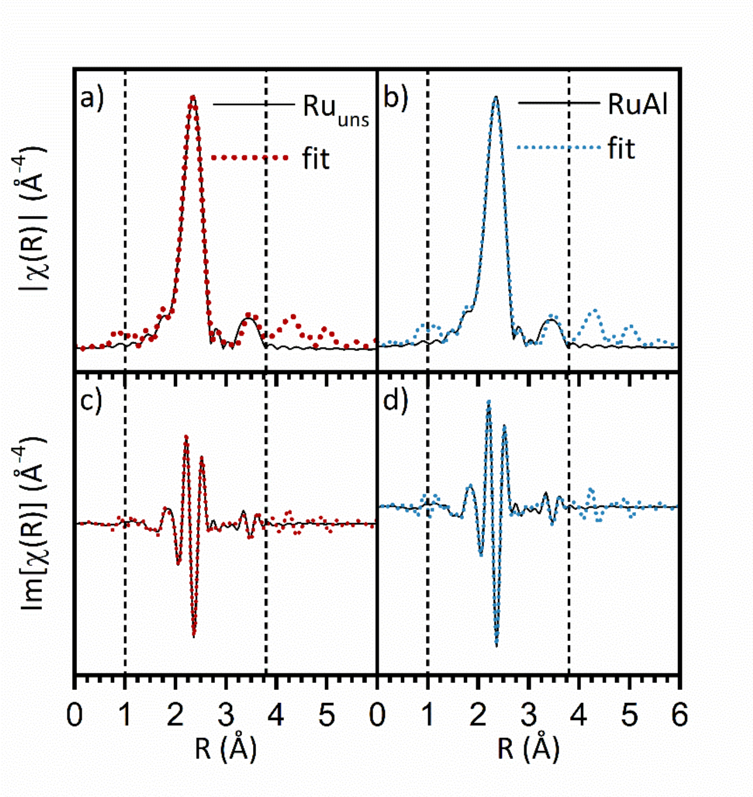

Figure A4 |FT| (a and b) and Im(FT) (c and d) of the k^3-weighted EXAFS functions for Ru_{uns} and RuAl in H_2 at 200°C and their fit. The dotted vertical lines indicate the windows considered for the fitting procedure.

Table A1 Results of the EXAFS data analysis for Ru_{uns} and RuAl in H_2 at 200°C.

	Scattering	**N_C (atoms)**	**R (Å)**	**σ^2 (Å^{-2})**	**X^2_v**	**R factor**
Ru_{uns}	Ru_1	3.8 ± 0.2	2.625 ± 0.004	0.004 ± 0.0003	3.8	0.9
	Ru_2	3.8 ± 0.2	2.717 ± 0.006	0.004 ± 0.0003		
	Ru_3	1.5 ± 0.3	3.777 ± 0.009	0.004 ± 0.0003		
RuAl	Ru_1	4.0 ± 0.4	2.622 ± 0.007	0.0045 ± 0.0014	99	1
	Ru_2	4.0 ± 0.4	2.710 ± 0.009	0.0045 ± 0.0014		
	Ru_3	1.3 ± 0.5	3.769 ± 0.012	0.0045 ± 0.0014		

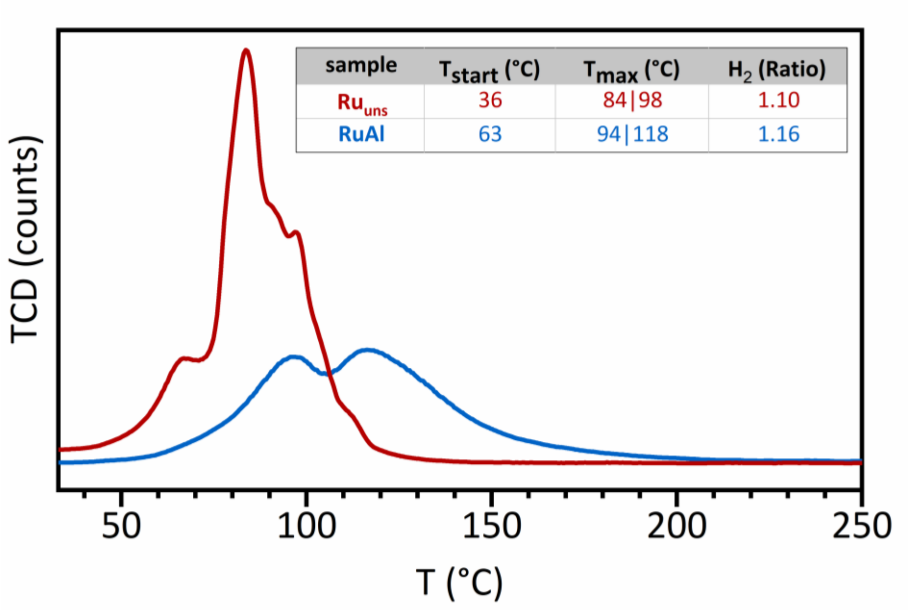

Figure A5 H_2-TPR collected from 25°C.

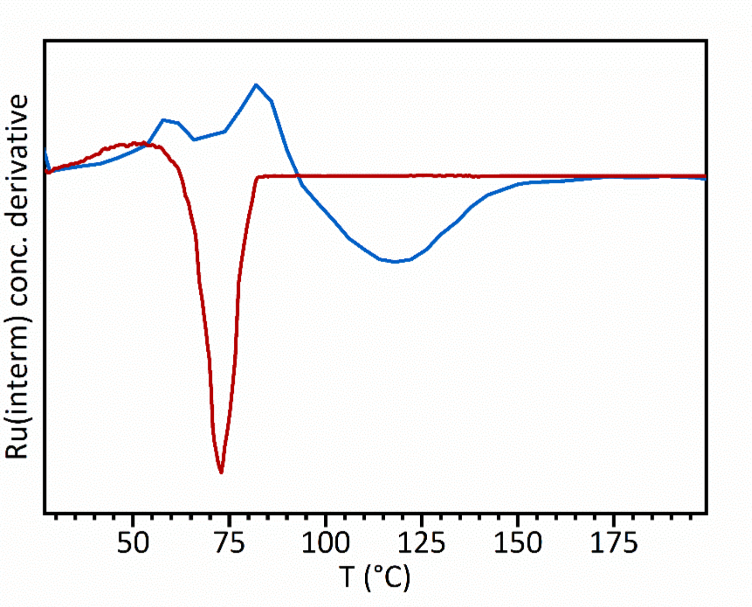

Figure A6 First derivatives of concentration profile of intermediate components obtained with MCR-ALS approach for Ru_{uns} (red) and RuAl (blue).

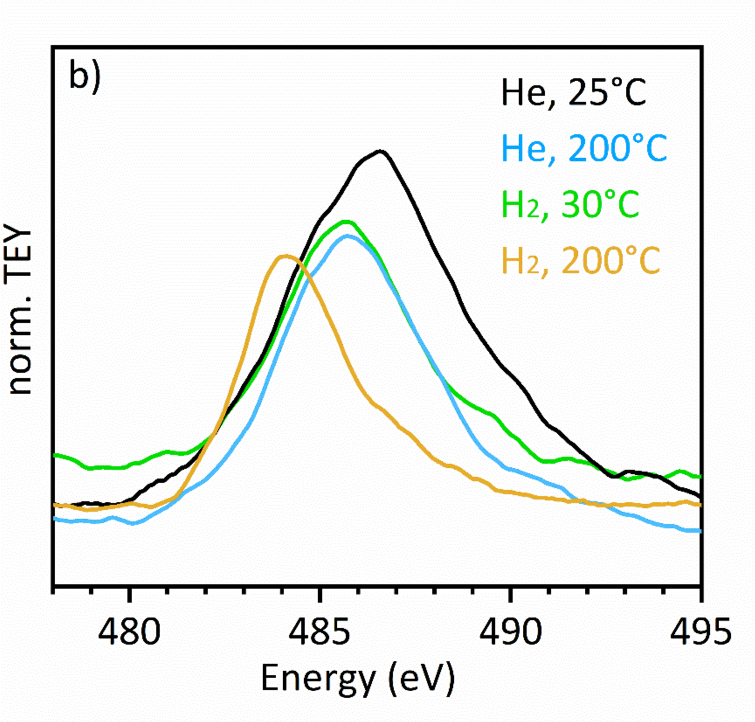

Figure A7 Normalized Ru M_2-edge spectra collected in different atmospheric and temperature conditions.

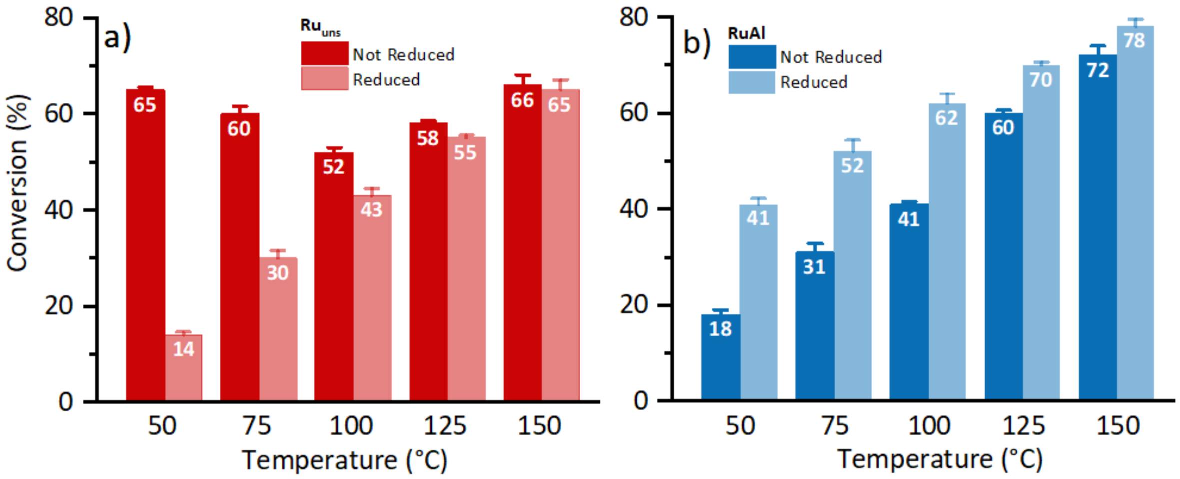

Figure A8 Hydrogenation of benzaldehyde in the temperature range 50-150°C over a) Ru_{uns} and b) RuAl catalysts in their pristine and pre-reduced forms

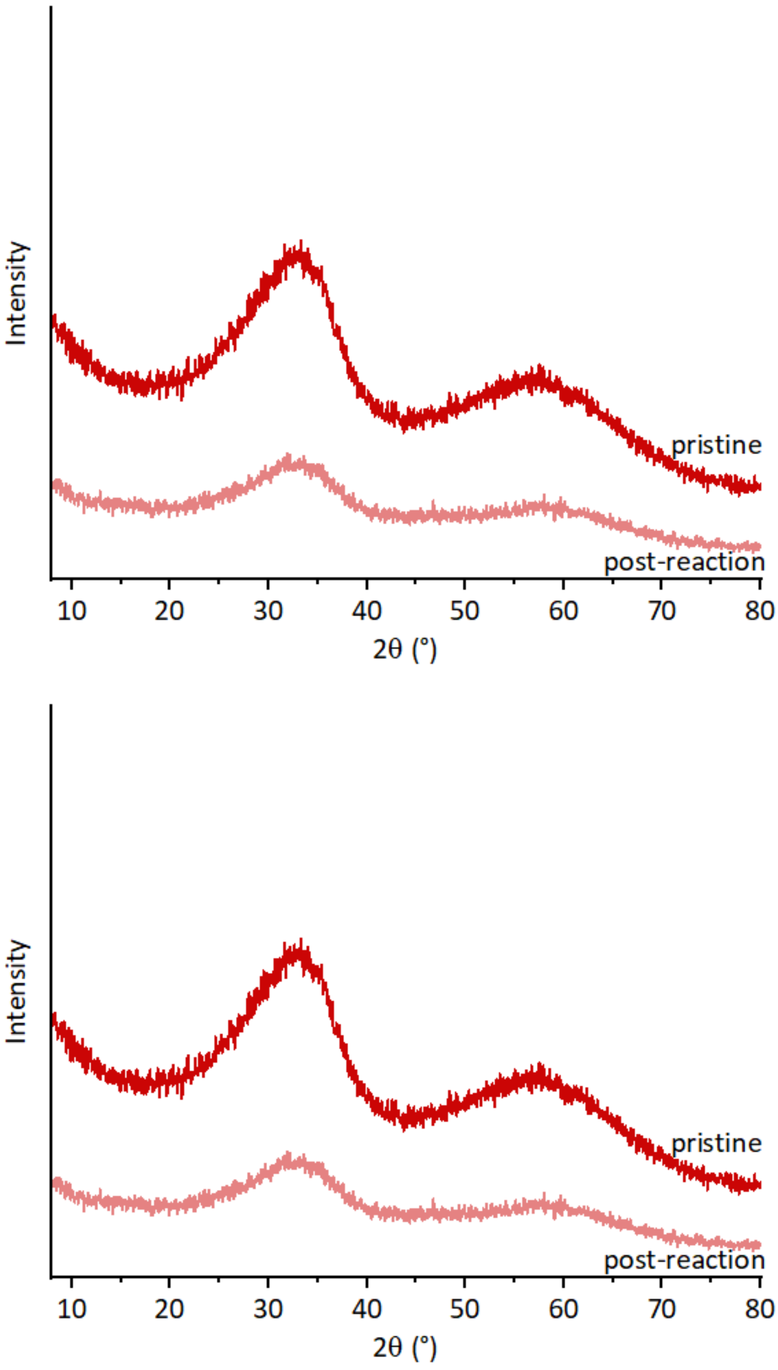

Figure A 9 XRD patterns of Ru$_{uns}$ before (pristine) and after (post reaction) its use in the hydrogenation of benzaldehyde at 50°C

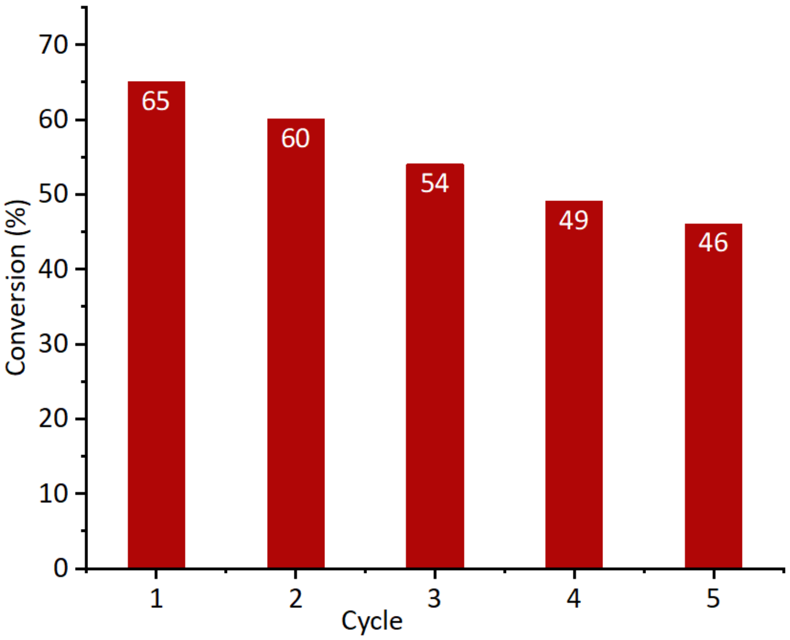

Figure A 10 Catalyst stability over five consecutive reaction cycles. Benzaldehyde hydrogenation at 50°C was performed using Ru_{uns} under identical conditions for each cycle.

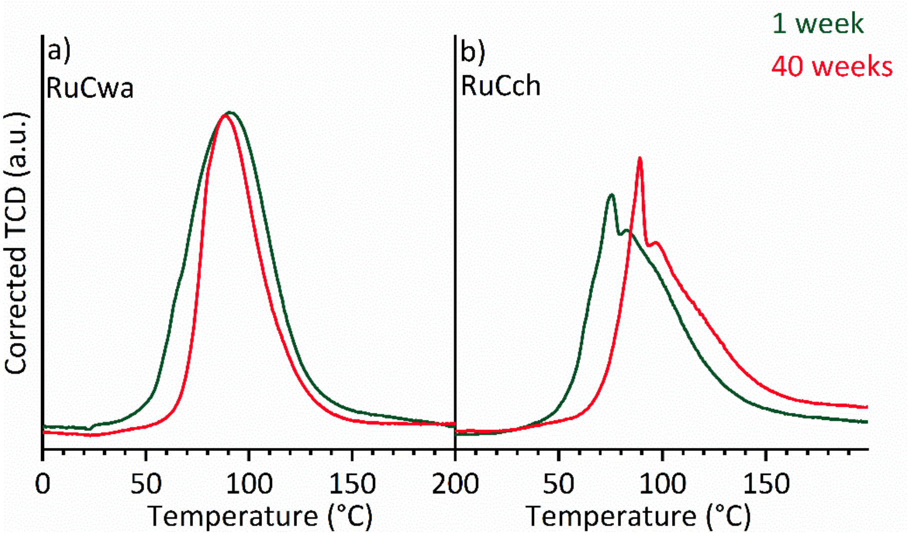

Figure A11 Evolution of H_2-TPR thermograms for (a) RuCw and (b) RuCch during 40 weeks of ageing after being dried at 90 °C.